IMAGING AND MONITORING SUBSURFACE STRUCTURE BY USING CROSS-CORRELATION OF SEISMIC AMBIENT NOISE

二宮, 啓

IMAGING AND MONITORING SUBSURFACE STRUCTURE BY USING CROSS-CORRELATION OF SEISMIC AMBIENT NOISE

HIRO NIMIYA

2022

IMAGING AND MONITORING SUBSURFACE STRUCTURE BY USING CROSS-CORRELATION OF SEISMIC AMBIENT NOISE

by

HIRO NIMIYA

A dissertation submitted in partial fulfillment of requirements

for the degree of

Doctoral Engineering

Examination Committee:

Prof. Akira Imai (Chairman)

Prof. Takeshi Tsuji

Assoc. Prof. Jun Nishijima

Assoc. Prof. Hideki Mizunaga

Department of Earth Resources Engineering

Graduate School of Engineering

Kyushu University

Japan

May 2022

Abstract

Constructing an accurate underground structure model and monitoring the underground state is essential to realize a society prepared for natural disasters and enables sustainable development. In this study, I have conducted several studies about both imaging and monitoring subsurface structures using ambient seismic noise generated from atmospheric, oceanic, and other turbulent flows and social activities of people. The approach using seismic ambient noise is highly versatile due to the simple procedure of this method, the constant presence of the ambient seismic noise, and the development permanent high-quality seismic network in Japan. Improving this versatile approach is important to develop a practical system of imaging and monitoring subsurface structure. Developing a practical system accelerates the realization of a resilient and sustainable society. The details of the background, motivation, and purpose of this study are described in Chapter 1.

In Chapters 2 and 3, I studied imaging underground structures by using surface waves extracted from ambient seismic noise to improve the accuracy and resolution of estimated subsurface structures. In Chapter 2, I focused on improving the horizontal resolutions and visualized central Japan's subsurface S-wave velocity structure. The horizontal resolution was improved by combining the tomographic approach and higher frequency Rayleigh wave which is sensitive to smaller structures. I developed an application to automatically estimate the dispersion curve of the Rayleigh wave since the tomographic approach requires a mass of dispersion data. The estimated high-resolution three-dimensional S-wave velocity structure was used to interpret the complex geological structure of central Japan.

In Chapter 3, I focused on improving the vertical resolutions using higher modes of surface waves. Here I estimated the subsurface structure of the Kanto Basin, where thick sedimentary layers exist. Thick sediments and strong velocity contrast between sediments and basement rock induce higher modes of the surface wave. I estimated multimodal surface-wave dispersion curves by applying a method that can separate the phase velocities of fundamental and higher modes. The vertical resolution was improved by using higher modes of surface waves. The accuracy and precision of the estimated S-wave velocity model were significantly improved by at least 50% by using higher modes. Since each mode of surface waves has a different sensitivity to the S-wave velocity and thickness, including higher modes resulted in constraining the solutions such that they could be well estimated. The estimated S-wave velocity model using higher modes better explains the complex characteristics of seismic wave propagation, which cause significant damage when a large earthquake occurs.

Next, I used ambient seismic noise to monitor the subsurface structures, taking advantage of the constant presence of the ambient seismic noise. The time-series of surface waves as a signal were extracted by calculating cross-correlations of ambient seismic noise

each day. The state of the subsurface structure can be reflected through the seismic velocity of the surface wave, which propagates between two seismic stations. Since the seismic velocity change is too small to estimate from the direct part of the surface wave, I used scattered waves which follow the direct surface wave. Chapter 4 revealed the change in the subsurface structure during the 2016 Kumamoto earthquake from the seismic velocity change. The velocity changes before and after the Kumamoto earthquake were estimated in many pairs of seismic stations, and the resultant velocity changes were mapped by averaging spatially. I observed a large decrease in velocity near the seismogenic fault after the Kumamoto earthquake. The largest velocity decrease was observed around the Aso volcano, which became active after the Kumamoto earthquake. These observations provide important knowledge of the relationship between earthquakes and the activities of volcanoes.

Recently, the high-frequency ambient seismic noise generated from social activities of people, such as vibrations from traffic and constructions, is also used as the signal of geophysical explorations. This anthropogenic seismic noise is complex because many and an unspecified number of seismic sources exist. Anthropogenic seismic noise as a signal makes it possible to image and monitor the local subsurface structure by taking advantage of the existence of many seismic sources. Understanding the characteristics of anthropogenic seismic noise helps identify specific seismic sources which may be utilized as the signal of geophysical explorations. In Chapter 5, to understand the anthropogenic seismic noise, we monitored the magnitude of anthropogenic seismic noise and compared it to human activities during the COVID-19 pandemic. Although the outbreak of the COVID-19 has immensely impacted and restricted the routine lives of people worldwide, the large-scale restrictions on human activities during the pandemic also presented a rare opportunity to study the anthropogenic seismic noise because of the seismic sources are restricted. I investigated the variation in the magnitude of anthropogenic seismic noise in different periods and on different days of the week. In addition, since the estimated temporal variation showed clear seasonal variations, I modeled the seasonal variations by assuming a simple annual cycle based on the data of the past 2 years. I estimated corrected temporal variations of the noise level and found a clear relationship to people's economic and leisure activities. This finding also demonstrates that seismic noise can be used to monitor social activities.

In this study, I developed applications for imaging and monitoring underground structures using ambient seismic noise. The geophysical exploration using ambient seismic noise is versatile due to the constant presence of signals. Our studies improved the resolution and accuracy of the versatile method using ambient seismic noise and developed the monitoring approach. These improved applications can contribute to realize a society prepared for natural disasters and enable sustainable development. I summarize the details of important findings of this study and discuss future developments in Chapter 6.

Table of Contents

List of Figures

Chapter 1

Introduction

1.1. Research background

Constructing an accurate underground structure model and monitoring the underground state is essential to realize that society is prepared for natural disasters and enables sustainable development. In Japan, there is a high possibility of a major earthquake, such as the Nankai megathrust earthquake and the Tokyo inland earthquake, in the near future (Miyake & Koketsu, 2005; Sato et al., 2005). The high-resolution and accurate underground structure can simulate and predict the magnitude of ground motions of these earthquakes, and it can mitigate the possible damage from future earthquakes. The high-resolution and accurate underground structures are also needed for geothermal development and underground storage of radioactive waste and carbon dioxide. Since these developments will be run in long term, the monitoring system is required to maintain the safe and efficient development (Tsuji et al., 2021; Okamoto et al., 2021). I have conducted several studies about imaging and monitoring underground structures using ambient seismic noise included in seismic observations in this study.

The development of seismic observation networks has led to the storage of a massive amount of seismic observation data (Okada et al., 2004). These observations have provided various advantages and knowledge, such as early earthquake warnings, source estimation, and earthquake propagation properties. These observations include not only earthquakes but ambient seismic noise which is usually treated as the noise of earthquake observations. Ambient seismic noise consists mainly of low-frequency natural tremors and high-frequency anthropogenic seismic noise (Nishida, 2017; Lecocq et al., 2020). Since these vibrations are generated from atmospheric, oceanic, and other turbulent flows and social activities of people, which never disappear, ambient seismic noise is always present.

The seismic interferometry enabled to use these noises as signals and to conduct geophysical surveys by passive seismic observation, by computing cross-correlation of two stations' data (Snieder, 2004). Under the assumption that the extracted signals from cross-correlation of ambient noise consist mainly of dominant surface waves, we can estimate underground structure from the propagation properties of surface waves. Many studies were reported in various fields such as fault zone, volcanic areas, and seafloor due to the convenience of passive observation and the development of permanent observation (Nimiya et al., 2020;

Yamaya et al., 2021; Nagaoka et al., 2012). Furthermore, temporal change in underground structure can be estimated from a time series of cross-correlations, taking advantage of the constant presence of the ambient seismic noise (Nimiya et al., 2017; Taira et al., 2018). This technique is used to detect physical changes in underground structures by estimating changes in the seismic velocity of surface waves extracted from ambient seismic noise.

As described above, geophysical exploration using ambient seismic noise allow imaging and monitoring of underground structures using only passive observations. On the other hand, the spatial resolution and accuracy of estimated underground structure are poor compared to other geophysical survey such as reflection surveys. In addition, the number of studies on monitoring underground structures using time-series cross-correlation is limited, and the physical mechanism of velocity changes is still unclear. Although the approach using ambient seismic noise is highly versatile, there is still room for improvement.

1.2. Challenges of surface wave analysis using ambient noise

To solve various social issues such as disaster mitigation and resource development, improving the resolution and accuracy of the underground structure and developing monitoring techniques are necessary. In this study, I have developed and improved the geophysical exploration using ambient seismic noise to image and monitor the underground structure.

Imaging of underground structures using ambient seismic noise is performed using surface waves extracted by seismic interferometry. Using the dispersion curve of the surface waves, the S-wave velocity structure can be estimated by inversion. In previous studies, such as the microtremor array survey, the average surface wave dispersion curve was estimated from ambient seismic noise using several seismometers, and the 1D S-wave velocity structure was estimated (Yamanaka & Yamada, 2006). The tomography analysis using the estimated dispersion curve between two observation points has dramatically improved the spatial resolution of the S-wave velocity structure (Ekström, 2014). If there are enough observation points, the tomography analysis can estimate the S-wave velocity structure with high resolution. However, the spatial resolution depends on whether surface waves reflect the detailed structures. The sensitivity of surface waves in the spatial direction depends on the frequency. The higher-frequency surface waves can reflect smaller structures. Therefore, it is necessary to estimate the dispersion curve, including high frequencies, to estimate the three-dimensional S-wave velocity structure with high resolution using surface waves. In addition, the dispersion curve between two stations needs to be estimated for tomography analysis, which requires flexible analysis of a large amount of data.

Imaging the subsurface structures in basins using ambient seismic noise is more difficult. In regions where velocity contrast is strong, such as basement rock and sedimentary

layer, higher-order modes of surface waves are dominant (Boaga et al., 2013). The analysis of surface waves generally assumes that the fundamental mode is dominant. Therefore, the analysis in the basin area where the dominant higher-order modes should be carefully performed. On the other hand, if the dispersion curves of the fundamental mode and the higher-order modes can be estimated separately, the information of both modes can be used for more accurate inversion (Fu et al., 2022; Yamaya et al., 2021). A method for estimating dispersion curves of higher-order modes from fundamental modes of surface waves and accurate inversion analysis are required.

The monitoring of subsurface structures using ambient seismic noise is generally performed using the coda waves of surface waves extracted from ambient seismic noise (Nimiya et al., 2017; Taira et al., 2018). The reduction of seismic wave velocity due to earthquakes and volcanic eruptions has been reported (Brenguier et al., 2014). In addition, precipitation and seasonal variations have also been reported (Wang et al., 2017). In monitoring seismic wave velocity using seismic interferometry, the interpretation of the physical meaning of velocity change depends on the definition of coda wave and range of frequency (Obermann et al., 2013). In addition, when there is a specific source of ambient noise, it may reflect the change of the source rather than the geophysical change of subsurface structures. Furthermore, it is difficult to detect where the changes occur between two observation points. It is necessary to conduct wide-area observations of various natural phenomena and interpret them carefully.

Brenguier et al. (2019) applied seismic interferometry to the seismic noise from trains to monitor the underground. They showed that it is possible to monitor the subsurface using ambient seismic noise from human activity. However, anthropogenic noise is not well understood because many human activities attribute anthropogenic noise. Anthropogenic seismic noise in urban areas tends to be stronger and more complex following the growth of economic activities (Hong et al., 2020). If we can find sources that can be used to monitor the subsurface, such as trains, more advanced monitoring of the subsurface will be possible in urban areas.

1.3. Chapter description

To overcome the above challenges of surface wave analysis using ambient noise, I have developed a technique for imaging and monitoring. In Chapters 2 and 3, I treated the challenge of imaging high-resolution S-wave velocity structures. In Chapters 4 and 5, I treated the challenge of monitoring seismic velocity change. The details of each chapter are described below.

In Chapter 2, I visualized central Japan's subsurface S-wave velocity structure using surface waves extracted from ambient seismic noise (Nimiya et al., 2020). To visualize the

subsurface structure at a depth of several kilometers from the surface, it is essential to improve the horizontal resolution because complex structures such as faults system, valleys, and volcanoes exist. In this study, I estimated the Rayleigh-wave dispersion curves almost automatically from a huge data set of ambient noise and performed surface wave tomography analysis over a wide area. The horizontal resolution was improved by using higher frequency Rayleigh waves, which are sensitive to smaller structures. The estimated high-resolution three-dimensional S-wave velocity structure was used to interpret the complex geological structure of central Japan.

In Chapter 3, I estimated the subsurface structure of the Kanto Basin, where thick sedimentary layers exist. In Chapter 2, I tried to improve the horizontal resolution, but in the Kanto Basin, where thick sedimentary layers exist, the horizontal homogeneity is high, and the vertical resolution is important. In the basin structure, sedimentary layers exist on top of basement rocks. Therefore, the energy of higher modes of surface waves can be dominant due to the strong velocity contrast. The existence of higher-order modes makes it difficult to estimate the dispersion curve of the fundamental mode, because most the conventional microtremor array surveys estimate surface-wave phase velocities by assuming the fundamental mode of surface waves. In this study, taking advantage of the strong energy of higher modes of surface waves, I estimated dispersion curves of Rayleigh and Love waves from fundamental modes to some higher modes. Higher modes of surface waves are more sensitive to the velocity at the deeper part than fundamental modes, improving the resolution in the depth direction. Since Love and Rayleigh's waves are sensitive to the velocity at different depths, joint inversion was applied to estimate the subsurface structure with high vertical resolution.

In Chapter 4, I used ambient seismic noise to monitor the subsurface structures, taking advantage of the constant presence of the ambient seismic noise. I monitor the subsurface structures by monitoring the velocity of the surface waves. The surface wave that propagates between two stations can be extracted by calculating the cross-correlation of ambient seismic noise. I revealed the change in the subsurface structure during the 2016 Kumamoto earthquake (Nimiya et al., 2017). I observed a large decrease in velocity near the seismogenic fault after the Kumamoto earthquake. The largest velocity decrease was observed along with the Aso volcano, which became active after the Kumamoto earthquake. This chapter describes the details of these changes and their interpretation.

In Chapter 5, I monitored human activities during the COVID-19 pandemic using anthropogenic seismic noise included in ambient noise above 1 Hz (Nimiya et al., 2021). It has been reported that the magnitude of anthropogenic seismic noise increases with economic development. Therefore, anthropogenic seismic noise in urban areas is dominant and complex. The outbreak of the SARS-CoV-2 virus temporarily reduced economic activity in the world.

There has never been such an example of a temporary decrease in human activity, making this a very rare period to investigate anthropogenic seismic noise. In this context, I studied the effect of changes in anthropogenic activities during COVID-19 on the seismic noise levels in the Tokyo metropolitan area, Japan, considering the time of day, day of the week, and seasonal changes. This chapter presents the details of these fluctuations and their interpretation.

In Chapter 6, I summarize the important findings of this study and discuss future developments.

References

Boaga, J., Cassiani, G., Strobbia, C. L. & Vignoli, G. Mode misidentification in Rayleigh waves: Ellipticity as a cause and a cure. *Geophysics* **78**, (2013).

Brenguier, F., Campillo, M., Takeda, T., Aoki, Y., Shapiro, M., Briand, X., Emoto, K. & Miyake, H. Mapping pressurized volcanic fluids from induced crustal seismic velocity drops. *Science.* **345**, 80–82 (2014).

Brenguier, F. Boué, P., Ben-Zion, Y., Vernon, F., Johnson, C. W., Mordret, A., Coutant, O., Share, P.-E., Beaucé, E., Hollis, D. & Lecocq, T. Train Traffic as a Powerful Noise Source for Monitoring Active Faults With Seismic Interferometry. *Geophys. Res. Lett.* **46**, 9529–9536 (2019).

Ekström, G. Love and Rayleigh phase-velocity maps, 5-40 s, of the western and central USA from USArray data. *Earth Planet. Sci. Lett.* **402**, 42–49 (2014).

Fu, L., Pan, L., Li, Z., Dong, S., Ma, Q. & Chen, X. Improved High-Resolution 3D Vs Model of Long Beach, CA: Inversion of Multimodal Dispersion Curves From Ambient Noise of a Dense Array. *Geophys. Res. Lett.* **49**, (2022).

Hong, T.-K., Lee, J., Lee, G., Lee, J. & Park, S. Correlation between Ambient Seismic Noises and Economic Growth. *Seismol. Res. Lett.* (2020). doi:10.1785/0220190369.

Lecocq, T., Hicks, S. P., Van Noten, K., van Wijk, K., Koelemeijer, P., De Plaen, R. S. M., Massin, F., Hillers, G., Anthony, R. E., Apoloner, M.-T., Arroyo-Solórzano, M., Assink, J. D., Büyükakpınar, P., Cannata, A., Cannavo, F., Carrasco, S., Caudron, C., Chaves, E. J., Cornwell, D. G., Craig, D., den Ouden, O. F. C., Diaz, J., Donner, S., Evangelidis, C. P., Evers, L., Fauville, B., Fernandez, G. A., Giannopoulos, D., Gibbons, S. J., Girona, T., Grecu, B., Grunberg, M., Hetényi, G., Horleston, A., Inza, A., Irving, J. C. E., Jamalreyhani, M., Kafka, A., Koymans, M. R., Labedz, C. R., Larose, E., Lindsey, N. J., McKinnon, M., Megies, T., Miller, M. S., Minarik, W., Moresi, L., Márquez-Ramírez, V. H., Möllhoff, M., Nesbitt, I. M., Niyogi, S.,

Ojeda, J., Oth, A., Proud, S., Pulli, J., Retailleau, L., Rintamäki, A. E., Satriano, C., Savage, M. K., Shani-Kadmiel, S., Sleeman, R., Sokos, E., Stammler, K., Stott, A. E., Subedi, S., Sørensen, M. B., Taira, T., Tapia, M., Turhan, F., van der Pluijm, B., Vanstone, M., Vergne, J., Vuorinen, T. A. T., Warren, T., Wassermann, J. & Xiao, H. Global quieting of high-frequency seismic noise due to COVID-19 pandemic lockdown measures. *Science.* (2020). doi:10.1126/science.abd2438.

Miyake, H. & Koketsu, K. Long-period ground motions from a large offshore earthquake: The case of the 2004 off the Kii Peninsula earthquake, Japan. *Earth, Planets Sp.* **57**, 203–207 (2005).

Nagaoka, Y., Nishida, K., Aoki, Y., Takeo, M. & Ohminato, T. Seismic imaging of magma chamber beneath an active volcano. *Earth Planet. Sci. Lett.* **333**, 1–8 (2012).

Nimiya, H., Ikeda, T. & Tsuji, T. Three-dimensional S wave velocity structure of central Japan estimated by surface-wave tomography using ambient noise. *J. Geophys. Res. Solid Earth* **125**, 1–18 (2020).

Nimiya, H., Ikeda, T. & Tsuji, T. Spatial and temporal seismic velocity changes on Kyushu Island during the 2016 Kumamoto earthquake. *Sci. Adv.* **3**, e1700813 (2017).

Nimiya, H., Ikeda, T. & Tsuji, T. Temporal changes in anthropogenic seismic noise levels associated with economic and leisure activities during the COVID-19 pandemic. *Sci. Rep.* **11**, 1–13 (2021).

Nishida, K. Review Ambient seismic wave field. *Proc. Jpn. Acad., Ser.* **93**, 423–448 (2017).

Obermann, A., Planès, T., Larose, E., Sens-Schönfelder, C. & Campillo, M. Depth sensitivity of seismic coda waves to velocity perturbations in an elastic heterogeneous medium. *Geophys. J. Int.* **194**, 372–382 (2013).

Okada, Y., Kasahara, K., Hori, S., Obara, K., Sekiguchi, S., Fujiwara, H. & Yamamoto, A. Recent progress of seismic observation networks in Japan - Hi-net, F-net, K-net and KiK-net -. *Earth, Planets Sp.* (2004) doi:10.1186/BF03353076.

Okamoto, K., Asanuma, H. & Nimiya, H. Fluid activity detection in geothermal areas using a single seismic station by monitoring horizontal-to-vertical spectral ratios. *Sci. Rep.* **11**, 1–9 (2021).

Sato, H., Hirata, N., Koketsu, K., Okaya, D., Abe, S., Kobayashi, R., Matsubara, M., Iwasaki, T., Ito, T., Ikawa, T., Kawanaka, T., Kasahara, K. & Harder, S. Geology: Earthquake source fault beneath Tokyo. *Science.* **309**, 462–464 (2005).

Snieder, R. Extracting the Green's function from the correlation of coda waves: A derivation based on stationary phase. *Phys. Rev. E* **69**, 046610 (2004).

Taira, T., Avinash, N., Brenguier, F. & Manga, M. Monitoring reservoir response to earthquakes and fluid extraction, Salton Sea geothermal field, California. *Sci. Adv.* **4**, 1–11 (2018).

Tsuji, T., Ikeda, T., Matsuura, R., Mukumoto, K., Hutapea, F. L., Kumura, T., Yamaoka, K. & Shinohara, M. Continuous monitoring system for safe managements of CO_2 storage and geothermal reservoirs. *Sci. Rep.* **11**, 1–15 (2021).

Wang, Q. Y., Brenguier, F., Campillo, M., Lecointre, A., Takeda, T. & Aoki, Y. Seasonal crustal seismic velocity changes throughout Japan. *J. Geophys. Res. Solid Earth* **122**, 7987–8002 (2017).

Yamanaka, H. & Yamada, N. Estimation of 3D S-wave velocity model of the Kanto Basin, Japan, using Rayleigh wave phase velocity. *Bull. Earthq. Res. Inst.* **81**, 295–301 (2006).

Yamaya, L., Mochizuki, K., Akuhara, T. & Nishida, K. Sedimentary structure derived from multi-mode ambient noise tomography with dense OBS network at the Japan Trench. *J. Geophys. Res. Solid Earth* **126**, 1–20 (2021).

Chapter 2

Three-Dimensional S-Wave Velocity Structure of Central Japan Estimated by Surface-Wave Tomography Using Ambient Noise

Abstract

Many significant geological features in central Japan reflect the history of tectonic events such as volcanic eruptions, fault ruptures, and the collision of the Izu-Bonin arc. Because most previous studies focused on deep, large-scale structures at relatively low resolution or local structures using high-resolution data (e.g., active source seismic data), tectonic structures over a wide area throughout central Japan have not been characterized in detail. This study estimated three-dimensional S wave velocity structures with a high spatial resolution by extracting surface waves from 1-year-long ambient seismic data recorded by the Hi-net high-sensitivity seismograph network. I computed cross spectra of ambient noise data between station pairs and then extracted phase velocity dispersion curves using a frequency domain method. I developed an algorithm to calculate phase velocity and obtained numerous dispersion data. I then estimated the three-dimensional S wave velocity structure by applying a direct surface-wave inversion method. Our results clearly mapped heterogeneous features such as tectonic lines, sedimentary plains, and volcanic systems. I observed some low-velocity anomalies below volcanoes. Active fault zones identified as low-velocity zones were consistent with features on seismic reflection profiles. Several geological blocks related to the Izu collision were observed around the Izu Peninsula. I observed previously unreported geological features of the island of Honshu. Our high-resolution S wave velocity model can be used to interpret geological structures and hazard assessment of earthquakes.

Keywords: S-wave, velocity model, Surface wave inversion, Tomography

2.1. Introduction

On the island of Honshu, the largest island of Japan, there are many significant geological features that reflect the tectonic history of the island. The Itoigawa-Shizuoka Tectonic Line (ISTL) is a major fault system and one of the biggest geological boundaries in Honshu (green line in Fig. 2.1). This line divides the island into a western part and an eastern part. In addition, the southwest Japan arc is divided into two parts by the Median Tectonic Line (MTL) (red line in Fig. 2.1). The MTL gradually parallels the Japan arc and curves in southwest Japan as it approaches the ISTL. This curvature reflects the subduction of the Philippine Sea plate (Takahashi & Saito, 1997), which has caused the Izu-Bonin arc to collide with the Japan arc and has bent the MTL. Although the MTL is considered to continue to the east of the ISTL, its location is not clearly defined because of thick sediments and the complex deformation caused by the Izu collision. The northeast Japan arc is present in the eastern part of central Japan. In this area, there are numerous volcanoes because the Pacific plate is being subducted beneath the northeast Japan arc. Central Japan, therefore, has very complex underground structures. Identifying these tectonic features over a wide area and in high resolution is necessary to reveal these complex structures and deformations within the Japanese Islands.

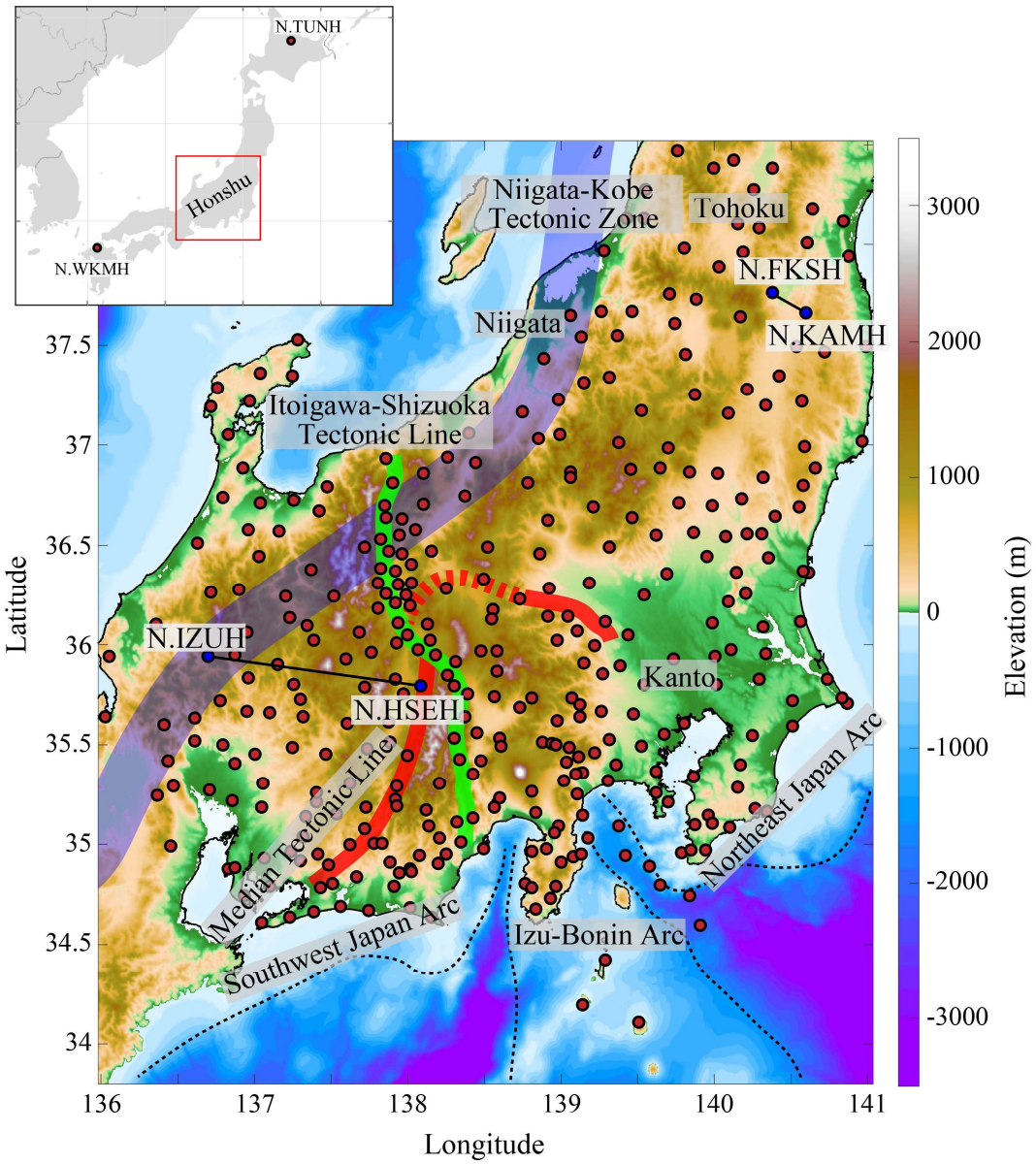

Figure 2.1. *Map of Honshu and main islands of Japan (inset), with locations of Hi-net stations (red and blue dots). The black solid lines connect the seismometer pairs (blue dots) shown in Fig. 2.4. The green line indicates the Itoigawa-Shizuoka Tectonic Line. The red line indicates the Median Tectonic Line, which is not clearly defined east of the Itoigawa-Shizuoka Tectonic Line (dashed portion). The blue line indicates Niigata-Kobe Tectonic Zone. I draw the tectonic lines and tectonic zone of Takahashi 2006 and Sagiya et al. 2000.*

Seismic tomography plays an important role in clarifying the origin of these complex tectonic features (e.g., Shapiro et al., 2005; Yang et al., 2008). The configuration of the tectonic plates in Japan has been determined from their three-dimensional seismic velocity structure by P- and S-wave travel-time tomography using local earthquakes (e.g., Matsubara et al., 2008; Nakajima et al., 2009). Although such body-wave tomography effectively estimates

underground structures, its spatial resolution is limited by the density of receivers and the distribution of natural earthquakes. Using temporarily deployed seismic stations, many local body-wave tomographies (e.g., Kato et al., 2008; Yukutake et al., 2015) have been conducted to construct the shallow three-dimensional seismic velocity structure. However, the coverage of these surveys was limited because it was difficult to deploy temporal high-density seismic stations in a wide area. Furthermore, to investigate the details of shallow structures, many active-source seismic surveys (e.g., Ikami et al., 1986; Ikeda et al., 2009; Ishiyama et al., 2013) microtremor array surveys (e.g., Satoh et al., 2001) have been conducted. Although these surveys can obtain 1D or 2D detailed structures, it is difficult to construct three-dimensional seismic velocity structures. Thus, constructing high-resolution, shallow, three-dimensional structures over a wide area is a challenging task.

Surface-wave tomography using ambient noise has been applied to estimate subsurface structures since the recent development of permanent high-quality seismic networks (e.g., Lin et al., 2008; Shapiro et al., 2005). Because ambient noise is usually dominated by surface waves (Ekström, 2001), surface waves propagating between two seismometers can be extracted by using seismic interferometry; active sources or earthquakes are not required (e.g., Lobkis & Weaver, 2001; Snieder, 2004; Wapenaar & Fokkema, 2006). S-wave velocity structures can be estimated from the dispersion characteristics of surface waves. Estimation of surface-wave dispersion curves between many station pairs enables estimation of a three-dimensional S-wave velocity model using tomographic methods. Most previous studies of surface-wave tomography using data from a permanent seismic network have focused on deep structures (tens to hundreds of kilometers deep) using low-frequency surface waves (e.g., Chen et al., 2018; Nishida et al., 2008). The surface-wave tomography should include surface-wave dispersion data at relatively short interstation distances and high frequencies to construct a high-resolution three-dimensional S-wave velocity model. Phase velocity information at short interstation distances improves the accuracy of tomographic analyses (Ekström et al., 2009; Luo et al., 2015), and higher-frequency surface-wave dispersion data reflect smaller-scale geological structures (Yang & Forsyth, 2006).

To investigate shallow (<10 km) structures at a high spatial resolution, I estimated three-dimensional S-wave velocity structures by applying surface-wave tomography at frequencies higher than conventional surface-wave tomography (0.2–0.6 Hz). I calculated the surface-wave phase velocity between station pairs in the frequency domain to avoid the limitations of interstation distance. Furthermore, I extended the surface-wave phase velocity at each pair of stations to a higher frequency range by using the envelope of the amplitude of the extracted signal, which was dominated by surface waves. I then estimated the high-resolution shallow three-dimensional S-wave structure of central Japan by applying a direct surface-wave tomographic method. My estimated shallow S-wave velocity structure revealed geological

features such as tectonic lines, sedimentary plains, and volcanic systems. In addition, several crustal blocks that may correspond to microplates were observed around the Izu collision area. Our results contribute to the interpretation of the deformation features of the islands of Japan.

2.2. Data and Methods

I used the vertical component of the seismic data recorded by high-sensitivity seismograph network (Hi-net) stations maintained by the National Research Institute for Earth Science and Disaster Resilience (NIED) from 1 December 2015 to 31 November 2016. Hi-net stations are equipped with short-period velocity sensors with a natural frequency of ~1 Hz and deployed in boreholes at depths of at least 100 m to reduce the influence of cultural noise (Obara et al., 2005). About 800 Hi-net stations are deployed throughout Japan. In this study, I used data from 364 stations distributed in central Honshu (dots in Fig. 2.1).

To construct a three-dimensional S-wave velocity structure model, I first extracted surface waves propagating between two stations by computing the cross-correlation of the ambient noise. I then estimated surface-wave phase velocity dispersion curves at each pair of stations by using a frequency-domain method (zero-crossing method; Ekström et al., 2009) as the basis of the spatial autocorrelation (SPAC) calculation (Aki, 1957). Finally, I inverted the phase velocity dispersion curves to construct a three-dimensional S-wave velocity structure by applying a direct surface-wave tomographic method (DSurfTomo; Fang et al., 2015). The detailed procedures used in each processing step are as follows.

2.2.1 Preprocessing and Cross-correlation

I divided one-day continuous ambient noise data into 30-min segments with a 50% overlap (Seats et al., 2012). I then subtracted the mean of each segment, corrected the instrumental response, and applied a 0.1–0.9 Hz band-pass filter to each segment. To reduce the influence of natural earthquakes in this method, segments in which the maximum absolute amplitude exceeds a specified threshold are removed (Bensen et al., 2007; Seats et al., 2012). I removed segments with RMS amplitudes ≥2.2 times the mean RMS amplitude for each day. I computed power-normalized cross spectra for each segment and then stacked them to create annual data.

I succeeded in observing the surface-wave propagation in the time domain of the stacked cross spectra, which were calculated by binning stacks (Fig. 2.2a). To check the azimuthal distribution of the ambient noise source, I computed the relative amplitude ratios of the positive and negative windows of the cross-correlation functions (Fig. 2.2b). If the noise sources were distributed randomly, the amplitudes of these windows would be symmetrical. In our data, differences in these amplitudes were relatively small, yielding relative amplitude

ratios of ~0.5 to 1.5 (Gu et al., 2019). Thus, I conclude that the noise source distribution did not significantly affect our results (Yao & van der Hilst, 2009).

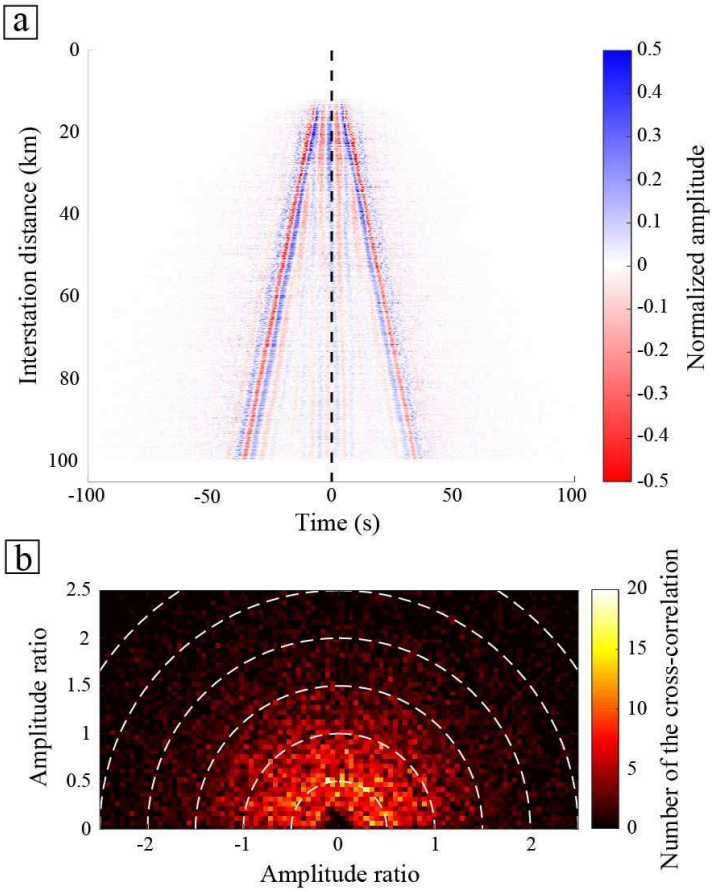

Figure 2.2. *(a) Binning stacks of the cross-correlation functions. The bin width is 0.1 km, and a 0.1–0.9 Hz band-pass filter was applied to each trace. The peak of the amplitude indicates the arrival time of the dominant surface waves. (b) Azimuthal distribution of the amplitude ratio between the maximum envelope amplitudes of the positive and negative windows of the cross-correlation functions. The azimuth of the value gives the azimuth of each station pair.*

2.2.2 Estimation of Phase Velocity Dispersion Curve

I applied a zero-crossing method to estimate the phase velocity between two seismometers (Ekström et al., 2009). References to determine unique phase velocity dispersion curves are required in this method. Therefore, I followed two steps. The first step is to estimate the phase velocity map at 0.2 Hz. In the second step, I applied a zero-crossing method by using the phase velocity map at 0.2 Hz as the reference velocity. I first explained how to estimate reference velocity map in short, followed by how to estimate the phase velocity between two seismometers using zero-crossing method.

2.2.3 Estimation of Reference Velocity Map

Using the extended SPAC method (Okada, 2003), I estimated the phase velocity map at 0.2 Hz as the reference velocity. To estimate reference velocity at each location, I meshed our study region with 47 by 50 grid points with an interval of 0.1° in latitude and longitude. I collected station pairs at one grid if the interstation distance ranges from 50 to 100 km, and the midpoint is located in this grid or grids surrounding this grid (Fig. 2.3a). Then, I estimated phase velocity with a 2.5 to 3.5 km/s velocity range in the frequency range from 0.15 to 0.25 Hz at each grid by applying the extended SPAC method (Okada 2003) to collected station pairs. The phase velocities at 0.2 Hz were then estimated by the linear interpolation of phase velocities from 0.15 to 0.25 Hz (Fig. 2.3b) to reduce the fluctuation of phase velocity at 0.2 Hz. To measure the stability of reference velocity at each grid, I calculated the root mean square error (RMSE) between original phase velocities and lineally interpolated phase velocities from 0.15 to 0.25 Hz (Fig. 2.3c). If the RMSE is more than 0.25 km/s, I removed phase velocity and obtained a reference velocity map using linear extrapolation (Fig. 2.3d).

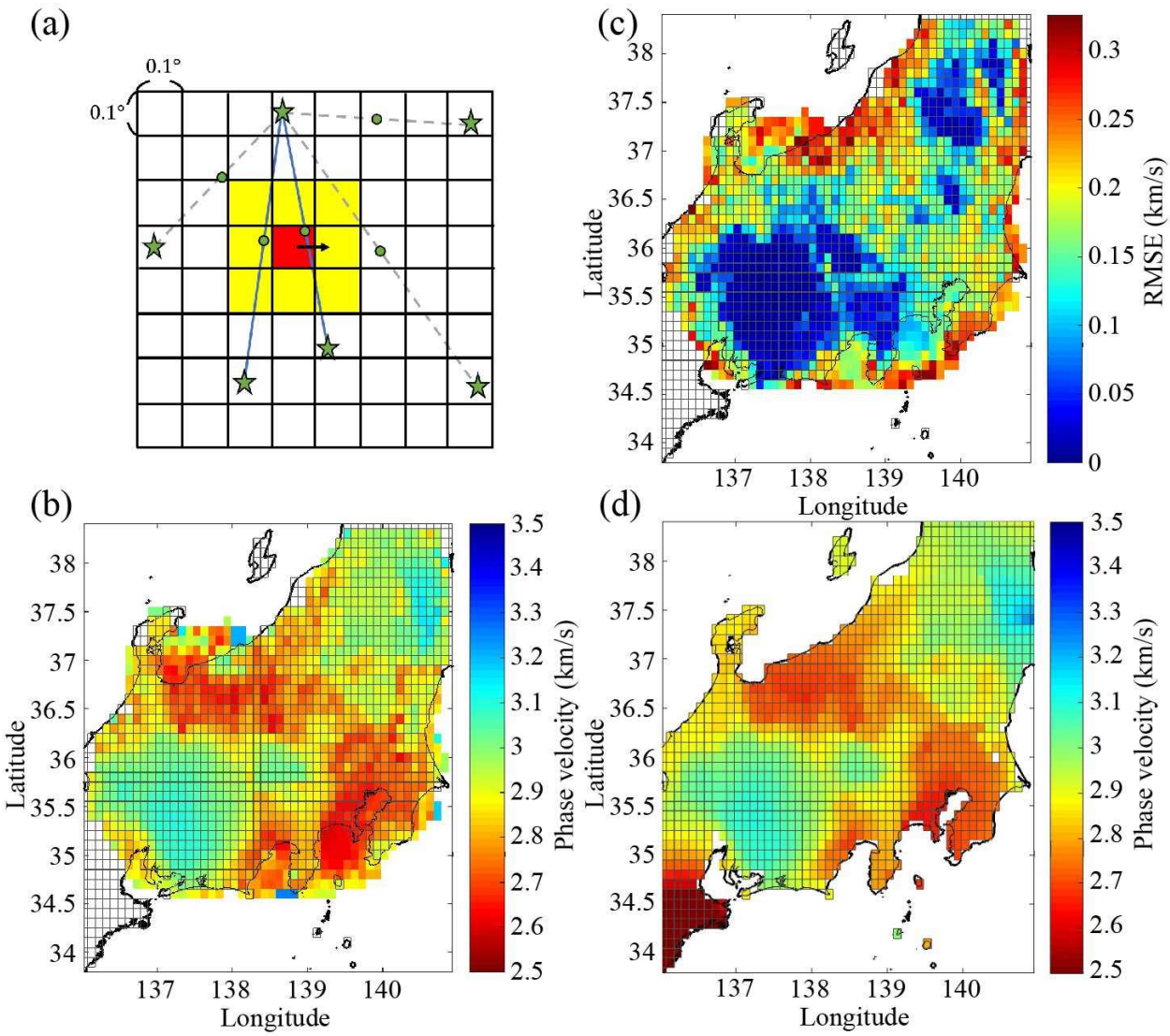

Figure 2.3. *Processing to estimate reference velocity map. (a) Collecting station pairs to apply the extended SPAC method. Green stars indicate stations. Solid and dashed lines show used and unused station pairs; I used only station pairs of which the midpoint (green dots) is located in red or yellow grids. (b) Original phase velocity map including unstable (high RMSE) data. (c) RMSE map of (b). (d) Final reference velocity map after removing unstable data.*

2.2.4 Estimation of Dispersion Curves Between Two Seismometers

I applied a zero-crossing method (Ekström et al., 2009). This method can estimate the phase velocity in the frequency domain based on the SPAC method (Aki, 1957). In the SPAC method, assuming that ambient noise is dominated by surface waves propagating isotopically allows the real part of the cross spectra to be modeled as a Bessel function of the first kind of order zero as follows:

$$\mathrm{Real}\big(\rho(f,\Delta x)\big) = J_0\left(\frac{2\pi f \Delta x}{C(f)}\right), \tag{2.1}$$

where Δx is the distance between two seismometers, J_0 is the Bessel function of the first kind of order zero, and $C(f)$ is the phase velocity. We usually applied a grid search algorithm to estimate the phase velocity by fitting the observed cross spectra to a Bessel function with Eq. (2.1). In using the zero-crossing method proposed by Ekström et al. (2009), I fit only zero crossings of the observed cross spectra with zero points of the Bessel function as follows:

$$C_m(f_n) = \frac{2\pi f_n \Delta x}{Z_{n+2m}}, \tag{2.2}$$

where f_n is the frequency of the nth observed zero of the cross spectra, Z_{n+2m} is the nth zero of the Bessel function, and m $(= 0, \pm 1, \pm 2, \cdots)$ is the number of missed or extra zero points.

On the one hand, interstation distances shorter than two or three wavelengths are not usually used in time-domain studies because of the far-field approximation required in time-domain analysis (Ekström et al., 2009; Luo et al., 2015; Shapiro et al., 2005). On the other hand, the zero-crossing method has no theoretical limit to its applicability at short station separations (Ekström et al., 2009). This method is a simple technique to extract the phase velocity directly from the zero crossings of the cross spectra, and this simplicity allows for the automated processing of large amounts of data (Ekström et al., 2009; Kästle et al., 2016).

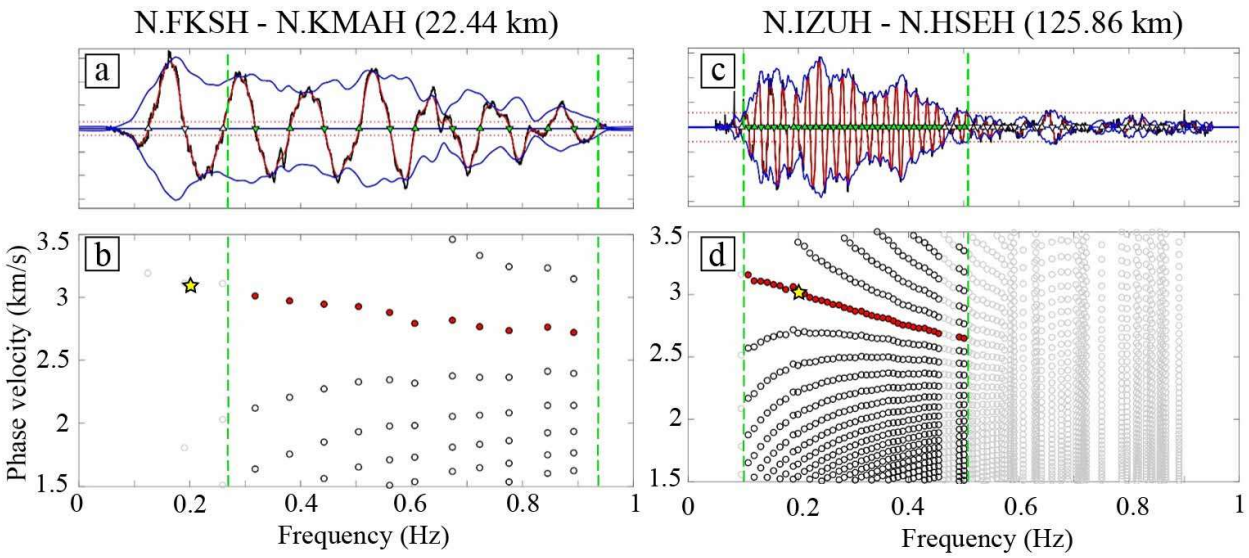

Figure 2.4. *Processing of cross spectra to estimate the phase velocity dispersion curve. (a) Real part of stacked, normalized cross spectra between stations N.FKSH and N.KMAH before (black) and after (red) smoothing. The Green dashed line shows the effective frequency range defined by using the envelope (blue) and threshold (dashed magenta) (see text for details). Green triangles indicate the zero crossings of smoothed cross spectra. (b) Phase velocities from the zero crossings of cross spectra (red dots). Each zero crossing can be explained by several possible phase velocities, as indicated by the black open circles. The reference velocity is shown as a yellow star. (c), (d) Same as (a) and (b) but for stations N.IZUH and N.HSEH. Station locations are given in Fig. 2.1.*

Figure 2.4 shows two examples of the stacked normalized cross spectra and estimation of phase velocity using the zero-crossing method. I obtained zero crossings from the smoothed cross spectra to reduce missed or extra zero crossings. In this study, I applied a running average with the Parzen window, the length of which is one-third the separation of zero crossings (Ekström, 2014). Several possible phase velocities can explain each zero crossing (black open circles in Figs. 2.4b and d).

Because several possible phase velocities were estimated at each frequency, phase velocity dispersion curves could not be uniquely determined without a reference velocity. To overcome this problem, I picked surface-wave dispersion curves using a reference velocity map at 0.2 Hz (Fig. 2.3d). I first picked the velocity closest to the reference velocity, which was the average velocity of the phase velocity map between pairs of stations (yellow stars in Figs. 2.4b and d). In the frequency range lower than 0.2 Hz, I chose the phase velocity closest to the previously picked phase velocity because the differences in phase velocity between other possibilities at each frequency were large. In the frequency range higher than 0.2 Hz, I chose the phase velocity closest to the approximate straight line, which was calculated from the

chosen four closest phase velocities. If the number of zeros is smaller than four in the frequency range lower than 0.2 Hz (e.g., Fig. 2.4b), I expanded this frequency range until I picked at least four phase velocities. When the envelope of a real part of the cross spectra was small (blue line in Figs. 2.4a and c), I sometimes observed unstable phase velocities because smaller values of the cross spectra easily introduced extra zero crossings due to noise. I, therefore, defined the effective frequency range (green dashed line in Figs. 2.4a and c) based on the envelope of the cross spectra to estimate accurate dispersion curves. In this study, I defined the frequency range where the amplitude of the envelope of the real part of the cross spectra was larger than the threshold (magenta dashed lines in Figures 2.4a and c) as the effective frequency range. To define the threshold, I calculated the stacked normalized cross spectra between stations N.TUNH and N.WKMH (locations are shown in the inset of Fig. 2.1). Because the distance between N. TUNH and N. WKMH was long (~1578 km), surface waves included in ambient noise in the analyzed frequency range (0.1 to 0.9 Hz) would not propagate between these stations because of attenuation. I assumed that the resulting cross spectra represented the level of uncorrelated noise and used 100 times the mean value of the envelope from 0.1 to 0.9 Hz as the threshold. Finally, I automatically obtained about 12,000 dispersion curves (Fig. 2.5). Because the estimations were automatic, some of the dispersion curves were unstable. I, therefore, excluded some unstable dispersion curves manually.

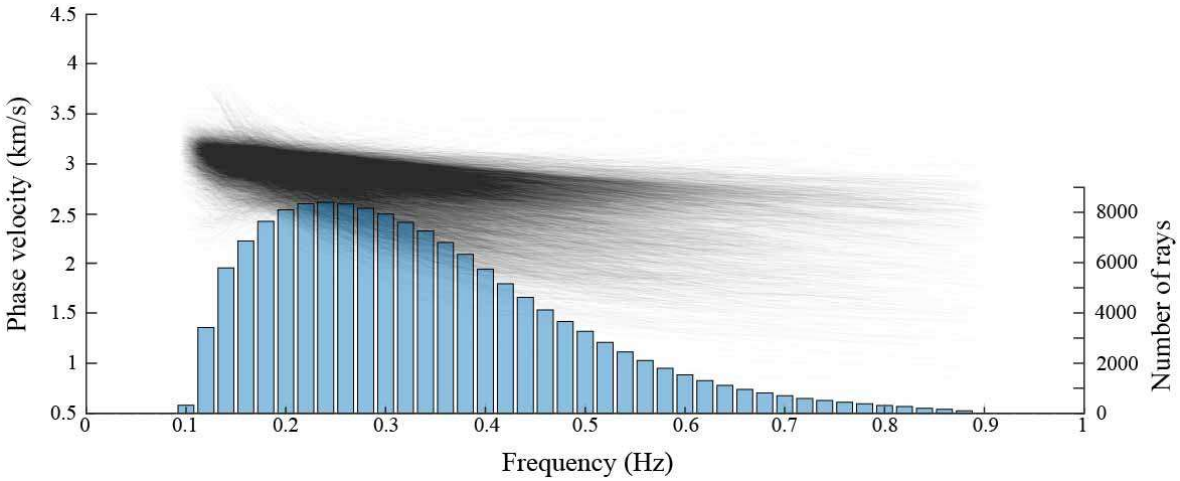

Figure 2.5. *Estimated dispersion curves and a number of rays at each frequency.*

2.3. Three-dimensional S-wave Velocity Structure by Surface-wave Tomography

I used a direct surface-wave tomography method (DSurfTomo) to estimate three-dimensional S-wave velocity structures from phase velocity dispersion curves between station pairs (Fang et al., 2015). In surface-wave tomography analyses, the three-dimensional S-wave

velocity model is usually constructed by pointwise inversion using 2D phase velocity maps for 1D S-wave velocity profiles at each grid point. However, recent studies (e.g., Boschi & Ekström, 2002; Fang et al., 2015; Pilz et al., 2012) have demonstrated that a three-dimensional velocity model can be estimated by direct inversion of dispersion data without constructing intermediate-phase velocity maps. Some of these direct inversion approaches do not update sensitivity kernels and ray paths for newly created three-dimensional models. The consequence is a biased wave velocity estimation in a complex medium such as the shallow crust. DSurfTomo avoids the intermediate step of inversion for the phase velocity map, and the sensitivity kernels are updated iteratively. In addition, this method uses the fast-marching method (Rawlinson & Sambridge, 2004) to account for the ray-bending effects of the frequency-dependent ray paths. Considering the ray-bending effect in inversion is particularly useful for high-frequency surface waves which are sensitive to heterogeneous shallow crustal structure (Fang et al., 2015; Gu et al., 2019). This tomography can therefore be effective for estimating the heterogeneous velocity structure of Honshu by using surface waves that include high frequencies. The simple explanation of the inverse problem used in DSurfTomo is as follows.

In the inversion, the optimal model $\mathbf{m}$ minimizes the differences $\delta t_i(f)$ between the observed travel times $t_i^{obs}(f)$ and the synthetic travel time $t_i(f)$ calculated from the model. The travel-time difference at frequency f for path i is given by

$$\delta t_i(f) = t_i^{obs}(f) - t_i(f) \approx -\sum_{k=1}^{K} v_{ik} \frac{\delta C_k(f)}{C_k^2(f)}, \tag{2.3}$$

where $t_i(f)$ is the calculated travel time from a reference model, which can be updated in the inversion, the v_{ik} are the bilinear interpolation coefficients along the ray path associated with the ith travel-time datum, and $C_k(f)$ and $\delta C_k(f)$ are the phase velocity and its perturbation at the kth 2D surface grid point at frequency f, respectively. Typically, surface wave dispersion is most sensitive to the S-wave velocity. However, high-frequency Rayleigh wave dispersion also has a significant sensitivity to P-wave velocity in the shallow crust (Fang et al., 2015). The Rayleigh wave phase velocity was therefore converted to an S-wave velocity using the relationship between P-wave velocity and density; the scaling factors $R_\alpha(z_j)$ and $R_\rho(z_j)$ in Eq. (4) were derived empirically by using a diverse dataset (e.g., borehole logs, vertical seismic profile and laboratory measurements) (Brocher, 2005). Thus, Eq. (2.3) can be rewritten as (Fang et al., 2015)

$$\delta t_i(f) = \sum_{k=1}^{K}\left(-\frac{v_{ik}}{C_k^2}\right)\sum_{j=1}^{J}\left[R_\alpha(z_j)\frac{\partial C_k}{\partial \alpha_k(z_j)} + R_\rho(z_j)\frac{\partial C_k}{\partial \rho_k(z_j)} + \frac{\partial C_k}{\partial \beta_k(z_j)}\right]\Big|_{\theta_k}\delta\beta_k(z_j) \quad (2.4)$$
$$= \sum_{l=1}^{M} G_{il} m_l,$$

where θ_k represents the 1D reference model at the kth surface grid point on the surface and $\alpha_k(z_j)$, $\beta_k(z_j)$, and $\rho_k(z_j)$ are the P-wave velocity, S-wave velocity, and mass density at the jth node in the depth direction, respectively. The total number of grid points of the three-dimensional model is $M = KJ$.

The direct surface-wave tomography described by Eq. (2.4) can be further formulated in matrix form as

$$\mathbf{d} = \mathbf{Gm}, \quad (2.5)$$

where $\mathbf{d}$ is the surface-wave travel-time residual vector for all ray paths at different frequencies, $\mathbf{G}$ is the data sensitivity matrix, and $\mathbf{m}$ is the model parameter vector. Damping and first-order smoothing regularizations are applied to make the inversion stable.

For the inversion grid, the study region was meshed with 170 by 210 grid points with an interval of 0.025° in latitude and longitude. I used 10 grid layers (0–9 km) for the depth direction. Because of computer memory limitations for the calculation, I divided the grids into 42 subareas with about 75% overlapping (Fig. 2.6b). Each subarea had 70 by 90 grid points. I tested several damping and smoothing parameters to determine the optimal ones. As a rule of thumb, the fundamental mode Rayleigh wave phase velocity is most sensitive to the S-wave velocity at depths around 1/3 of its corresponding wavelength. For a uniform half-space Poisson solid, the phase velocity $c = 0.92\beta$, where β is the S-wave velocity (Shearer, 2009). I, therefore, chose an initial S-wave velocity model that was close to the average of the estimated phase velocities times 1.1 ($\beta \approx 1.1c$) at the depth of 1/3 of the wavelength in each subarea (Fig. 2.6).

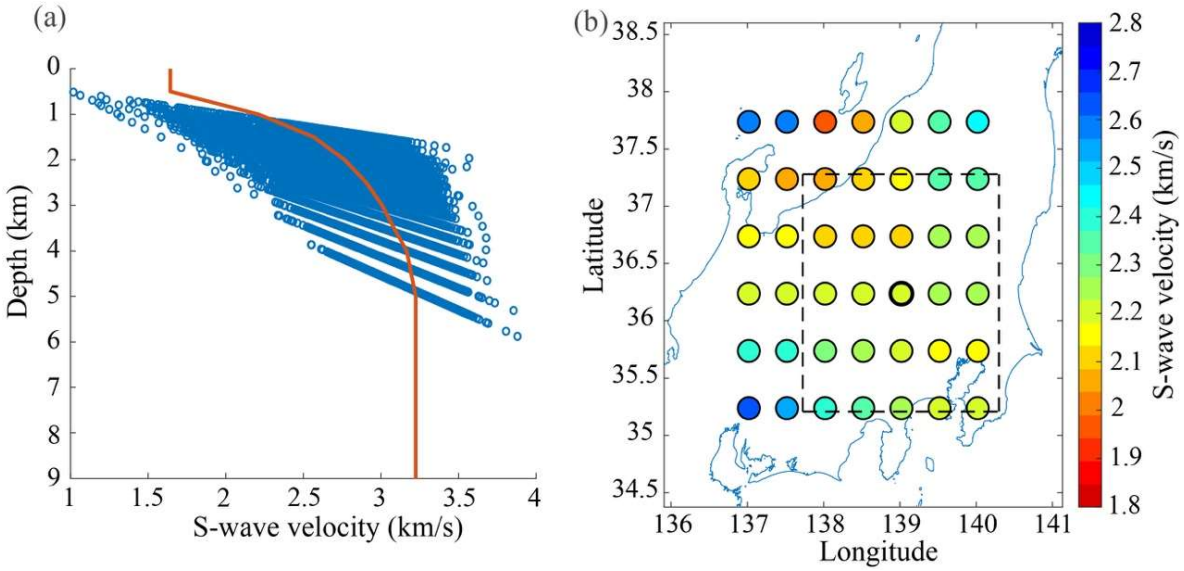

Figure 2.6. *(a) Transformation of phase velocity to a depth-S-wave velocity approximation profile in the subarea (black dashed square in Fig. 2.6b). For each dispersion data, I converted 1/3 of wavelength to depth and 1.1 times phase velocity to S-wave velocity (blue circles). The averaged velocity at each depth (red line) is used as the initial reference S-wave velocity model in the inversion. (b) The initial reference S-wave velocity at 1 km depth in all subareas. The color of each circle shows the initial reference S-wave velocity. Each circle indicates the center of its subarea. The black dashed line indicates the bold circle's subarea.*

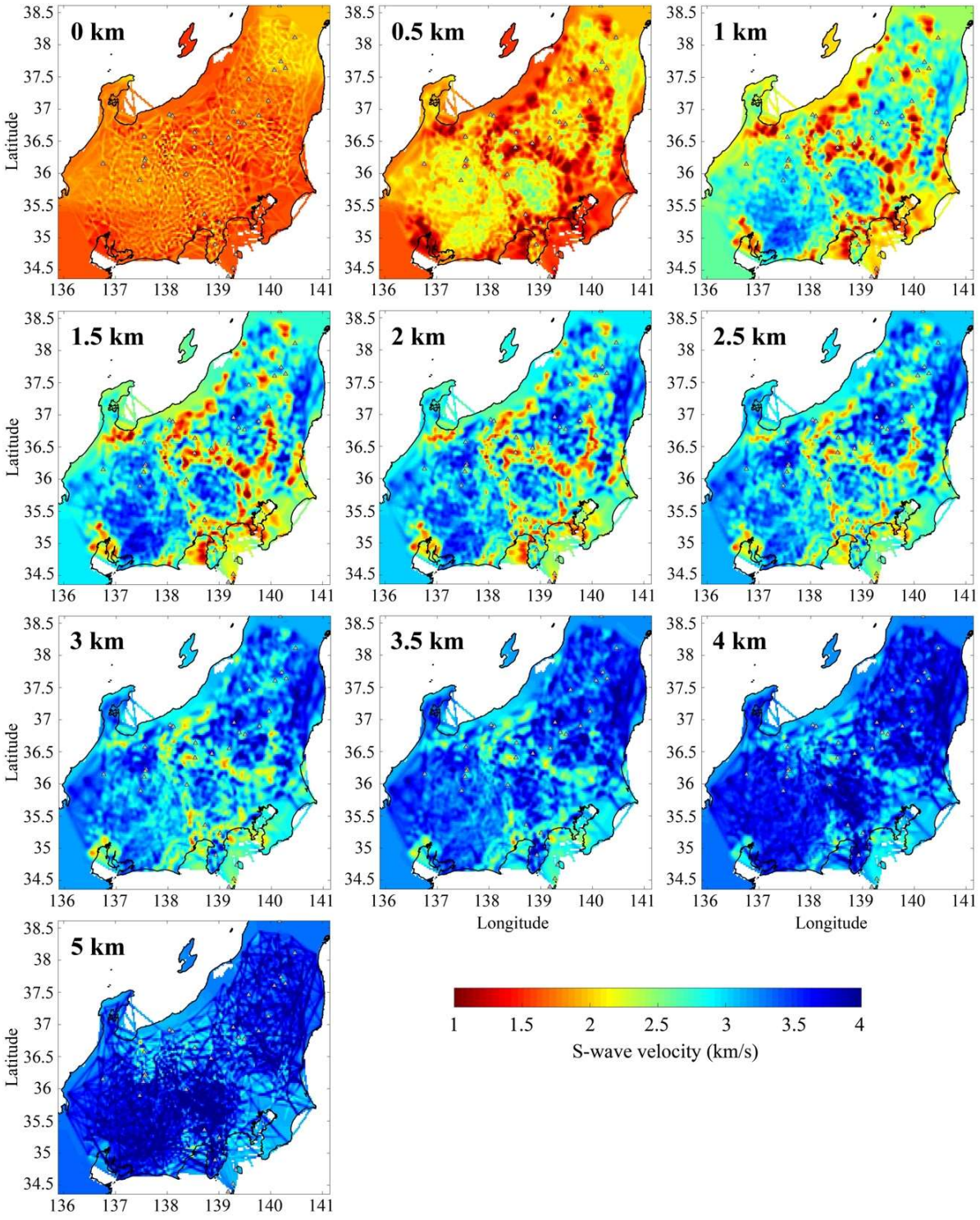

Figure 2.7. *Results of the inversion at the surface of each layer. Gray triangles show active volcanoes.*

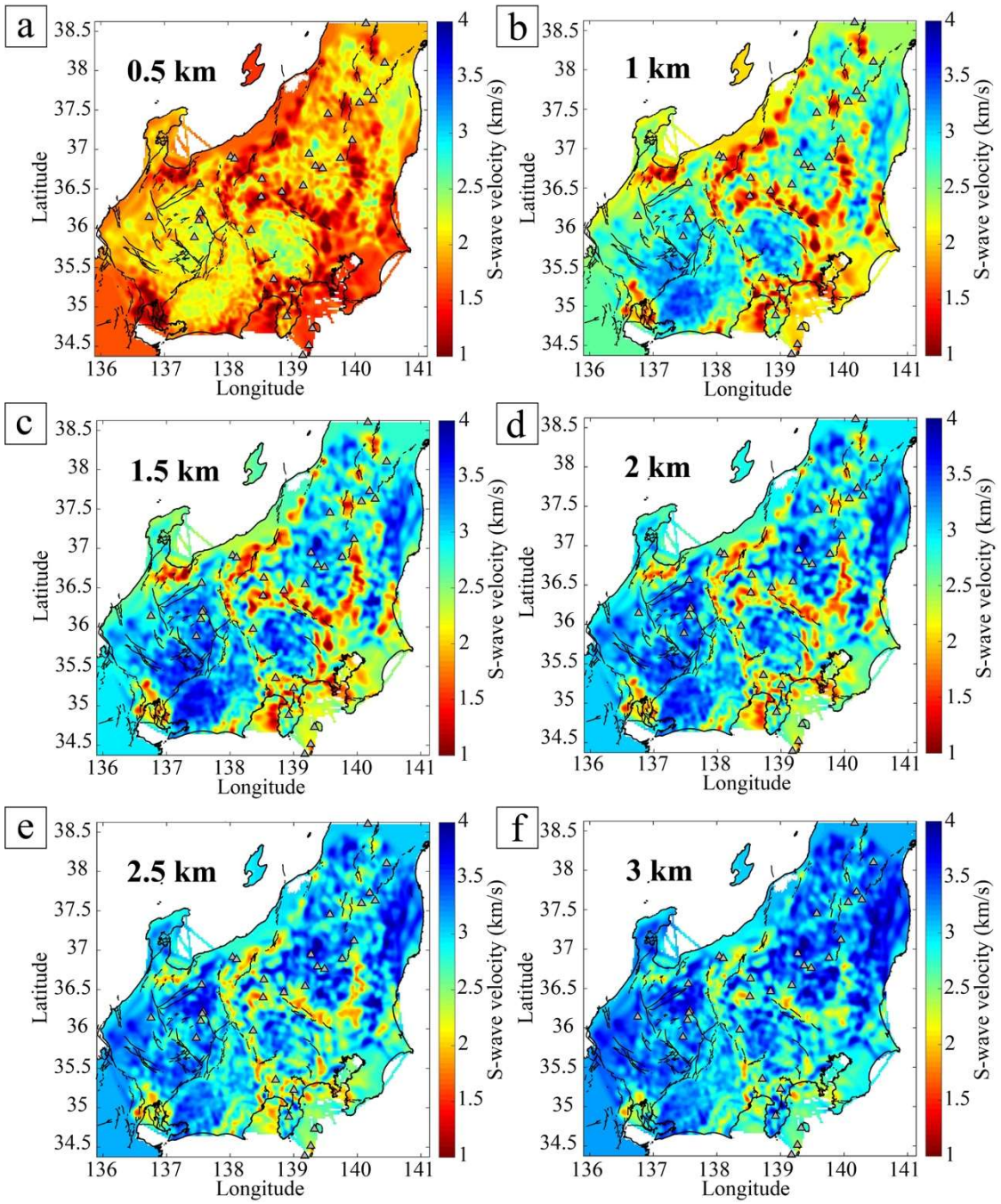

Figure 2.8. *S-wave velocity model before topographic correction at different depths (upper left of each panel). Black lines indicate active faults. Gray triangles show active volcanoes.*

2.4. Results

To derive a smooth, three-dimensional S-wave velocity model from the layered three-dimensional S-wave velocity model estimated by direct inversion (Fig. 2.7), I applied a linear interpolation technique in the slowness domain. First, I interpolated vertical layers at

each horizontal grid, followed by horizontal grids at each interpolated layer. After that, I added vertical shifts to the inverted velocity model to correct the elevation at each grid because the inversion is based on the assumption of the flat surface (results before topographic correction are shown in Fig. 2.8). The depth shown in following figures is therefore the depth below sea level.

Figure 2.9 shows the resultant S-wave velocity structures at six different depths. The high-velocity zones basically correspond to mountainous areas (Figs. 2.1 and 2.9). Thin, low-velocity zones were observed at many locations, and most of them were observed along valleys or active faults (Figs. 2.1 and 2.9). The locations of thin, low-velocity anomalies in the northern and western parts of our study area were very consistent with the locations of active faults (area D in Fig. 2.9b). However, it was difficult to detect faults directly using surface waves because the width of the faults was thinner than the wavelengths of the surface waves used in this study. Therefore, these thin, low-velocity zones reflected the thick, soft sediments deposited in graben caused by a fault.

In a previous study using surface waves, Nishida et al. (2008) estimated a three-dimensional S-wave velocity model down to a depth of 50 km using low-frequency surface waves recorded by a tiltmeter (0.05–0.2 Hz). Although low-frequency surface waves are sensitive to deeper structures, it is difficult to resolve small structures accurately. Our study used higher-frequency (0.2–0.6 Hz) surface waves that could reflect detailed structures. When I decreased the spatial resolution of our results by changing the damping and smoothing parameters of the inversion, the smoothed results were similar to the S-wave velocity model of Nishida et al. (2008) (Fig. 2.10).

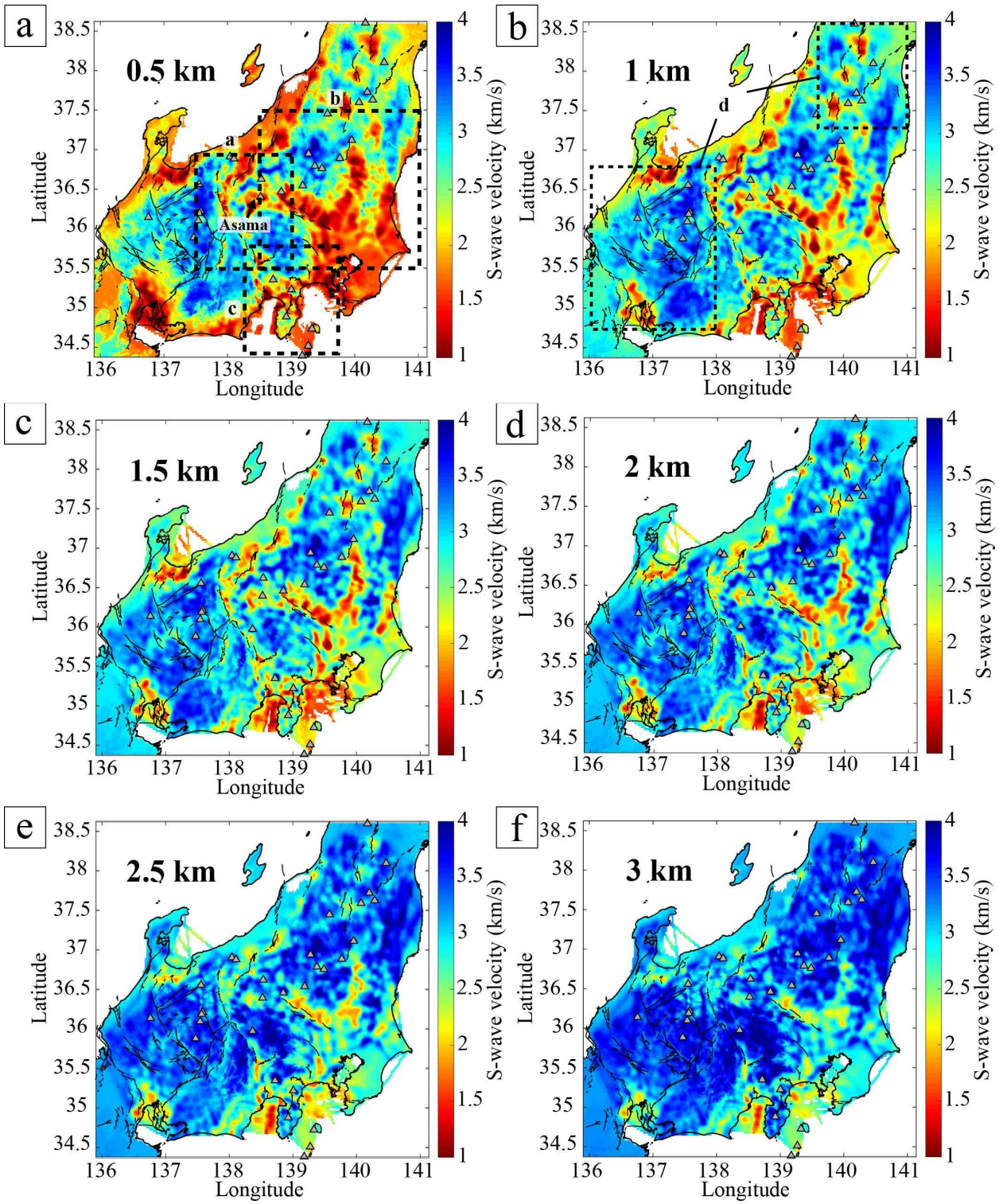

Figure 2.9. *S-wave velocity model at different depths below sea level (upper left of each panel). Black lines indicate active faults (retrieved 25 October 2019 from http://www.j-shis.bosai.go.jp/map/). Gray triangles show active volcanoes.*

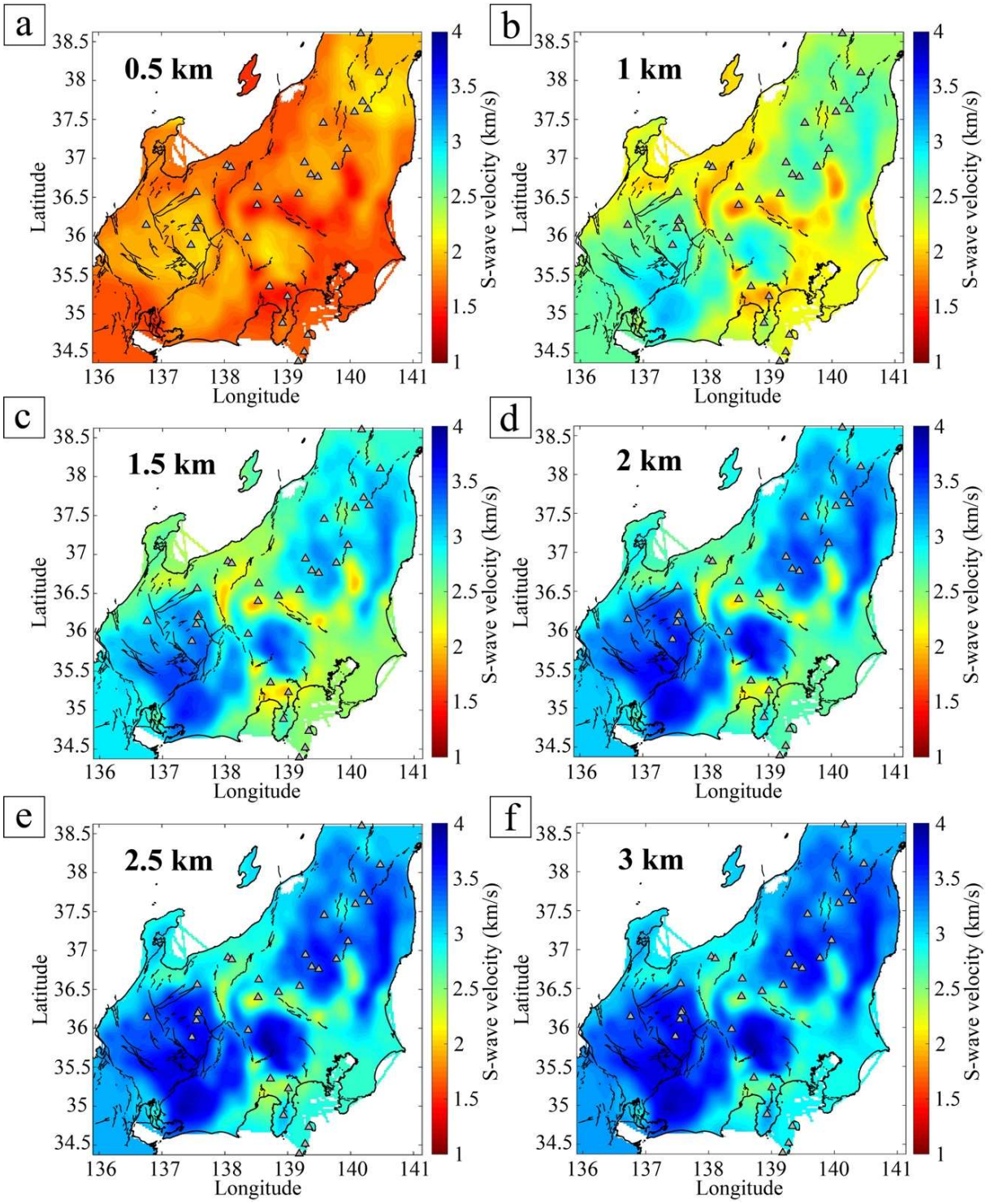

Figure 2.10. *S-wave velocity model using strong smoothing parameter before topographic correction at different depths (upper left of each panel). Black lines indicate active faults. Gray triangles show active volcanoes.*

To consider the reliability of our results, I first checked the ray-path coverage at different frequencies and performed a checkerboard resolution test. Figure 2.11 shows the ray

paths at two different frequencies (0.2 and 0.5 Hz) based on the final three-dimensional velocity model. It is apparent that the ray-path coverage was relatively good, except for the Kanto and Niigata areas (Figs. 2.1 and 2.11). To further evaluate the spatial resolution of our inverted model, I performed a checkerboard resolution test (Fig. 2.12). I simulated the input anomalies at each depth with a sine function for horizontal direction, and the range of the amplitudes varied from about 70% to 130% of the depth-dependent reference velocity $v = 2 + 0.2d$ (km/s), where d is depth (km). The synthetic interstation travel times were calculated in the same source-receiver distribution as the real data distribution. Each anomaly had a size of about 15 km.

Most inversion models recovered the checkerboard pattern, except around Kanto and Niigata (Fig. 2.12). However, the value of the velocity variation could not be accurately recovered in some places. The implication is that our model could accurately reflect the shape of the velocity anomaly, but it might overestimate or underestimate the value of the estimated S-wave velocities. Around the coast of Niigata, the inversion models were insensitive because there was no proximate Hi-net station (Figs. 2.1 and 2.12). Although there were many Hi-net stations in the Kanto area, some of them were deployed in boreholes with depths up to ~3.5 km from the surface because the sediments were thick. It was difficult to extract surface waves at these stations using seismic interferometry. When I extracted surface waves, it was difficult to pick optimal phase velocities using the same selection algorithm because the thick, soft sediments caused the dispersion of velocity to be strong and the estimations of dispersion curves around Kanto to be unstable. I did not use obviously unstable dispersion curves in the inversion. The inversion models around Kanto could therefore not recover the checkerboard pattern.

Furthermore, I estimated the standard deviation of the S-wave velocity model from randomly selected data to confirm the accuracy of the inversion models. I estimated 50 S-wave velocity models by randomly selecting 80% of the total dispersion data without repetition at each subarea. I estimated the standard deviation except for outer subareas because of computer time constraints. The results showed that the uncertainty of S-wave velocity is less than ~0.2 km/s in most of the area (Fig. 2.13).

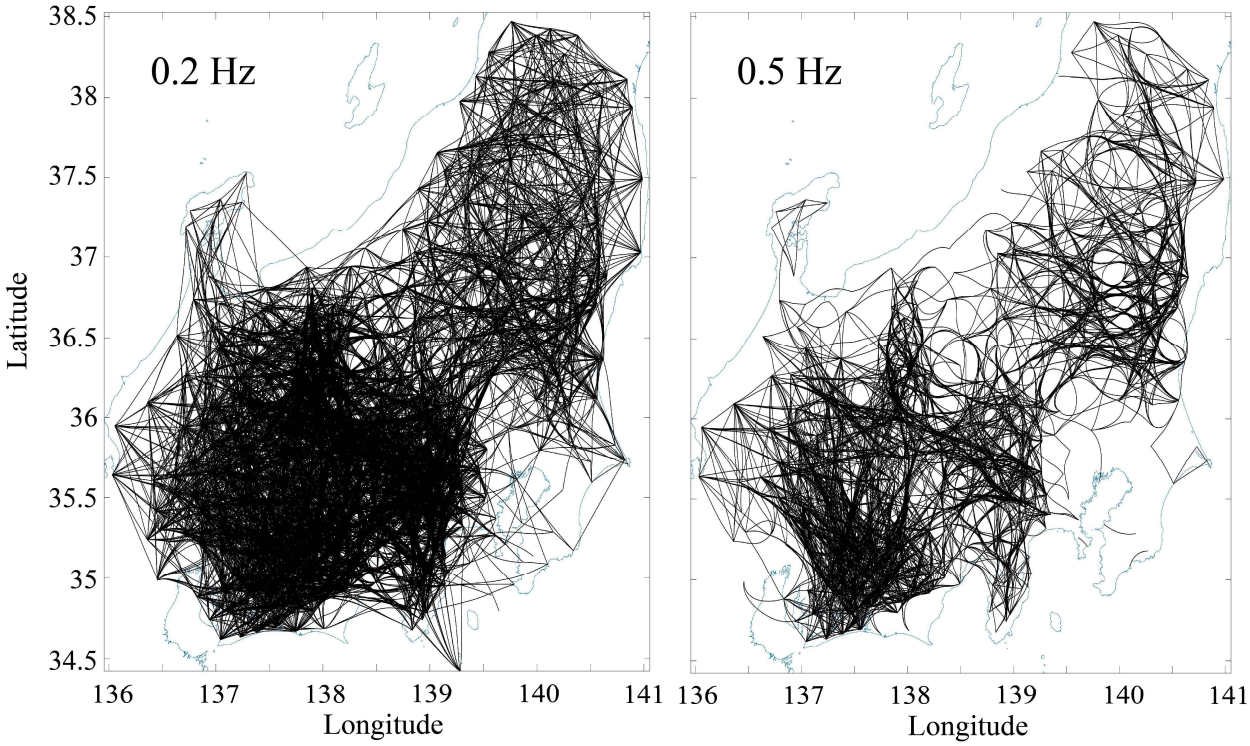

Figure 2.11. *The ray paths obtained from the final three-dimensional model at (a) 0.2 Hz and (b) 0.5 Hz.*

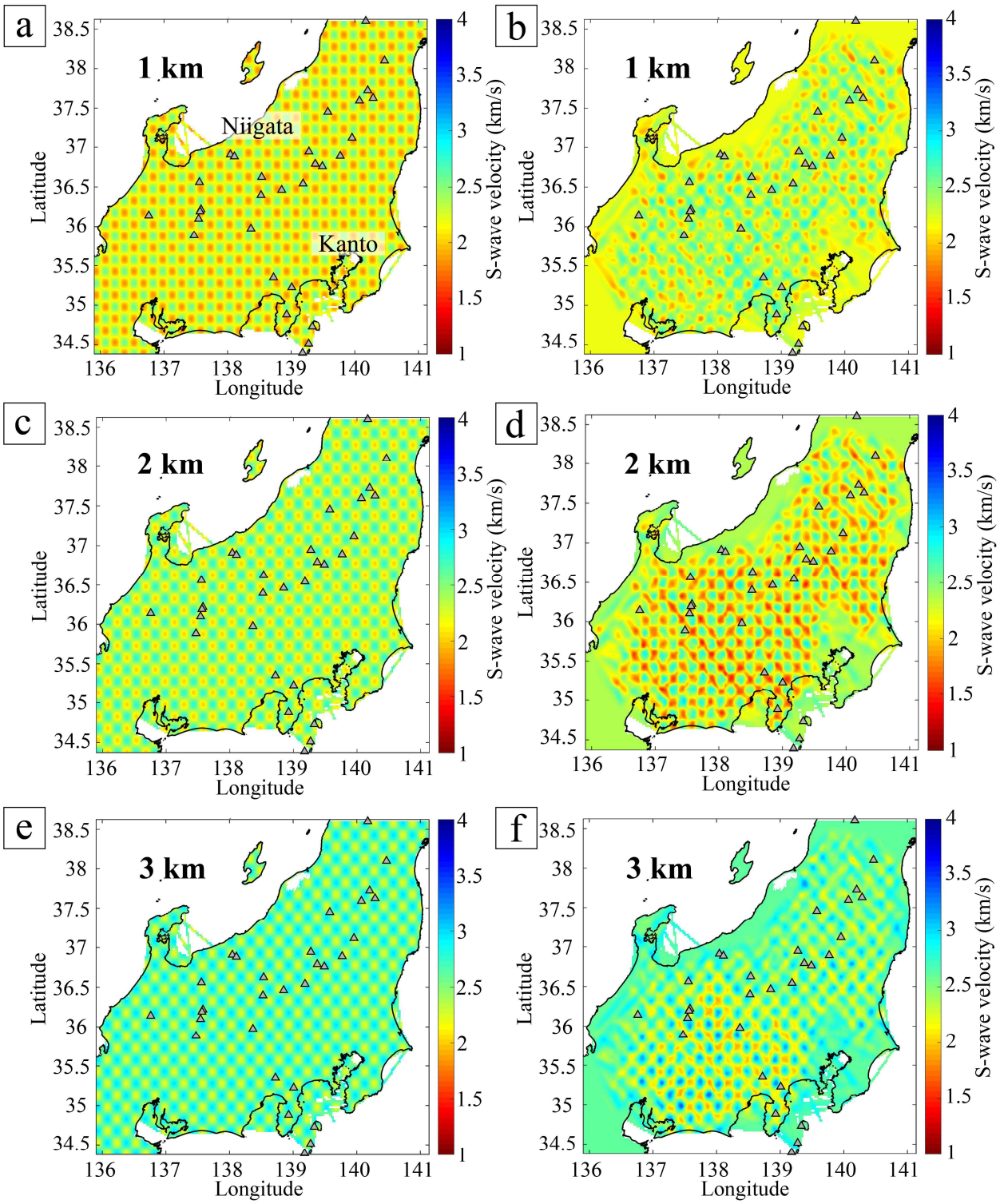

Figure 2.12. *Checkerboard resolution tests of the inversion at different depths (upper left of each panel) without the topographic correction. Panels on the left (a, c, and e) show the input checkerboard model. Panels on the right (b, d, and f) show the recovered checkerboard models. Gray triangles indicate active volcanoes.*

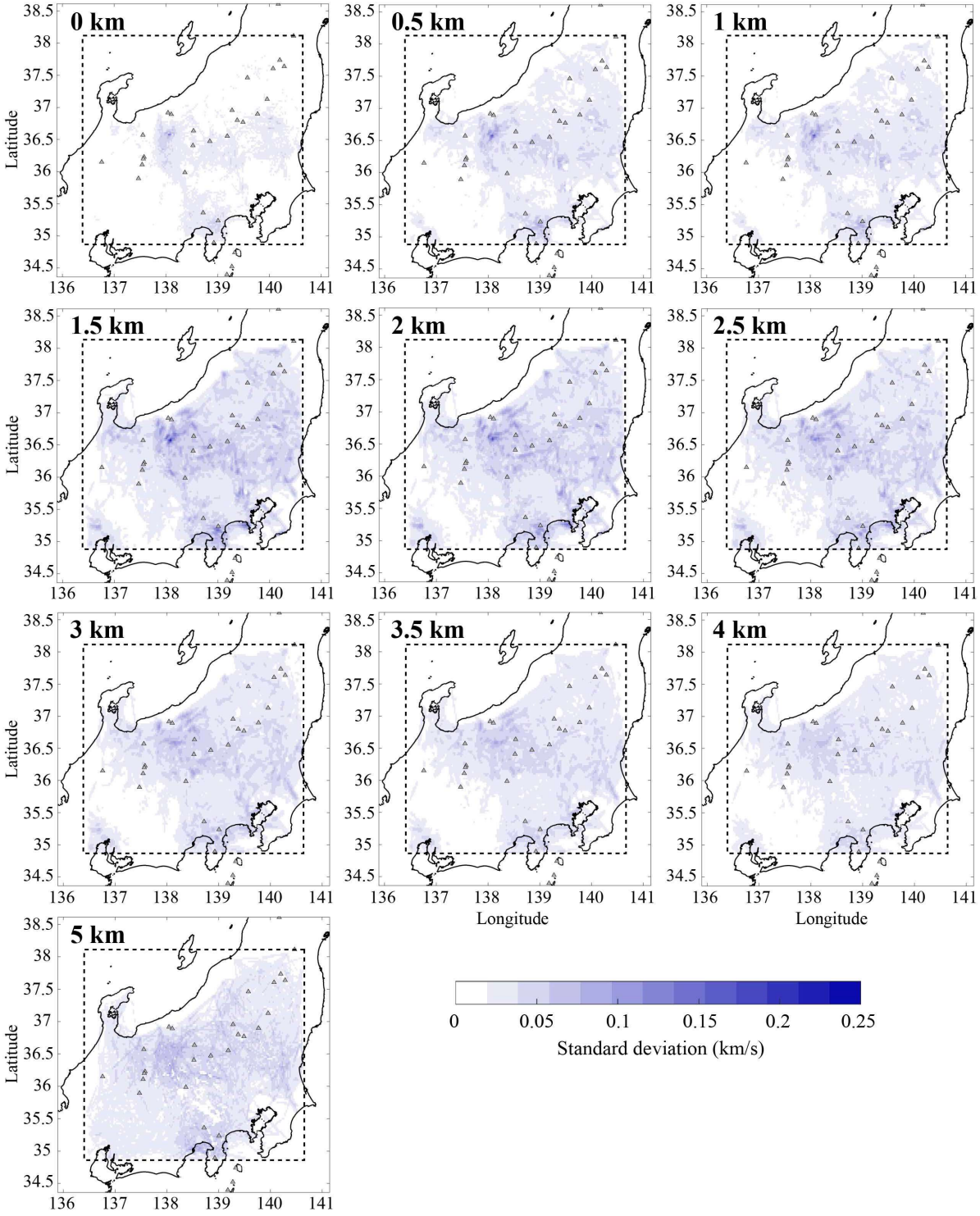

Figure 2.13. *The standard deviation of S-wave velocity at each layer. The black dashed line indicates the estimated area. Gray triangles show active volcanoes.*

2.5. Interpretations

2.5.1 Volcanoes

Mt. Asama is one of the biggest active volcanoes in central Japan (Fig. 2.9), and a low-velocity anomaly beneath it extends to greater depths west of Mt. Asama (red arrows in Fig. 2.14). This low-velocity anomaly is present from ~3 km below sea level. Nagaoka et al. (2012) have observed a similar low S-wave velocity from 5 to 10 km west of the summit using surface wave (0.1–0.4 Hz), and they have suggested that the anomaly represents a magma chamber. The slight difference of the depth of the anomaly could be due to methodological differences and the range of analyzed frequencies. However, the horizontal location and size of the anomaly are consistent. The S-wave velocity of this anomaly is also consistent. In this area, the result of the checkerboard resolution test shows that the inversion models recovered the checkerboard pattern and amplitude well (Fig. 2.12).

Furthermore, below the summit (<2 km), there is a high-velocity anomaly surrounded by low velocities (blue arrow in Fig. 2.14). This high-velocity anomaly could reflect solidified magma resulting from repeated dike intrusions. Such intrusions have been inferred from an active-source seismic experiment (Aoki et al., 2009).

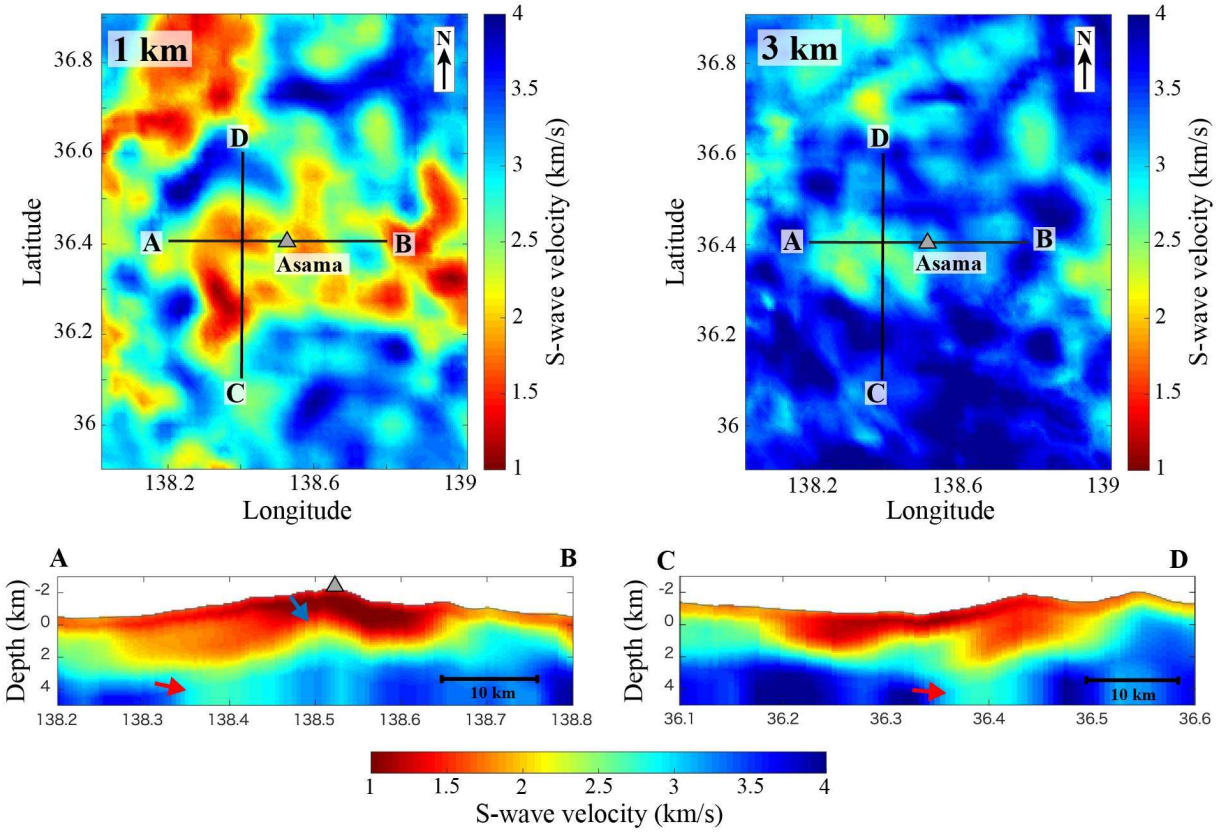

Figure 2.14. *S-wave velocity structure around Mt. Asama. The upper left and right panels represent enlarged views around Mt. Asama (Figure 2.9) at depths 1 and 3 km below sea level. The lower left and right panels are vertical views of the S-wave velocity and profiles A–B and C–D.*

Several active volcanoes are aligned along the volcanic front in the Tohoku region (location in Fig. 2.1). In this area, strong low velocities were apparent around the basins and valleys (Figs. 2.9 and 2.15a). These low velocities reflect the soft sediment in the basins. The low velocities extend to greater depths below some volcanoes, especially Mt. Nikko-Shirane and Mt. Nantai (Figs. 2.15b to 2.15d). In these areas, an anomalous attenuation zone, which has been considered to be a source of magma, was observed in the area east of Mt. Nikko-Shirane. The diameter of this zone is ~10 km at depths greater than 3 km based on the energy ratios of P waves (Horiuchi et al., 1997). Around this attenuation zone, S-wave reflectors have also been detected based on a detailed travel-time analysis of reflected S waves (Matsumoto & Hasegawa, 1996).

Furthermore, the limit of the depth of microearthquakes has been estimated to be much shallower below Mt. Nikko-Shirane than below other areas because the depth of the local magma fluid is shallow (Hasegawa & Matsumoto, 1997). Our results also show a low-velocity zone diameter of ~10 km between Mt. Nikko-Shirane and Mt. Nantai (Figs. 2.15c and d). Because our analysis was highly sensitive to the structure of shallow S-wave velocities, our results revealed that the low-velocity zone continued to nearly the surface (~1 km). This result could reflect a local, shallow magma fluid or a cracking zone due to intrusions of magma fluid.

I thus succeeded in constructing a high-resolution S-wave velocity model in a volcanic area without using active seismic sources. Although I do not present a detailed interpretation of the velocity anomalies in this paper, our result showed local structures that have not been revealed in previous studies over such a wide area.

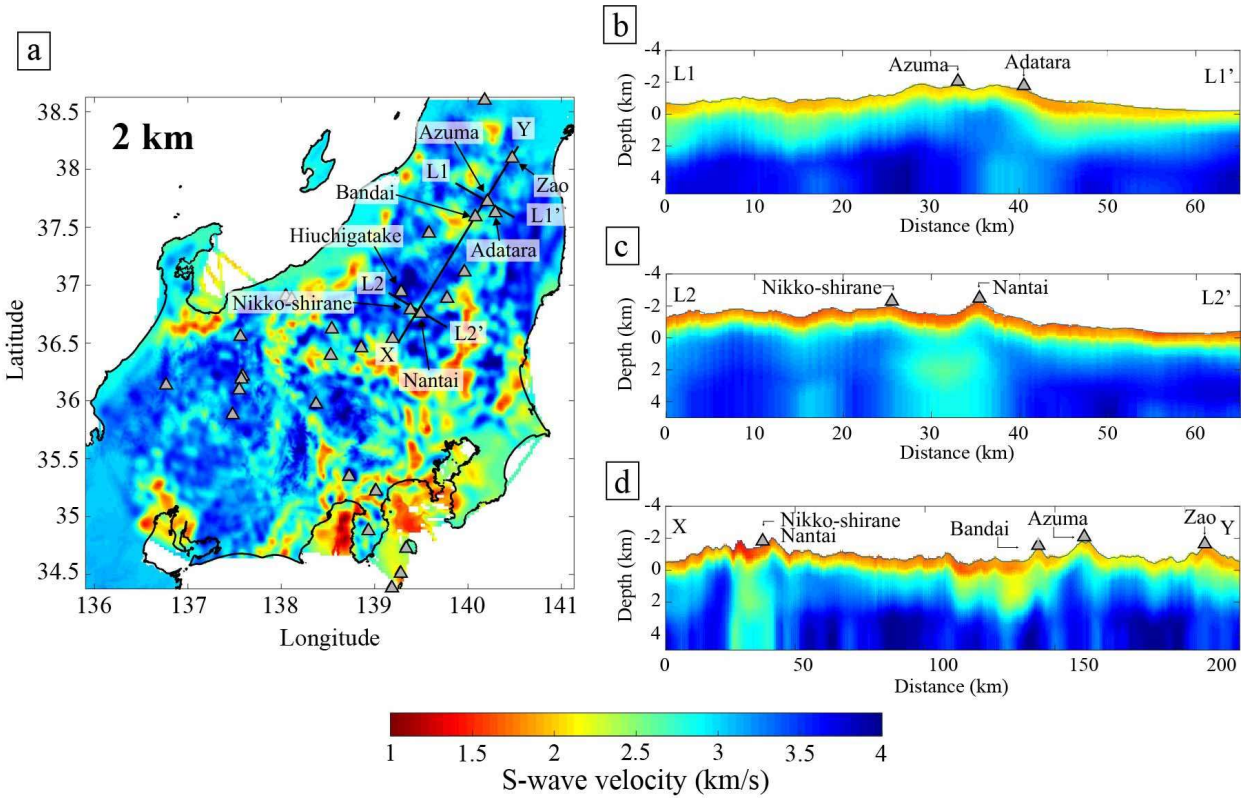

Figure 2.15. *(a) S-wave velocity structure at a depth of 2 km below sea level. (b–d) Vertical views of S-wave velocity along the black lines (L1–L1', L2–L2', and X–Y in the left panel).*

2.5.2 Itoigawa-Shizuoka Tectonic Line

I interpreted low-velocity zones along the ISTL (area (a) in Fig. 2.9) using our S-wave velocity model (Fig. 2.16). The dip directions of local fault segments change from north to south (green line in Fig. 2.16a). Past studies demonstrated that the north segments of the ISTL have mainly east-dipping, low-angle reverse faults (e.g., Okumura, 2001; Panayotopoulos et al., 2014). This trend changes to left-lateral, strike-slip faults in the middle of the ISTL (e.g., Okumura et al., 1994; Panayotopoulos et al., 2014) and to a west-dipping, reverse fault in the south (e.g., Ikeda et al., 2009). These detailed features are apparent in our results—especially the north, east-dipping reverse fault, and the south, west-dipping reverse fault—in the cross-sections of the S-wave velocity (green arrows in Figs. 2.16c and d). Furthermore, the cross-sections of the northern and southern parts of the ISTL (Figures 11c and d) are similar to the seismic reflection profiles reported by Ikami et al. (1986) and Ikeda et al. (2009), respectively. According to the result of the checkerboard resolution test, our S-wave velocity model could accurately reflect the shape of the velocity anomaly with overestimated or underestimated amplitude depending on this area (Fig. 2.12). However, some shapes of the features of the cross-sections along the ISTL (Fig. 2.16) are different from the trends of

previous studies. That can be because our results using long wavelengths (several to ten km) do not show fault planes directly as seismic reflectors on reflection profiles. In our results (i.e., S-wave velocity), I identified the faults based on the velocity contrasts between the hanging wall and footwall.

On the north side of this region, a wide, low-velocity area extends northeast from the ISTL (red arrow in Fig. 2.16b) and reaches depths as great as 4 km (Fig. 2.16e). This low-velocity anomaly lies along the Niigata-Kobe Tectonic Zone, where high strain rates have been revealed by Global Positioning System (GPS) observations (Sagiya et al., 2000). Although previous studies have observed this low-velocity anomaly from the surface to a depth of about 40 km (e.g., Nakajima et al., 2009; Nishida et al., 2008), our results revealed this feature at shallow depths in high spatial resolution.

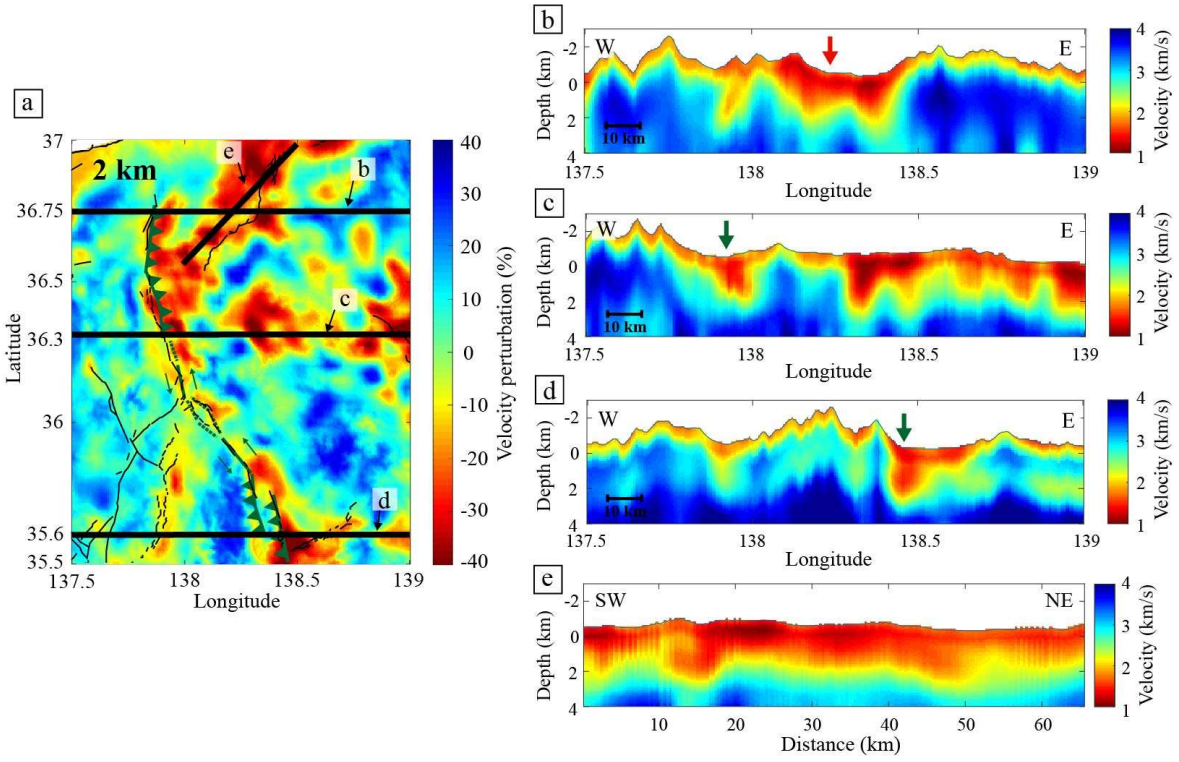

Figure 2.16. *Enlarged view of the area (a) in Figure 2.9. (a) S-wave velocity perturbation at a depth of 2 km below sea level. Green lines indicate the Itoigawa-Shizuoka fault system. Black lines show active faults. (b–e) Vertical views of S-wave velocity along the profiles are marked as thick black lines in (a). Red and green arrows indicate that low-velocity anomalies correspond to the Niigata-Kobe Tectonic Zone and local fault segments.*

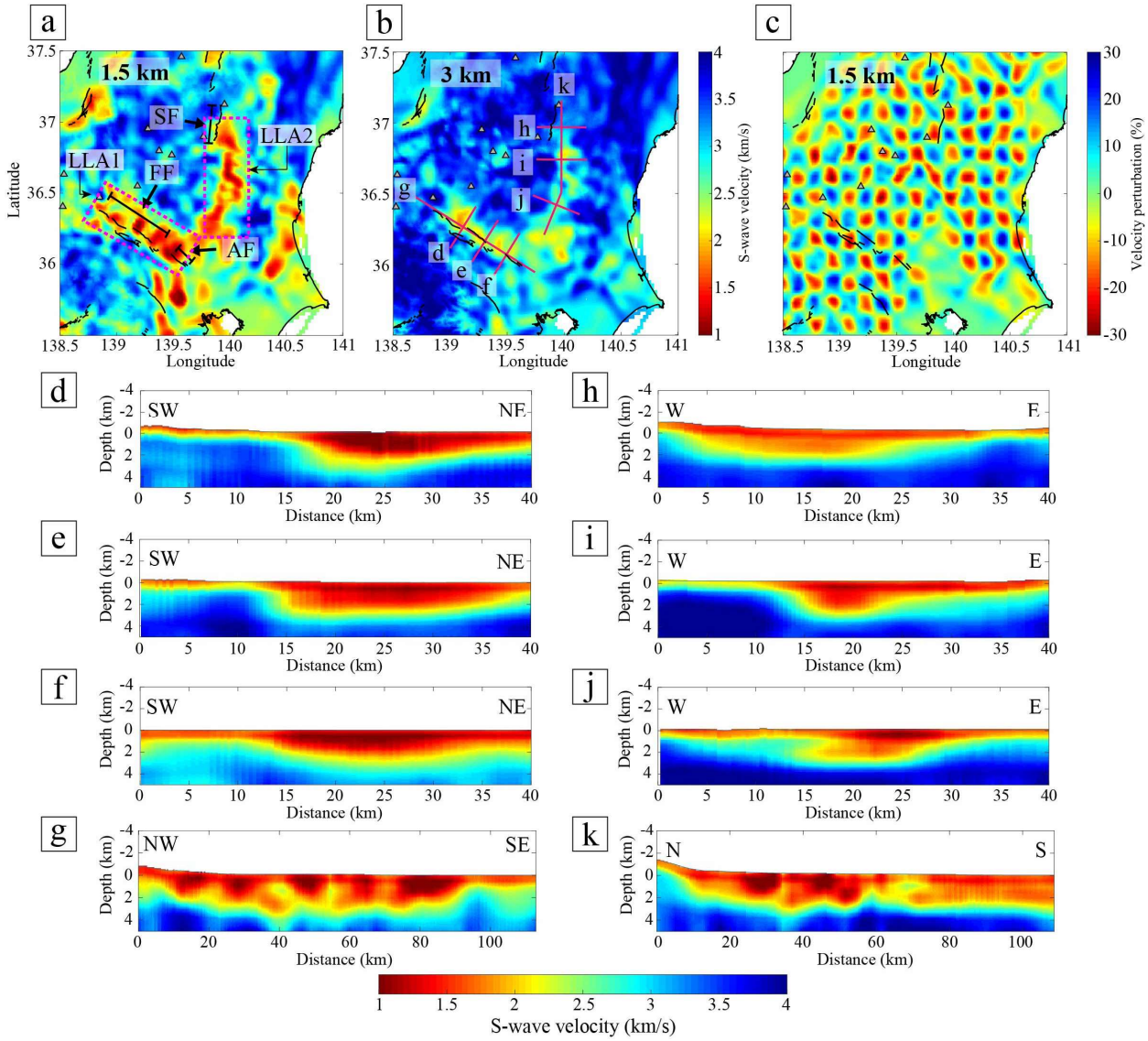

Figure 2.17. *Enlarged velocity model of area (b) in Figure 2.9. (a and b) S-wave velocity at depths of 1.5 and 3 km below sea level. Black lines show active faults. LLA, linear low-velocity anomaly; FF, Fukaya fault system; AF, Ayasegawa fault; SF, Sekiya fault. (c) The recovered checkerboard models at a depth of 1.5 km. (d–k) Vertical cross-sections along the magenta lines in (b).*

2.5.3 Fault Distribution in the Kanto Area

I mapped two linear, low-velocity anomalies around the Kanto region (location in Fig. 2.1). The first of these (LLA1 in Fig. 2.17a) reached a depth >4 km in the Kanto plain and extended northwesterly. It corresponds to the Fukaya fault system and the Ayasegawa fault, southwest-dipping reverse faults (Nakata & Imaizumi, 2002). The depth of the low velocity corresponds to the depth of the upper boundaries of the pre-Neogene system (Suzuki, 2002).

In the cross-sections, some sections show a low-velocity region that tilts in a southwesterly direction (Figs. 2.17d and e). I hypothesized that these tilts reflected the effect of the Fukaya fault system. The cross-section along the Ayasegawa fault showed a weak tilt in a southwesterly direction (Fig. 2.17f). The weakness of this tilt may be a consequence of poor resolution because of the lack of a ray path around Kanto (Figs. 2.11, 2.12 and 2.17c).

The second anomaly (LLA2 in Fig. 2.17a) extended northward and reached a depth no greater than ~4 km (Figs. 2.17d to k). The Sekiya fault, which is a west-dipping reverse fault (Nakata & Imaizumi, 2002) (Fig. 2.17a), is present in the northern part of this anomaly, but our results showed a gentle, low-velocity anomaly without tilt (Fig. 2.17h). In addition, some cross-sections in the middle of this anomaly showed a tilt in a westerly direction (Figs. 2.17i and j). These may reflect old faults under thick sediments or the distribution of basement rock.

2.5.4 Deformation Features Due to the Izu Collision

Many low-velocity anomalies were apparent around the Izu Peninsula (Fig. 2.18). The collision of the Izu-Bonin arc against central Japan because of the subduction of the Philippine Sea plate (Takahashi & Saito, 1997) is considered to be the likely explanation for the complex crustal structure of this region (Arai et al., 2009, 2013). Our results clearly showed low-velocity boundaries related to the Izu collision (Fig. 2.18). In the north-south cross-section of the Izu Peninsula, three or four remarkable low-velocity regions extended from the surface to a depth of about 3 km separating high-velocity blocks, which may represent microplates (or geological blocks), between them (Fig. 2.18c). The Izu Peninsula is subducting beneath the Tanzawa block along the Kannawa fault, a north-dipping reverse fault. This deformation has been clearly observed with active source refraction/reflection data (Arai et al., 2009, 2013). Our results also clearly showed this deformation feature (red arrows in Fig. 2.18c).

Furthermore, our velocity model showed other collisional boundaries probably caused by the Izu collision (Fig. 2.18c). The boundary between the Manazuru block and the north Izu block is the largest and strongest (black arrows in Figs. 2.18c and d). On the other hand, the boundary between the south and north Izu blocks is thin, weak, and characterized by low velocity.

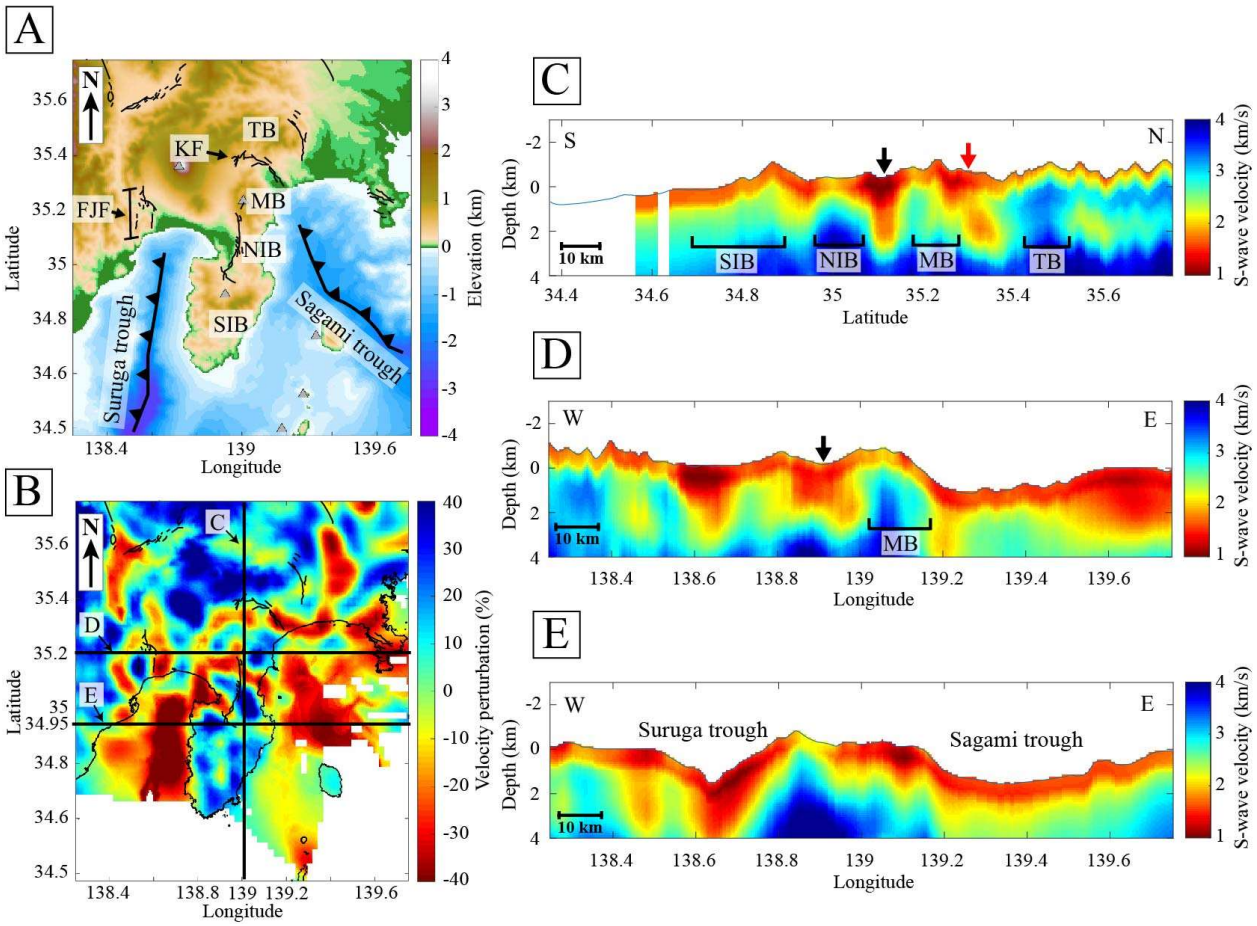

Figure 2.18. *(a) Elevation map around the Izu Peninsula. KF, Kannawa fault; FJF, Fujikawa fault system; TB, Tanzawa block; MB, Manazuru block; NIB, north Izu block; SIB, south Izu block. (b) The S-wave velocity perturbation at 2 km below sea level. (c–e) Vertical cross-sections of S-wave velocity along the black lines in (b).*

Because I used pairs of stations across the ocean, we were able to observe the velocity structure of the coastal area. I could clearly observe low velocities along the plate boundary in the Suruga and Sagami Troughs (Fig. 2.18e). The large low-velocity zone in the Suruga Trough may be due to thick trough sediments and soft sediments related to the Izu collision and active faults.

2.6. Conclusions

I applied surface wave tomography using ambient noise to construct a high-resolution three-dimensional S-wave velocity model in central Japan. I applied the zero-crossing method to estimate surface-wave dispersion curves in the frequency domain, and I obtained a high three-dimensional resolution of shallow structures using a direct inversion

method. The resultant velocity model clearly indicates small-scale geological features such as faults, sedimentary basins, volcanic systems, and geological boundaries. I identified magma-related structures without active-source data in the volcanic regions, and I identified a magma chamber below Mt. Nikko-Shirane based on its low seismic velocity anomaly. Our results also revealed the spatial distribution of fault traces as low-velocity anomalies. In the Izu collision area, I observed several high-velocity blocks separated by low-velocity boundaries, which may represent microplates.

The local geological structures I described here are commonly interpreted using active-source seismic data. However, our higher-resolution surface wave tomography makes such interpretations feasible for large areas. Although I did not present detailed geological interpretations in this study, the velocity model derived from our approach enabled us to independently clarify the relationships between several geologic features considered in previous studies. Furthermore, our high-resolution velocity model can simulate seismic wave propagation to understand the characteristics of amplification in central Japan and thereby contribute to disaster management and assessment.

References

Aki, K., Space and time spectra of stationary stochastic waves, with special reference to microtremors. Bulletin. Earthquake Research Institute, University of Tokyo, 35(3), 415–456 (1957).

Aoki, Y., Takeo, M., Aoyama, H., Fujimatsu, J., Matsumoto, S., Miyamachi, H., et al., P-wave velocity structure beneath Asama Volcano, Japan, inferred from active source seismic experiment. Journal of Volcanology and Geothermal Research, 187(3–4), 272–277. https://doi.org/10.1016/j.jvolgeores.2009.09.004 (2009).

Arai, R., Iwasaki, T., Sato, H., Abe, S., & Hirata, N., Collision and subduction structure of the Izu-Bonin arc, central Japan, revealed by refraction/wide-angle reflection analysis. Tectonophysics, 475(3), 438–453. https://doi.org/10.1016/j.tecto.2009.05.0230 (2009).

Arai, R., Iwasaki, T., Sato, H., Abe, S., & Hirata, N., Crustal structure of the Izu collision zone in central Japan from seismic refraction data. Journal of Geophysical Research: Solid Earth, 118(12), 6258–6268. https://doi.org/10.1002/2013JB010532 (2013).

Bensen, G. D., Ritzwoller, M. H., Barmin, M. P., Levshin, A. L., Lin, F., Moschetti, M. P., et al., Processing seismic ambient noise data to obtain reliable broad-band surface wave

dispersion measurements. Geophysical Journal International, 169(3), 1239–1260. https://doi.org/10.1111/j.1365-246X.2007.03374.x (2007).

Boschi, L., & Ekström, G., New images of the Earth's upper mantle from measurements of surface wave phase velocity anomalies. Journal of Geophysical Research: Solid Earth. https://doi.org/10.1029/2000jb000059 (2002).

Brocher, T. M., Empirical relations between elastic wavespeeds and density in the Earth's crust. Bulletin of the Seismological Society of America, 95(6), 2081–2092. https://doi.org/10.1785/0120050077 (2005).

Chen, K. X., Gung, Y., Kuo, B. Y., & Huang, T. Y., Crustal Magmatism and Deformation Fabrics in Northeast Japan Revealed by Ambient Noise Tomography. Journal of Geophysical Research: Solid Earth, 123(10), 8891–8906. https://doi.org/10.1029/2017JB015209 (2018).

Ekström, G., Time domain analysis of Earth's long-period background seismic radiation. Journal of Geophysical Research, 106(B11), 26483–26493. https://doi.org/10.1029/2000JB000086 (2001).

Ekström, G., Love and Rayleigh phase-velocity maps, 5-40 s, of the western and central USA from USArray data. Earth and Planetary Science Letters, 402(C), 42–49. https://doi.org/10.1016/j.epsl.2013.11.022 (2014).

Ekström, G., Abers, G. A., & Webb, S. C., Determination of surface-wave phase velocities across USArray from noise and Aki's spectral formulation. Geophysical Research Letters, 36(18), 5–9. https://doi.org/10.1029/2009GL039131 (2009).

Fang, H., Yao, H., Zhang, H., Huang, Y. C., & Van Der Hilst, R. D., Direct inversion of surface wave dispersion for three-dimensional shallow crustal structure based on ray tracing: Methodology and application. Geophysical Journal International, 201(3), 1251–1263. https://doi.org/10.1093/gji/ggv080 (2015).

Gu, N., Wang, K., Gao, J., Ding, N., Yao, H., & Zhang, H., Shallow Crustal Structure of the Tanlu Fault Zone Near Chao Lake in Eastern China by Direct Surface Wave Tomography from Local Dense Array Ambient Noise Analysis. Pure and Applied Geophysics, 176(3), 1193–1206. https://doi.org/10.1007/s00024-018-2041-4 (2019).

Hasegawa, A., & Matsumoto, S., Deep Structure of Nikko-Shirane Volcano Group in the Northeastern Japan Arc Estimated from Seismic Observations (in Japanese with English abstract). Bulletin of the Volcanological Society of Japan, 52(Special), S147–S155. https://doi.org/10.18940/kazan.42.Special_S147 (1997).

Horiuchi, S., Tsumura, N., & Hasegawa, A., Mapping of a magma reservoir beneath Nikko-Shirane volcano in northern Kanto, Japan, from travel time and seismogram shape anomalies. Journal of Geophysical Research: Solid Earth, 102(B8), 18071–18090. https://doi.org/10.1029/97jb00974 (1997).

Ikami, A., Yoshii, T., Kubota, S., Sasaki, Y., Hasemi, A., Moriya, T., et al. A seismic-refraction profile in and around Nagano Prefecture, central Japan. Journal of Physics of the Earth, 34(6), 457–474. https://doi.org/10.4294/jpe1952.34.457 (1986).

Ikeda, Y., Iwasaki, T., Kano, K., Ito, T., Sato, H., Tajikara, M., et al., Active nappe with a high slip rate: Seismic and gravity profiling across the southern part of the Itoigawa-Shizuoka Tectonic Line, central Japan. Tectonophysics, 472(1–4), 72–85. https://doi.org/10.1016/j.tecto.2008.04.008 (2009).

Ishiyama, T., Sato, H., Kato, N., Nakayama, T., & Abe, S., Active blind thrusts beneath the Tokyo metropolitan area: Seismic hazards and inversion tectonics. Geophysical Research Letters, 40(11), 2608–2612. https://doi.org/10.1002/grl.50487 (2013).

Kästle, E. D., Soomro, R., Weemstra, C., Boschi, L., & Meier, T., Two-receiver measurements of phase velocity: Cross-validation of ambient-noise and earthquake-based observations. Geophysical Journal International, 207(3), 1493–1512. https://doi.org/10.1093/gji/ggw341 (2016).

Kato, A., Sakai, S., Kurashimo, E., Igarashi, T., Iidaka, T., Hirata, N., et al., Imaging heterogeneous velocity structures and complex aftershock distributions in the source region of the 2007 Niigataken Chuetsu-oki Earthquake by a dense seismic observation. Earth, Planets and Space. https://doi.org/10.1186/BF03353145 (2008).

Lin, F. C., Moschetti, M. P., & Ritzwoller, M. H., Surface wave tomography of the western United States from ambient seismic noise: Rayleigh and Love wave phase velocity maps. Geophysical Journal International, 173(1), 281–298. https://doi.org/10.1111/j.1365-246X.2008.03720.x (2008).

Lobkis, O. I., & Weaver, R. L., On the emergence of the Green's function in the correlations of a diffuse field. The Journal of the Acoustical Society of America, 110(6), 3011–3017. https://doi.org/10.1121/1.1417528 (2001).

Luo, Y., Yang, Y., Xu, Y., Xu, H., Zhao, K., & Wang, K., On the limitations of interstation distances in ambient noise tomography. Geophysical Journal International, 201(2), 652–661. https://doi.org/10.1093/gji/ggv043 (2015).

Matsubara, M., Obara, K., & Kasahara, K., Three-dimensional P- and S-wave velocity structures beneath the Japan Islands obtained by high-density seismic stations by

seismic tomography. Tectonophysics, 454(1–4), 86–103. https://doi.org/10.1016/j.tecto.2008.04.016 (2008).

Matsumoto, S., & Hasegawa, A., Distinct S wave reflector in the midcrust beneath Nikko-Shirane volcano in the northeastern Japan arc. Journal of Geophysical Research: Solid Earth, 101(B2), 3067–3083. https://doi.org/10.1029/95jb02883 (1996).

Nagaoka, Y., Nishida, K., Aoki, Y., Takeo, M., & Ohminato, T., Seismic imaging of magma chamber beneath an active volcano. Earth and Planetary Science Letters, 333, 1–8. https://doi.org/10.1016/j.epsl.2012.03.034 (2012).

Nakajima, J., Hirose, F., & Hasegawa, A., Seismotectonics beneath the Tokyo metropolitan area, Japan: Effect of slab-slab contact and overlap on seismicity. Journal of Geophysical Research: Solid Earth, 114(8), 1–23. https://doi.org/10.1029/2008JB006101 (2009).

Nakata, T., & Imaizumi, T. (Eds)., Digital active fault map of Japan (DVD-ROM) (in Japanese). Tokyo: University of Tokyo Press (2002).

Nishida, K., Kawakatsu, H., & Obara, K., Three-dimensional crustal S wave velocity structure in Japan using microseismic data recorded by Hi-net tiltmeters. Journal of Geophysical Research: Solid Earth, 113(B10302). https://doi.org/10.1029/2007JB005395 (2008).

Obara, K., Kasahara, K., Hori, S., & Okada, Y., A densely distributed high-sensitivity seismograph network in Japan: Hi-net by National Research Institute for Earth Science and Disaster Prevention. Review of Scientific Instruments, 76(2). https://doi.org/10.1063/1.1854197 (2005).

Okada, H., The Microtremor survey method. Geophysical monograph (Vol. 12). Tulsa: Society of Exploration Geophysicists (2003).

Okumura, K., Paleoseismology of the Itoigawa-Shizuoka tectonic line in Central Japan. Journal of Seismology, 5(3), 411–431. https://doi.org/10.1023/A:1011483811145 (2001).

Okumura, K., Shimokawa, K., Yamazaki, H., & Tsukuda, E., Recent Surface Faulting Events along the Middle Section of the Itoigawa-Shizuoka Tectonic Line (in Japanese with English abstract). Zisin, 46(4), 425–438. https://doi.org/10.4294/zisin1948.46.4_425 (1994).

Panayotopoulos, Y., Hirata, N., Sato, H., Kato, A., Imanishi, K., Kuwahara, Y., et al., Investigating the role of the Itoigawa-Shizuoka tectonic line towards the evolution

of the Northern Fossa Magna rift basin. Tectonophysics, 615–616, 12–26. https://doi.org/10.1016/j.tecto.2013.12.014 (2014).

Pilz, M., Parolai, S., Picozzi, M., & Bindi, D., Three-dimensional shear wave velocity imaging by ambient seismic noise tomography. Geophysical Journal International, 189(1), 501–512. https://doi.org/10.1111/j.1365-246X.2011.05340.x (2012).

Rawlinson, N., & Sambridge, M., Wave front evolution in strongly heterogeneous layered media using the fast marching method. Geophysical Journal International, 156(3), 631–647. https://doi.org/10.1111/j.1365-246X.2004.02153.x (2004).

Sagiya, T., Miyazaki, S., & Tada, T., Continuous GPS Array and Present-day Crustal Deformation of Japan. Pure and Applied Geophysics, 157(11–12), 2303–2322. https://doi.org/10.1007/978-3-0348-7695-7_26 (2000).

Satoh, T., Kawase, H., & Matsushima, S., Estimation of S-Wave velocity structures in and around the Sendai Basin, Japan, using array records of microtremors. Bulletin of the Seismological Society of America, 91(2), 206–218. https://doi.org/10.1785/0119990148 (2001).

Seats, K. J., Lawrence, J. F., & Prieto, G. A., Improved ambient noise correlation functions using Welch's method. Geophysical Journal International, 188(2), 513–523. https://doi.org/10.1111/j.1365-246X.2011.05263.x (2012).

Shapiro, N. M., Campillo, M., Stehly, L., & Ritzwoller, M. H., High-resolution surface-wave tomography from ambient seismic noise. Science, 307(5715), 1615–1618. https://doi.org/10.1126/science.1108339 (2005).

Shearer, P. M. (2009). Introduction to seismology. Cambridge: Cambridge University Press.

Snieder, R., Extracting the Green's function from the correlation of coda waves: A derivation based on stationary phase. Physical Review E, 69(4), 046610. https://doi.org/10.1103/PhysRevE.69.046610 (2004).

Suzuki, H., Underground Geological Structure beneath the Kanto Plain, Japan (in Japanese with English abstract). Report of the National Research Institute for Earth Science and Disaster Prevention, 63, 1–19. https://doi.org/http://doi.org/10.24732/nied.00001131 (2002).

Takahashi, M., & Saito, K., Miocene intra-arc bending at an arc-arc collision zone, central Japan. Island Arc, 6(2), 168–182. https://doi.org/10.1111/j.1440-1738.1997.tb00168.x (1997).

Takahashi, M., Tectonic boundary between Northeast and Southwest Japan Arcs during Japan Sea opening (in Japanese with English abstract). Journal of the Geological Society of Japan, 112(1), 14–32. https://doi.org/10.5575/geosoc.112.14 (2006).

Wapenaar, K., & Fokkema, J., Green's function representations for seismic interferometry. Geophysics, 71(4), 1JA-Z75. https://doi.org/10.1190/1.2213955 (2006).

Yang, Y., & Forsyth, D. W., Rayleigh wave phase velocities, small-scale convection, and azimuthal anisotropy beneath southern California. Journal of Geophysical Research: Solid Earth, 111(7), 1–20. https://doi.org/10.1029/2005JB004180 (2006).

Yang, Y., Ritzwoller, M. H., Lin, F., Moschetti, M. P., & Shapiro, N. M., Structure of the crust and uppermost mantle beneath the western United States revealed by ambient noise and earthquake tomography, 113, 1–9. https://doi.org/10.1029/2008JB005833 (2008).

Yao, H., & van der Hilst, R. D., Analysis of ambient noise energy distribution and phase velocity bias in ambient noise tomography, with application to SE Tibet. Geophysical Journal International, 179(2), 1113–1132. https://doi.org/10.1111/j.1365-246X.2009.04329.x (2009).

Yukutake, Y., Honda, R., Harada, M., Arai, R., & Matsubara, M., A magma-hydrothermal system beneath Hakone volcano, central Japan, revealed by highly resolved velocity structures. Journal of Geophysical Research: Solid Earth, 120, 3293– 3308. https://doi.org/10.1002/2014JB011856 (2015).

Chapter 3

Multimodal Rayleigh and Love Wave Joint Inversion for S-wave Velocity Structures in Kanto Basin, Japan

Abstract

The highly populous Kanto Basin, Japan, comprises thick sediments above a complex basement rock and prevention of earthquake disaster is required. The high-resolution three-dimensional S-wave velocity model is essential for understanding the complex amplification of strong ground motion, especially in basins. I constructed a three-dimensional S-wave velocity model for this area using the joint inversion of multimodal dispersion curves of Rayleigh and Love waves. The inclusion of higher modes improved the accuracy and precision of the surface-wave inversion by at least 50%. Our estimated model revealed a low-velocity anomaly of sediments towards the east and a curved velocity contour of the basement rock. Such structures better explain the observed complex surface-wave dispersion curves that were not able to explain in the past homogeneous multilayered model. Our high-precision three-dimensional S-wave velocity model reflects underground heterogeneity and improves the earthquake simulation and hazard assessment.

Keywords: S-wave, Velocity model, Surface-wave inversion, Joint inversion, multimode

3.1. Introduction

Earthquake hazard assessment is vital, especially for densely-populated metropolitan areas like Tokyo, which is located in the earthquake-prone Kanto basin composed of large-scale thick sedimentary formations (Denolle et al., 2018; Koketsu & Kikuchi, 2000; Sato et al., 2005). Constructing an accurate subsurface structure is important for mitigating possible damage from future earthquakes. In this respect, estimating the S-wave velocity structure from the epicenter to the surface is essential for accurately assessing earthquake hazards (Denolle et al., 2014; Kano et al., 2017). Several studies on resource development and disaster prevention have contributed to assessing the subsurface structures of the Kanto region (Koketsu et al., 2009; Komazawa & Hasegawa, 1988; Suzuki, 2002; Viens et al., 2020; Yamanaka & Yamada, 2006). These reveal that the Kanto Basin consists of three sedimentary groups in the basement, with the maximum total thickness of the sediments being >4 km. The strong seismic amplification has strongly affected the shape of the basin (Denolle et al., 2014), and the magnitude of the earthquake varies depending on the direction of incidence. The high-resolution three-dimensional S-wave velocity model is essential to understand the complex amplification of strong ground motion, especially in the Kanto Basin, which comprises thick sediments above a complex basement rock.

S-wave velocity structures can be estimated from the dispersion characteristics of surface waves, which can be constructed using cross-correlation functions of seismic ambient noise. Multimodal surface-wave inversion is an important technique for estimating the accurate S-wave velocity structure over several kilometers in the frequency range below 1Hz. Although the estimation of multimodal dispersion curves of surface waves from ambient noise is difficult, including higher-mode surface-wave dispersion curves to inversion can improve the accuracy and obtain a more reliable S-wave velocity structure (Fu et al., 2022; Luo et al., 2007; Wu et al., 2020; Yamaya et al., 2021). Recently, Wang et al. (2019) developed a frequency-Bessel transform (F-J) method that can effectively extract higher-mode dispersion curves of Rayleigh waves. Hu et al. (2020) extended the F-J method to Rayleigh and Love waves using multicomponent functions. Numerical examples (Wang et al., 2019) and real applications (Hu et al., 2020; Wu et al., 2020; Zhan et al., 2020) have demonstrated that the F-J method is an effective tool for ambient-noise multimodal dispersion curve extraction.

In this study, I estimated the S-wave velocity structure of the Kanto Basin using multimodal dispersion curves of Rayleigh and Love waves. The joint inversion of multimodal Rayleigh and Love waves significantly improved the accuracy and precision of the inverted solutions. The three-dimensional S-wave velocity model derived from the local one-dimensional model revealed the shape and velocity of the sedimentary layer and basement rock.

Our estimated model better explains the observed surface-wave properties that were not able to explain in the major homogeneous multilayered model. Estimating the three-dimensional S-wave velocity structure, including basement rock depth, using only surface waves is also particularly important for comparison and integration with other geophysical survey results, such as gravity surveys commonly used for estimating the basement rock distribution.

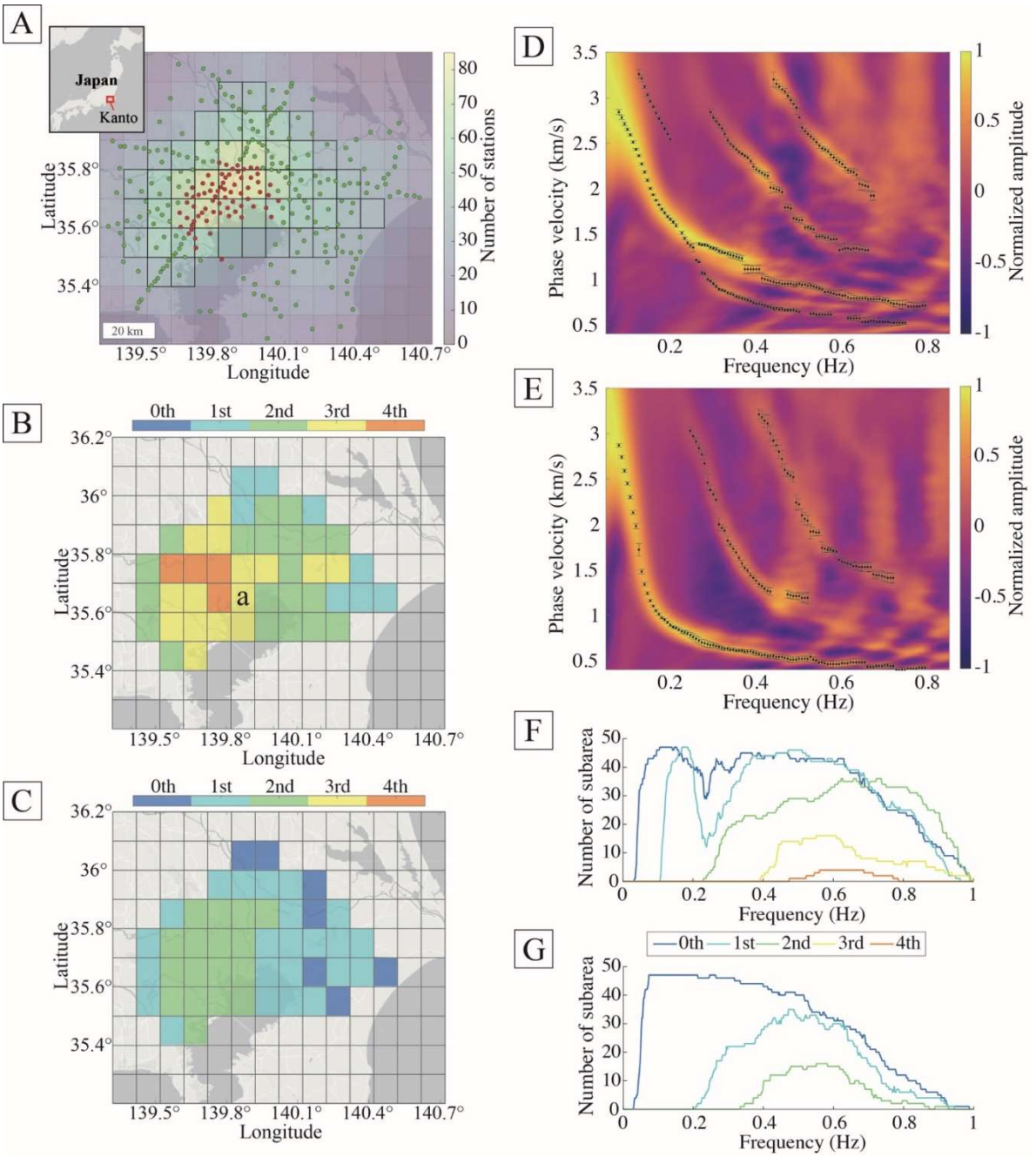

Figure 3.1. *Estimated multimodal surface-wave dispersion curves. (A) Study area and array for the estimation of dispersion curves. Background color indicates the number of stations within 20 km from the center of the grid. Grids having more than 30 stations are indicated by*

a black outline. Green and red dots indicate the MeSO-net stations. Red dots indicate the stations which compose the array of grid 'a' in panel B. (B and C) a Maximum number of modes of estimated dispersion curves of (B) Rayleigh and (C) Love wave. (D and E) Black dots indicate estimated multimodal dispersion curves of (D) Rayleigh and (E) Love wave at grid 'a' in (B). The background color shows the normalized amplitude of F-J spectra. Error bars indicate standard deviation from 1000 bootstrap resampling iterations. (F and G) The number of grids where each mode of phase velocity of (F) Rayleigh and (G) Love wave is observed for each frequency.

3.2. Data and Method

3.2.1 Preprocessing and setting subarray

I downloaded the data observed by the metropolitan seismic observation network (MeSO-net) (National Research Institute for Earth Science and Disaster Resilience, 2021). I downsampled the data from 200 to 66.67 Hz after applying the low-pass filter. The means and trends of the daily three-component data were removed. Single-day data were divided into 10-min segments with 50% overlap. To suppress earthquake signals before cross-correlation, I discarded segments where the mean square amplitude exceeded twice the average of the mean square amplitude (Takagi et al., 2018). For each station pair, the two horizontal components were rotated in the radial and transverse directions according to the distributions of the station pair after correcting for the orientation of each station (KANO et al., 2015). I computed the power-normalized cross spectra for each segment and then stacked them to create annual data. Overall, five components of stacked cross spectra (ZZ, ZR, RZ, RR, and TT) were calculated between all station pairs where the interstation distance was <40 km. After applying the band pass filter of 0.025–0.9 Hz, cross spectra were transformed from frequency domain to time domain. I applied a velocity filter of 0.2–8 km·s-1 in the time domain and transformed it to the frequency domain again. Due to the complexity of the basement rock structure in the Kanto Basin, I divided the study area into subareas to assume a homogeneous multilayered structure. For each subarea, I estimated the dispersion curves using data recorded at stations located within 20 km from its center. Subareas having fewer than 30 stations were excluded from analysis, due to instability in the F-J spectrogram (Fig. 3.1A).

3.2.2 Estimation of dispersion curves

To estimate the multimodal dispersion curves of Rayleigh and Love waves, I applied the frequency-Bessel transform (F-J) method (Wang et al., 2019). Hu et al. (2020) extended the F-J spectrogram of the ZZ components to multi-components, enabling the estimation of

multimode dispersion curves. That showed strong sensitivity only at dispersion points via the Dirac delta function.

I estimated the multimodal dispersion curves from the amplitude peaks of the F-J spectrogram. Estimation of multimodal dispersion curves in the basin requires careful consideration as osculation (smooth connection of the fundamental mode and first overtone) occurs in the basin because of the strong velocity contrast between the sediments and basement rock (Boaga et al., 2013). In the Kanto basin, Boue et al. (2016) reported the osculation point to be ~0.21 Hz using the nine components average correlation tensor for the MeSO-net stations. Above 0.21 Hz, the Rayleigh wave fundamental mode dominates the ZZ component, and the first higher mode dominates the RR component (Boúe et al., 2016). The situation reverses for frequencies lower than 0.21 Hz, where the fundamental mode dominates the RR component, and the first higher mode dominates the ZZ component.

In this study, I used different F-J spectrograms (I_{R0}, I_{R1}, I_{R2} and I_{sum}) to estimate the dispersion curves based on frequency. I selected the phase velocity of the fundamental mode from I_{R2} below ~0.21 Hz and from I_{R0} above ~0.2 Hz, and phase velocity of the first overtone from I_{R0} below ~0.21 Hz and I_{R2} above ~0.2 Hz; phase velocity of second or higher mode were selected from I_{R2}. I also examined other spectrograms and selected them as appropriate. The dispersion curves estimated from respective F-J spectrograms were similar in all instances where clear amplitude peaks corresponding to each mode were observed in the F-J spectrograms.

Phase velocity picking was performed semi-automatically. Specifically, the range of phase velocities and frequencies to be selected for each mode was manually specified, and the phase velocity with the largest amplitude within that range was obtained for each frequency. The dispersion curves were selected for the Love and Rayleigh waves. The F-J spectrogram was not selected for the Love wave, considering that there was only I_{L0}.

I estimated the variance of each phase velocity using bootstrap resampling (Efron & Tibshirani, 1994; Löer et al., 2018). The F-J spectrogram was estimated from the same number of stations that were randomly selected from stations in the same subarea, allowing duplication. Since the resampled F-J spectrogram was similar to returning the same peaks as the original F-J spectrogram, the phase velocity closest to the original F-J spectrogram was estimated. Resampling was conducted 1000 times, and the error of each dispersion curve was estimated from the variance of the resampled phase velocities (Löer et al., 2018) (Fig. 3.1D, E).

3.2.3 F-J spectra

The F-J spectrogram can be derived by applying the Hankel transform (Erdélyi et al., 1954), the orthogonal property of the Bessel function (Arfken et al., 2005) and the spatial

autocorrelation (SPAC) method (Aki, 1957). In this study, I skipped the details of the derivation of the F-J spectrogram, which are shown in Wang et al. (2019) and Hu et al. (2020). The F-J spectrogram can be expressed as the following:

$$I_{R0}(f,c) \approx \int_0^\infty CC_{ZZ}(f,r) J_0\left(\frac{2\pi f}{c} r\right) r dr, \tag{3.1}$$

$$I_{R0}(f,c) = P^R(f) \frac{c}{(2\pi f)^2} \delta(c_R - c), \tag{3.2}$$

where I_{R0} is the F-J spectrogram of the Rayleigh wave derived from the ZZ-component cross spectra CC_{ZZ}, J_0 is the Bessel function of the first kind of order zero, δ is the Dirac delta function, f is the frequency, c is the phase velocity, c_R is the Rayleigh wave phase velocity, and P^R is the Rayleigh wave power spectrum.

Hu et al. (2020) extended the F-J method from the ZZ component to all multicomponent using the SPAC coefficient tensor for Rayleigh and Love waves (Haney et al., 2012). A noteworthy point of the extended F-J method is the separation of Rayleigh and Love waves in the RR- and TT-component cross spectra. In most cases using TT-component cross spectra, I assumed that the contribution of the Love wave was dominant and ignored the contribution of the Rayleigh wave. Furthermore, it was difficult to use the RR-component cross spectra because of the unknown contributions of Rayleigh and Love waves. The extended F-J method could theoretically overcome these problems. In this study, I expressed the multicomponent F-J spectrogram (the details of the derivation are provided in Hu et al. 2020). The F-J spectrogram derived from the multicomponent cross spectra can be expressed as follows:

$$I_{R1}(f,c) \approx \int_0^\infty \{CC_{RZ}(f,r) - CC_{ZR}(f,r)\} J_1\left(\frac{2\pi f}{c} r\right) r dr, \tag{3.3}$$

$$I_{R2}(f,c) \approx \int_0^\infty \{CC_{RR}(f,r) + CC_{TT}(f,r)\} J_0\left(\frac{2\pi f}{c} r\right) r dr - \int_0^\infty \{CC_{RR}(f,r) - CC_{TT}(f,r)\} J_2\left(\frac{2\pi}{c} r\right) r dr, \tag{3.4}$$

$$I_{L0}(f,c) \approx \int_0^\infty \{CC_{RR}(f,r) + CC_{TT}(f,r)\} J_0\left(\frac{2\pi f}{c} r\right) r dr + \int_0^\infty \{CC_{RR}(f,r) - CC_{TT}(f,r)\} J_2\left(\frac{2\pi f}{c} r\right) r dr, \quad (3.5)$$

where I_{R1} is the F-J spectrogram of the Rayleigh wave derived from the ZR- and RZ-component cross spectra CC_{ZR} and CC_{RZ}, J_1 and J_2 are the Bessel functions of the first kind of 1st and 2nd order; and are the F-J spectrograms of Rayleigh and Love waves derived from the RR- and TT-component cross spectra CC_{RR} and CC_{TT}. By using the multicomponent SPAC coefficient (Haney et al., 2012), Equations 3.3 to 3.5 can be expressed as follows (Hu et al., 2020):

$$I_{R1}(f,c) = \frac{1}{\varepsilon(f)} P^R(f) \frac{2c}{(2\pi f)^2} \delta(c_R - c), \quad (3.6)$$

$$I_{R2}(f,c) = \frac{1}{\varepsilon^2(f)} P^R(f) \frac{2c}{(2\pi f)^2} \delta(c_R - c), \quad (3.7)$$

$$I_{L0}(f,c) = P^L(f) \frac{2c}{(2\pi f)^2} \delta(c_L - c), \quad (3.8)$$

where ε is the period-dependent vertical-to-horizontal amplitude ratio, or ZH ratio, which is equal to the inverse of the horizontal-to-vertical amplitude ratio, P^L is the Love wave power spectrum, c_L is the Love-wave phase velocity.

To calculate each F-J spectrogram (Equations 3.3–3.5), I used the following discrete summation proposed by Hu et al. (2020) by assuming that there are N cross spectra arranged according to the interstation distances in ascending order ($r_1, r_2, \ldots, r_N$):

$$\int_0^\infty G(r) J_n\left(\frac{2\pi f}{c} r\right) r dr \approx \sum_{j=1}^{N} \left[\frac{G(r_j)}{8}\left(r_{j+1}^2 + 2r_j\left(r_{j+1} - r_{j-1}\right) - r_{j-1}^2\right) J_n\left(\frac{2\pi f}{c} r_j\right)\right], \quad (3.9)$$

where $r_0 = 0$, $r_{N+1} = r_N$, and $G(r)$ is the kernel function, J_n is the Bessel function of the first kind of nth order. Finally, I can estimate the Rayleigh and Love wave multi-mode dispersion curves from the largest absolute amplitude of each F-J spectrogram at each frequency.

In the F-J method, Rayleigh wave dispersion curves can be estimated from three F-J spectrograms (I_{R0}, I_{R1} and I_{R2}). Hu et al. (2020) proposed an additional F-J spectrogram by summation ($I_{sum} = I_{R0} + |I_{R1}| + I_{R2}$) and multiplication ($I_{mul} = \sqrt[3]{I_{R0} \cdot I_{R1} \cdot I_{R2}}$) approaches to enhance the Rayleigh wave F-J spectrogram. Because the power spectrum and ellipticity vary with mode, depending on the type of Rayleigh wave F-J spectrogram (I_{R0}, I_{R1} and I_{R2}), a particular mode can be dominant at a particular frequency.

3.2.4 Inversion problem

I estimated an optimum S-wave velocity using the objective function Φ, which minimizes the difference between the observed and theoretical phase velocities of the multimodal Rayleigh and Love waves.

$$\Phi = \sum_{i=0}^{NR-1}\left(\sqrt{\frac{\sum W_{R,i}\left(C_{R,i}^{obs}(f) - C_{R,i}^{theo}\left(f, V_s^{(n)}, H^{(n)}\right)\right)^2}{NF_{R,i}}}\right) + \sum_{i=0}^{NL-1}\left(\sqrt{\frac{\sum W_{L,i}\left(C_{L,i}^{obs}(f) - C_{L,i}^{theo}\left(f, V_s^{(n)}, H^{(n)}\right)\right)^2}{NF_{L,i}}}\right), \quad (3.10)$$

where NR and NL are the number of observed modes of the Rayleigh and Love waves, respectively. NF indicates the number of frequencies observed in the ith mode of the Rayleigh or Love waves (represented by the subscript R or L). W indicates weight. $C^{obs}(f)$ and $C^{theo}(f)$ indicate the observed and theoretical phase velocities at frequency f. $V_s^{(n)}$ and $H^{(n)}$ indicate the S-wave velocity and thickness of nth layer, respectively, as variables to be estimated. The theoretical phase velocities were estimated using a computer program in seismology (Herrmann, 2013).

The Kanto Basin consists of three sedimentary layers in its basement (Koketsu et al., 2009; Suzuki, 2002; Yamanaka & Yamada, 2006). Based on previous studies, I assumed four layers. The S- and P-wave velocities of each layer were reported in previous studies. Based on Kokestu et al. (2009) and Yamanaka & Yamada (2002), I used the S-wave velocities of 0.5 km·s^{-1}, 1.0 km·s^{-1}, 1.7 km·s^{-1}, and 3.2 km·s^{-1} as initial values in the Shimousa (first layer),

Kazusa (second layer), Miura (third layer), and pre-Neogene layers (fourth layer), respectively. The P-wave velocities V_p and densities ρ were fixed using different empirical relationships for sediments (Kitsunezaki et al., 1990; Yamanaka et al., 1994) and basement rock (Koketsu et al., 2009):

$$V_p = \begin{cases} 1.11V_s + 1.290 & (sediments) \\ 1.0753V_s + 2.1183 & (basementrock) \end{cases}, \qquad \rho = \begin{cases} -0.536ln\left({V_p}^{-1}\right) + 1.635 & (sediments) \\ -6.737{V_p}^{-1} + 3.808 & (basementrock) \end{cases}. \tag{3.11}$$

The optimal S-wave velocities were found to be in the range of ±20% of the initial S-wave velocities in sediments and ±10% in the basement rock. The optimal thicknesses were determined to be 0–1 km in the first layer and 0–2 km in the second and third layers. If the estimated thickness was < 30 m, it was considered as zero.

I inverted the multimode surface-wave dispersion curves using forward modeling to estimate the S-wave velocity structure. To find the global minimum, I applied the CMA-ES (Hansen & Ostermeier, 2001; Hansen, 2016) because deterministic derivative-based methods typically depend on the initial model and easily converge to a local minimum. CMA-ES aims to explore the model space globally, robust to ill-conditioned problems (Hansen & Ostermeier, 2001; Hansen, 2016). The CMA-ES algorithm can reflect the results of each generation and adaptively increase or decrease the search space for the next generation. Although there is less application of CMA-ES in geophysics (Grayver & Kuvshinov, 2016; Munch et al., 2018), it has been implemented as a global minimization method that outperforms other optimization methods such as genetic algorithms.

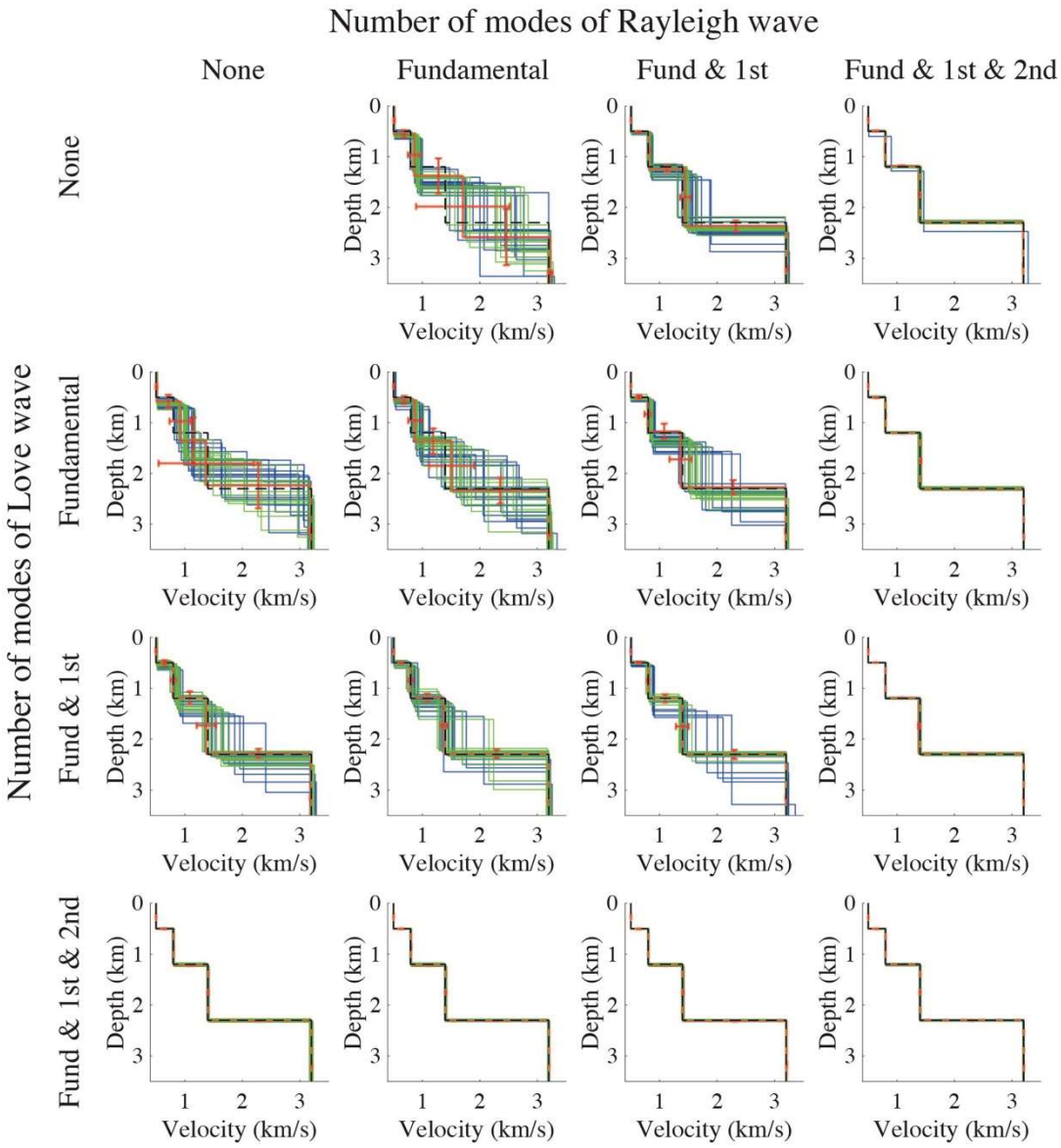

Figure 3.2. *Simulation test of inversion using multimodal surface-wave dispersion curves. Each column and row indicate the number of included modes of Rayleigh and Love wave. The black dashed line indicates the true model. Green and blue lines show the solutions of 30 times inversions using the initial model with 0−10% and 15−25% variations, respectively. The red line indicates the best solution. The error bar shows the standard deviation of the first 10 solutions with minimum misfits from the true model.*

3.2.5 Simulation test

I applied inversion to synthetic data. The synthetic model was adjusted to simulate actual data by following the inversion results (grid ‘a’ in Fig. 3.1B; Table 3.1). The available frequency range of the dispersion curves was also adjusted to represent the actual observed

multimodal dispersion curves (grid ‘a’ in Fig. 3.1B; Fig. 3.1D, C). The error tolerance in each phase velocity was set at 5%. Inversion was applied 30 times on the initial model, which was randomly generated by adding 0−10% and 15−25% variations to the true model (green and blue lines, respectively, in Fig. 3.2).

Table 3.1. Simulation model for the synthetic inversion test.

	Thickness (km)	S-wave velocity (km·s^{-1})
1st layer	0.5	0.5
2nd layer	0.7	0.8
3rd layer	1.1	1.4
4th layer		3.2

3.3. Results

I obtained four types of F-J spectrograms using multicomponent cross-correlations of the ambient noise records of the MeSO-net (Figs. 3.1A and 3.3), and estimated the multimodal dispersion curves of Rayleigh and Love waves from the peaks of the F-J spectrograms (Fig. 3.1B–G). I estimated the second and first overtones of the Rayleigh and Love waves, respectively, for most grids where the number of stations of the array exceeded 30 (Fig. 3.1A–C). The highest numbers of observed mode of the Rayleigh and Love waves were fourth and second modes, respectively.

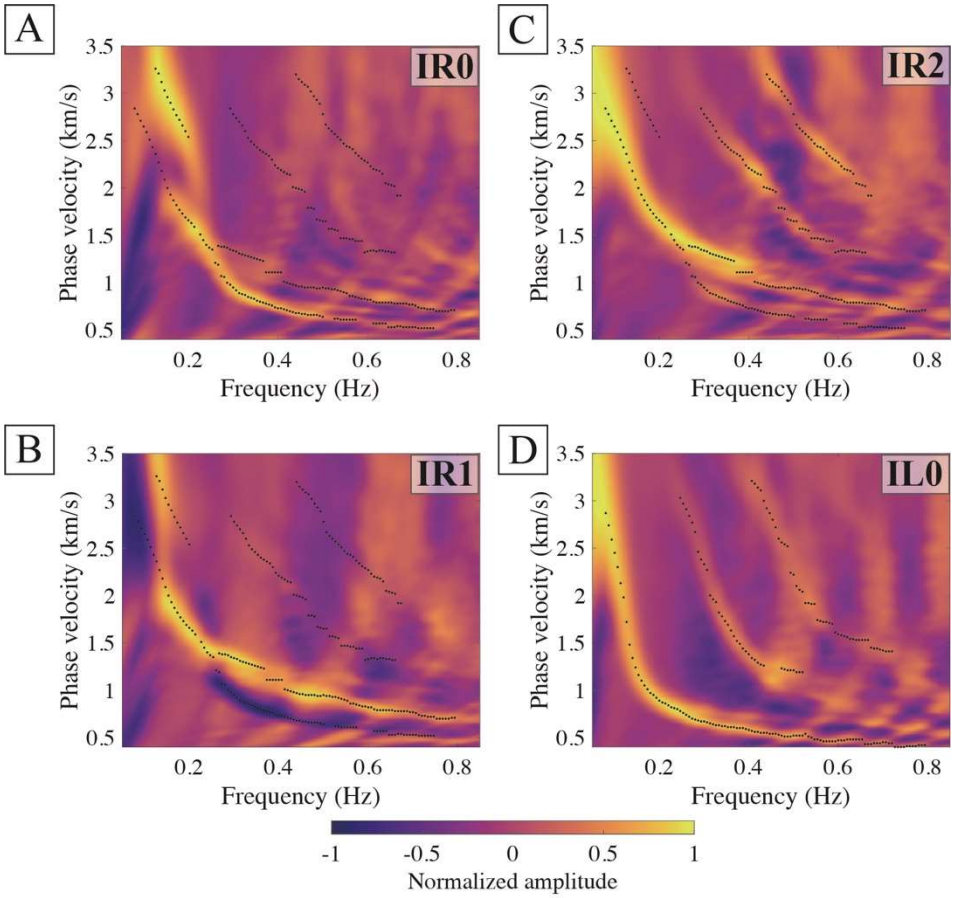

Figure 3.3. *F-J spectrograms in grid 'a' in Fig. 3.1B. (A–D) The F-J spectrograms estimated by using (A) eq. 3.2, (B) eq. 3.3, (C) eq. 3.4, and (D) eq. 3.5, respectively. The background color shows the normalized amplitude of F-J spectrograms. Black dots indicate the estimated multimodal phase velocities of (A–C) Rayleigh and (D) Love waves.*

I constructed a four-layered velocity model following previous studies (Koketsu et al., 2009; Suzuki, 2002; Yamanaka & Yamada, 2006). The number of parameters to be estimated is seven; the S-wave velocity of each layer and its thickness. For surface-wave inversion, I applied the covariance matrix adaptation evolution strategy (CMA-ES) (Hansen & Ostermeier, 2001; Hansen, 2016) using a forward modeling approach that compares the theoretical dispersion curves of estimated models and the observed surface-wave dispersion curves.

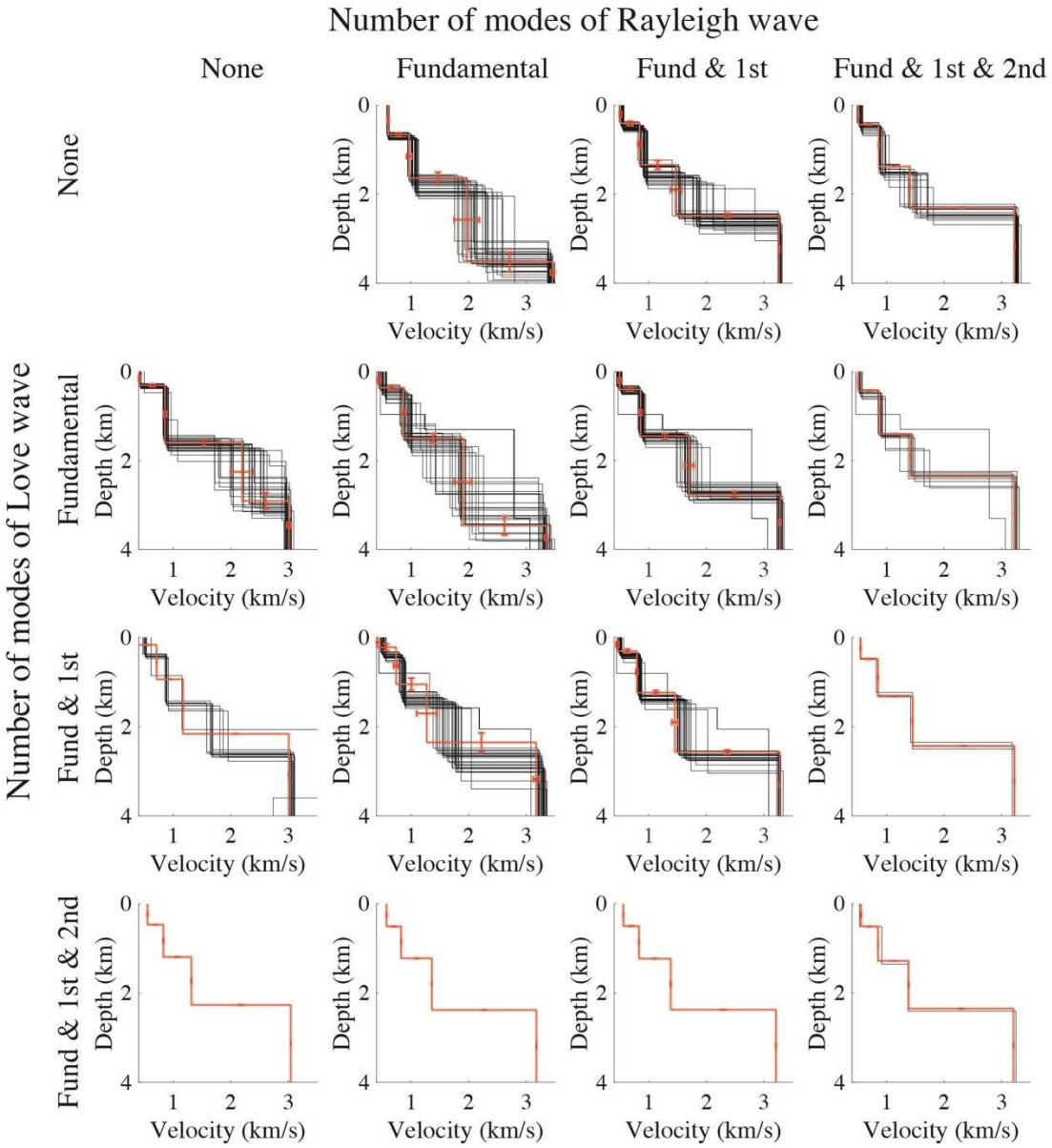

Figure 3.4. *Inversion results for grid 'a' in Fig. 3.1B using multimodal surface-wave dispersion curves. Each column and row indicate the number of included modes of Rayleigh and Love wave. Black lines indicate solutions of 30 times inversions with a randomly perturbated initial value. The red line indicates the best solution. The error bar shows the standard deviation of the first 10 solutions with minimum misfits.*

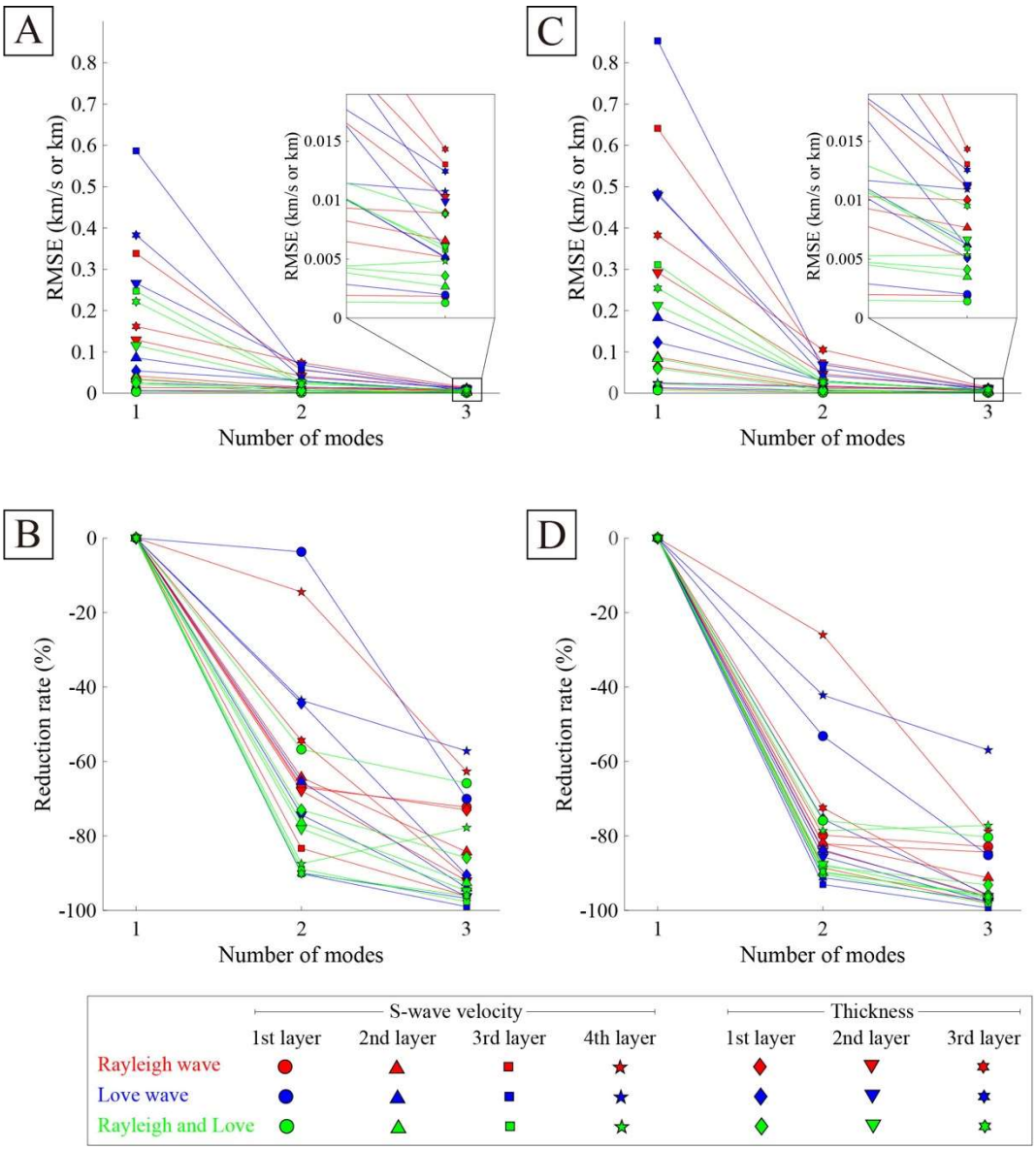

Figure 3.5. *The standard deviation of solutions in the simulation test. (A–D) (A) Standard deviations of the first 10 solutions with minimum misfit from its average. The legend is summarized at the bottom. (B) The reduction rate of (A). The result of the fundamental mode is used as the reference for other results. (C–D) Same as (A–B), but standard deviations from the true model.*

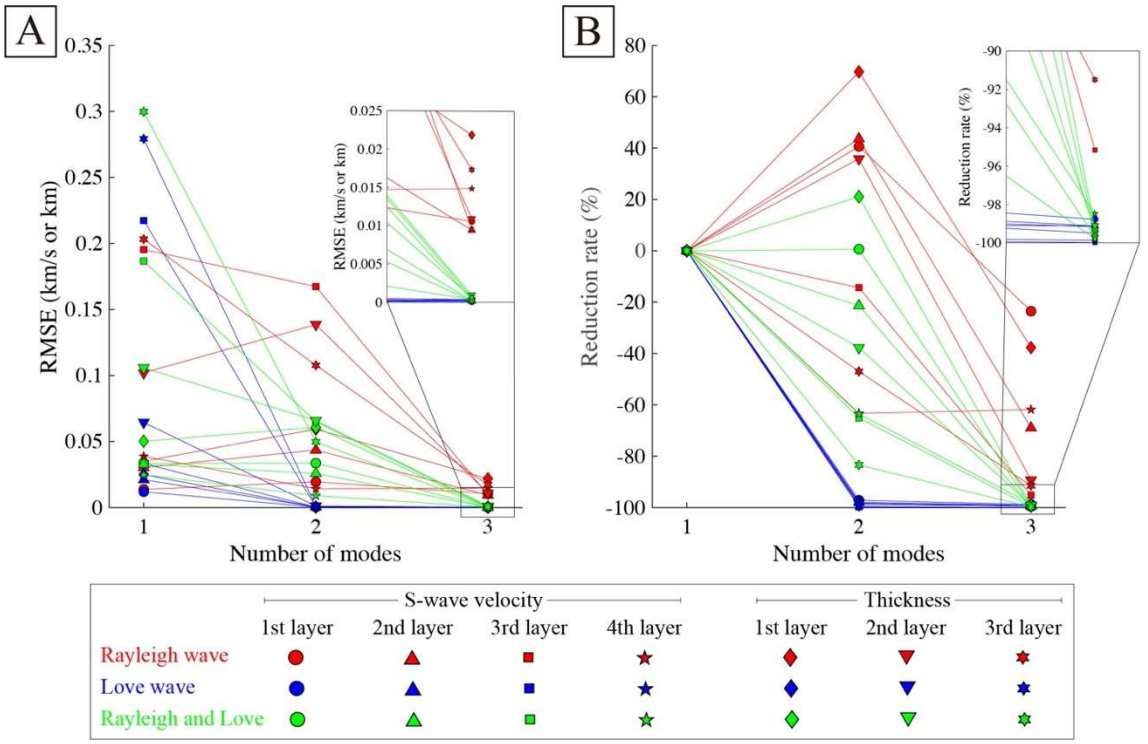

Figure 3.6. *The standard deviation of solutions in the inversion test using actual data. (A–B) (A) Standard deviations of the first 10 solutions with minimum misfit from its average. The legend is summarized at the bottom. (B) The reduction rate of (A). The result of the fundamental mode is used as the reference for other results.*

First, I applied inversion to synthetic data to validate the performance of the multimodal dispersion curves (Fig. 3.2). Furthermore, I validated the performance of multimodal dispersion curves using actually observed dispersion curves (grid 'a' in Fig. 3.1B; Fig. 3.4). Both inversions of synthetic and actual data show better convergence by including higher modes. Comparing inversion using only fundamental mode and fundamental to second higher mode, the standard deviations of the first 10 solutions with minimum misfit from an average and true model decrease by more than 50% (Fig. 3.5). Furthermore, in the case of actual data, the standard deviations of the first 10 solutions with minimum misfit decrease by about 98% by the inclusion of first and second overtones (Fig. 3.6).

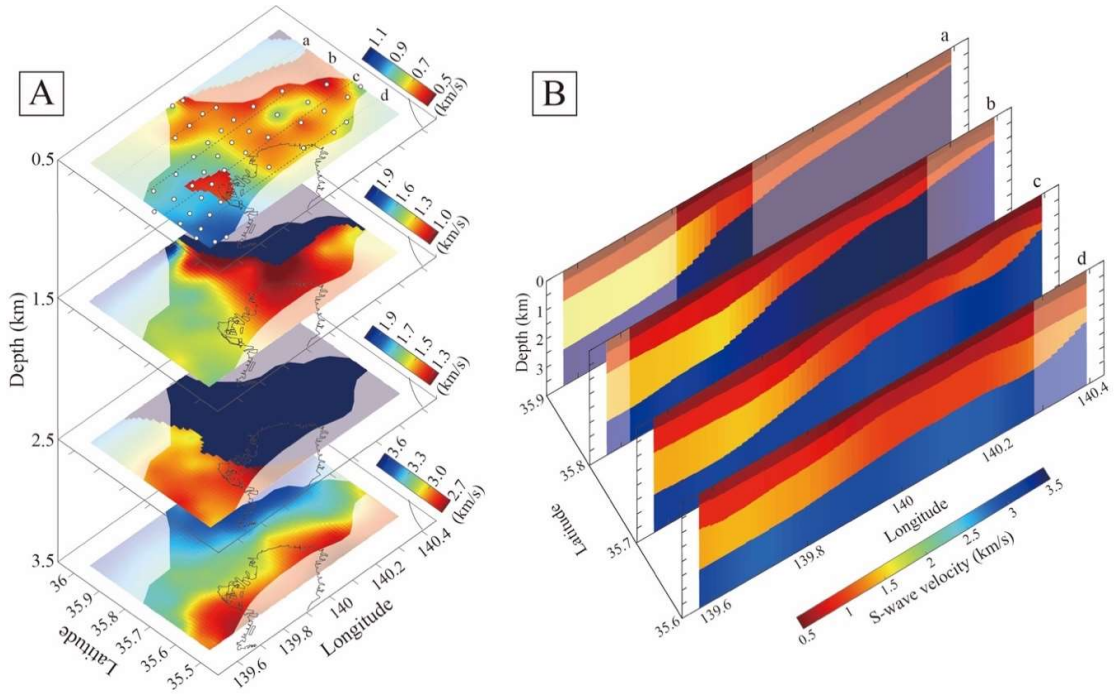

Figure 3.7. *Horizontal and vertical slices of estimated the three-dimensional S-wave velocity model. (A) Horizontal slices. The white dots indicate the center of stations in each grid. The extrapolated area is masked. (B) Vertical slices along with the dashed lines a−d in (A). The extrapolated area is masked.*

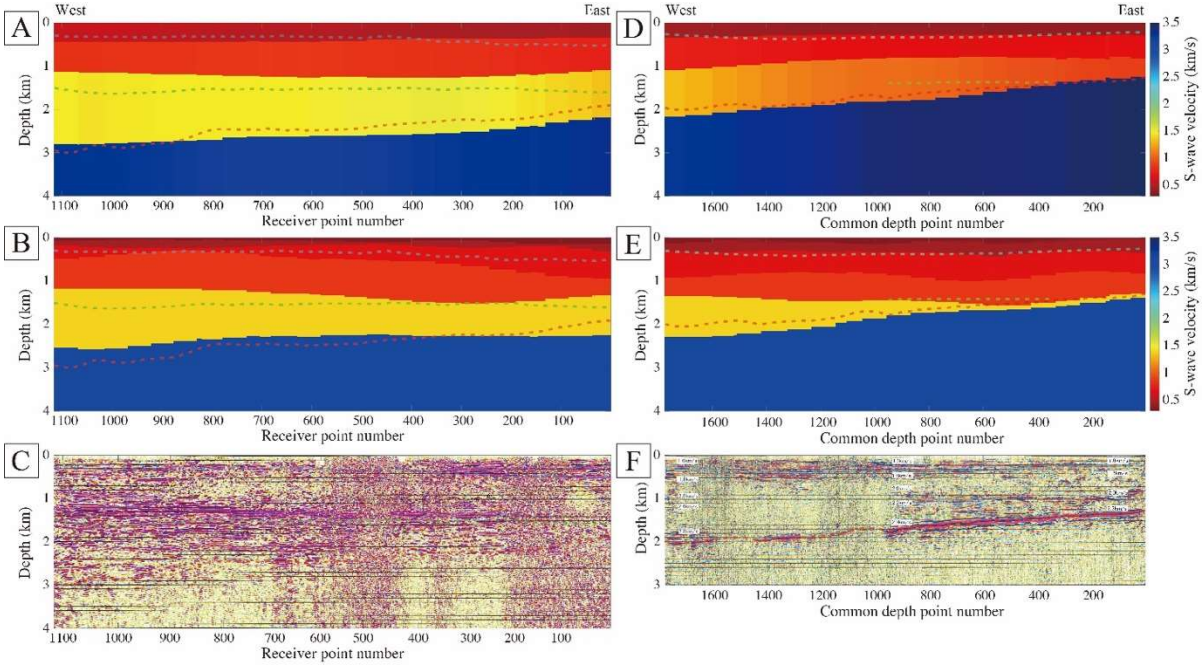

Figure 3.8. *Comparison of the velocity structure along with the P-wave reflection survey lines. (A to C) A vertical slice of (A) the estimated S-wave velocity model and (B) the J-SHIS model along with the seismic reflection survey line of (C) Tokyo (2004) (Fig. 3.11). (D to F) Vertical slice of (D) the estimated S-wave velocity model and (E) the J-SHIS model along with the seismic reflection survey line of (F) Chiba (1999) (Fig. 3.11). Blue, green, and red dashed lines indicate the boundaries between the Shimousa and Kazusa group, Kazusa and Miura group, and Miura group and basement rock, respectively, according to Tokyo (2004) and Chiba (1999) (Fig. 3.14).*

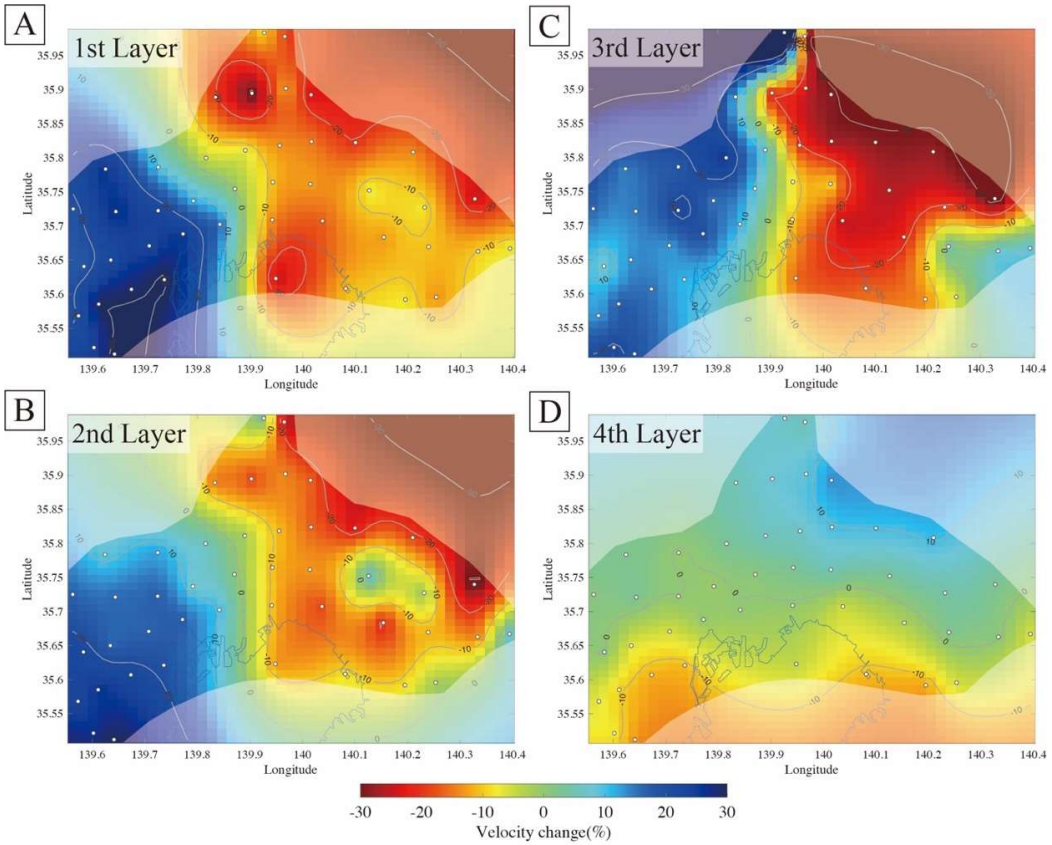

Figure 3.9. *Estimated S-wave velocity perturbation of each layer. (A–D) S-wave velocity perturbation of (A) first, (B) second, (C) third, and (D) the fourth layer. White dots indicate the center of stations in each grid. The extrapolated area is masked.*

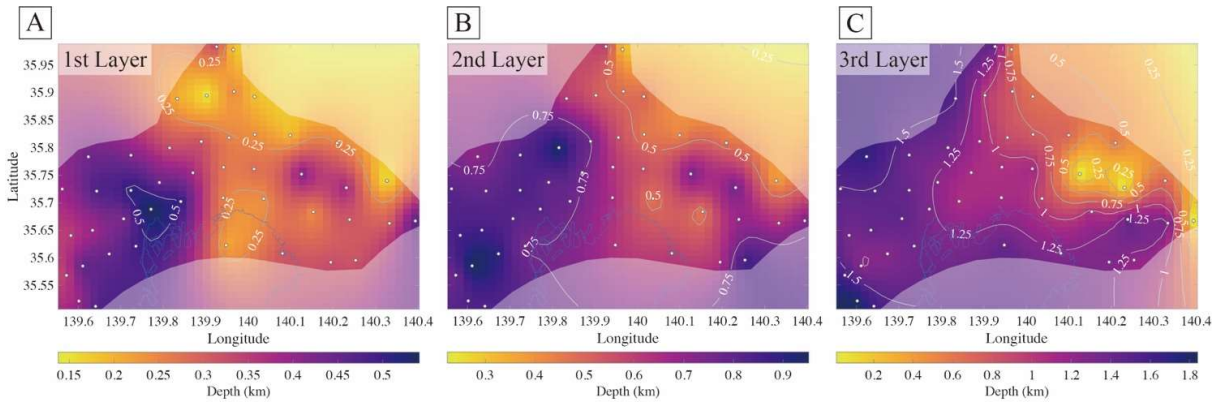

Figure 3.10. *The estimated thickness of each layer. (A–C) The estimated thickness of (A) first, (B) second, and (C) third layer. White dots indicate the center of stations in each grid. The extrapolated area is masked.*

I applied the inversion using multimodal dispersion curves observed at each grid (Fig. 3.1A–C). I constructed the three-dimensional S-wave velocity model using data from the local one-dimensional S-wave velocity structure (Fig. 3.7). Each estimated local solution was horizontally interpolated using the kriging method (Senna et al., 2019). I used the center of gravity of all stations in each array as coordinates instead of the center of each grid (white dots in Fig. 3.7A). The estimated S-wave velocity structure showed a strong velocity contrast between the sediments and the basement rock (Figs. 3.7 and 3.8). Despite the inversions being independent, the estimated S-wave velocity and thickness of each layer were spatially smooth (Figs. 3.9 and 3.10). The S-wave velocity was lower on the northeast side in sedimentary layers, and it was lower on the south side in basement rock (Fig. 3.9). The top of the basement rock tended to be shallower on the northeastern side (Fig. 3.11). Considering the deep boring data (stars in Fig. 3.11A) and previous studies (Koketsu et al., 2009; Suzuki, 2002), the overall trend was generally consistent.

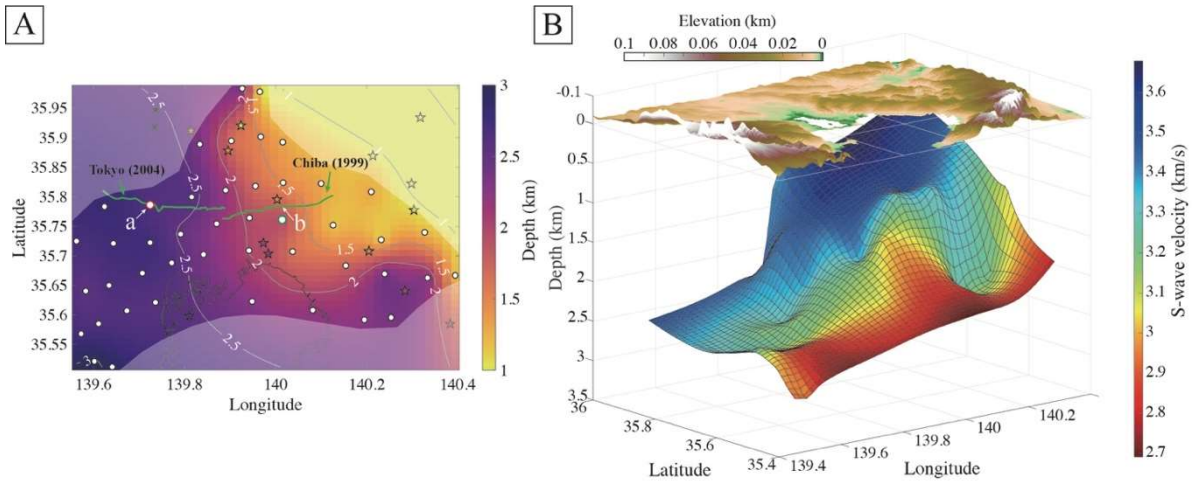

Figure 3.11. *Depth of the basement rock and S-wave velocity. (A) Distribution of the depth of the top of basement rock. The black circles indicate the center of stations in each grid. Stars show the depth of basement rock from the deep borehole (Suzuki, 2002). The extrapolated area is masked. (B) The shape of the top of basement rock and its S-wave velocity. The background color shows the S-wave velocity. The elevation is also mapped above the surface. Note that the ratio of the vertical axis is different between positive and negative.*

3.4. Discussion

I estimated multimodal dispersion curves of Rayleigh and Love waves from cross-correlation of ambient noise. The number of extracted modes tended to be greater on the western side, where the number of stations is higher when compared to that in other areas (Fig. 3.1B, C). That also reflected the lateral homogeneity of the underground structure as the extraction of the higher modes of Rayleigh waves is difficult in heterogeneous structures (Fu et al., 2022). The number of fundamental and first modes of Rayleigh waves decreased in the frequency range of 0.2–0.3 Hz (Fig. 3.1F, G). Around this frequency range, I carefully picked the phase velocities and discarded some phase velocities which are smoothly connected and indistinguishable around this osculation or kissing point (Figs. 3.1D and 3.3A–C).

The inclusion of overtones in simulated data improved the accuracy and precision of the inverted solutions (Figs. 3.2 and 3.5). I could completely estimate a four-layered S-wave velocity structure using up to the second overtone for both Rayleigh and Love waves. Including the second overtone improved the solution convergence by more than 50% (Fig. 3.5). Conversely, using only the fundamental mode could not represent the true model, even when applying the joint inversion of the Rayleigh and Love waves. Presumably, the inversion

problem of the S-wave velocity and thickness was considerably complex to be solved using only the fundamental mode since the model was highly flexible. Since each dispersion curve has different sensitivity to S-wave velocity and thickness (Fig. 3.12), including higher modes constrained the solutions to be estimated. I used simulated data in the frequency range corresponding to the actual observed data, and the dispersion curves of the Rayleigh wave, especially the first overtone, around the osculation point were absent (Fig. 3.1D). Therefore, the effect of the absence of dispersion curves around the osculation point was expected to be apparent but was not clear (Fig. 3.2).

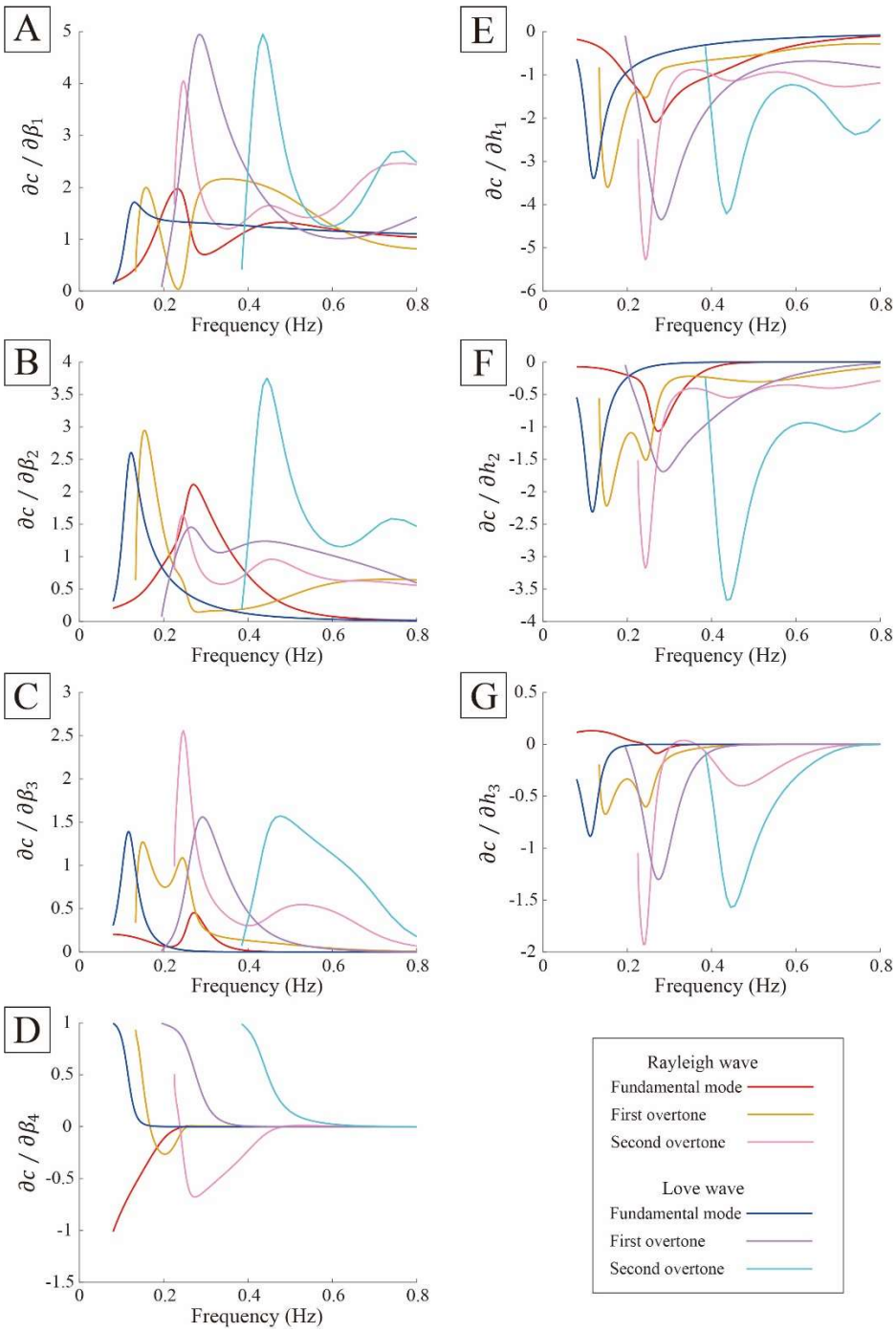

Figure 3.12. *Frequency-depended sensitivity kernels with respect to the S-wave velocity and thickness in grid 'a' in Fig. 3.1B. (A–G) The frequency-depended sensitivity kernels with respect to the S-wave velocity of the first layer (A), second layer (B), third layer (C), and fourth layer (D). The frequency-depended sensitivity kernels with respect to the thickness of the first layer (E), the second layer (F), and the third layer (G). Red, yellow, and pick lines to indicate the sensitivity kernels of fundamental, first and second higher modes of Rayleigh wave, respectively. Blue, purple and light blue lines indicate the sensitivity kernels of fundamental, first and second higher modes of Love wave, respectively.*

The inverted solutions using the observed dispersion curves showed similar results in the simulation tests (Figs. 3.2, 3.4). Including up to the second overtone significantly improved the precision of solutions by about 98% compared to the solutions of the fundamental mode (Fig. 3.6). Although both Rayleigh and Love waves showed improvement in precision by including higher modes, the results of the Rayleigh wave were unstable compared with those of the simulation test. In the result of the Rayleigh wave, the standard deviations of some parameters increased when I used the first overtone. That can be not because the first overtone increases the variance of solutions but because the solutions of only fundamental mode converged wrong values stably (Figs. 3.5 and 3.6). The surface-wave inversion using only the fundamental mode can lead misunderstanding of underground structure. In the case of inversion using up to a second overtone, the variance of the Rayleigh wave is still larger than the cases of Love-wave or joint inversions. Although this can occur due to several reasons, such as underground heterogeneity or uncertainty in dispersion curve estimation, I inferred that the inversion of S-wave velocity using Rayleigh waves was more complicated because they incorporate the sensitivity of not only S-waves but also P-wave velocity. In this study, I used the empirical relationship between the S-wave and P-wave velocities for the Kanto basin (Kitsunezaki et al., 1990; Koketsu et al., 2009; Yamanaka & Yamada, 2006). However, the shape of the objective function could be blurred because the empirical relationship cannot exactly match like in simulation. In such cases, joint inversion can suppress the instability of either inversion and improve the accuracy and precision of inverted solutions. Estimating the multimodal dispersion curves of Rayleigh and Love waves can significantly improve the construction of the velocity model.

I estimated a three-dimensional S-wave velocity model by multimodal surface-wave joint inversion. Since multimodal joint inversion improved the accuracy and precision, the estimated model was smooth, although the inversions were independent at each grid. The shape of the basement rock was consistent (Figs. 3.8 and 3.11) with the results from the Japan Seismic Hazard Information Station (J-SHIS) model (National Research Institute for Earth Science and Disaster Resilience, 2019) and the reflection/refraction surveys for Tokyo and Chiba (Chiba, 1999; Tokyo, 2004). Notably, the J-SHIS model was constructed by integrating existing data derived from boring, seismic reflection/refraction, gravity, and microtremor surveys. Using multimodal dispersion curves, our model estimated from ambient noise is comparable to the model estimated from several geophysical data.

While the shape of each layer was consistent, the distribution of the S-wave velocity differed from that suggested by the J-SHIS model. According to the reflection/refraction surveys of Tokyo (2004) and Chiba (1999), the third layer (Miura group) has low thickness eastwards, a trend that is also reflected in the J-SHIS model. In contrast, our estimated model

showed a gradual velocity change. The boundary in the seismic profile was defined considering the geological boundary of the near-boring data (Chiba, 1999; Tokyo, 2004). As our estimated S-wave velocity structure was constructed to optimally reproduce the observed surface-wave dispersion curves, complete consistency with the seismic profile was unnecessary. Furthermore, the surface wave could not reflect the thin layer due to the large wavelength of the surface wave.

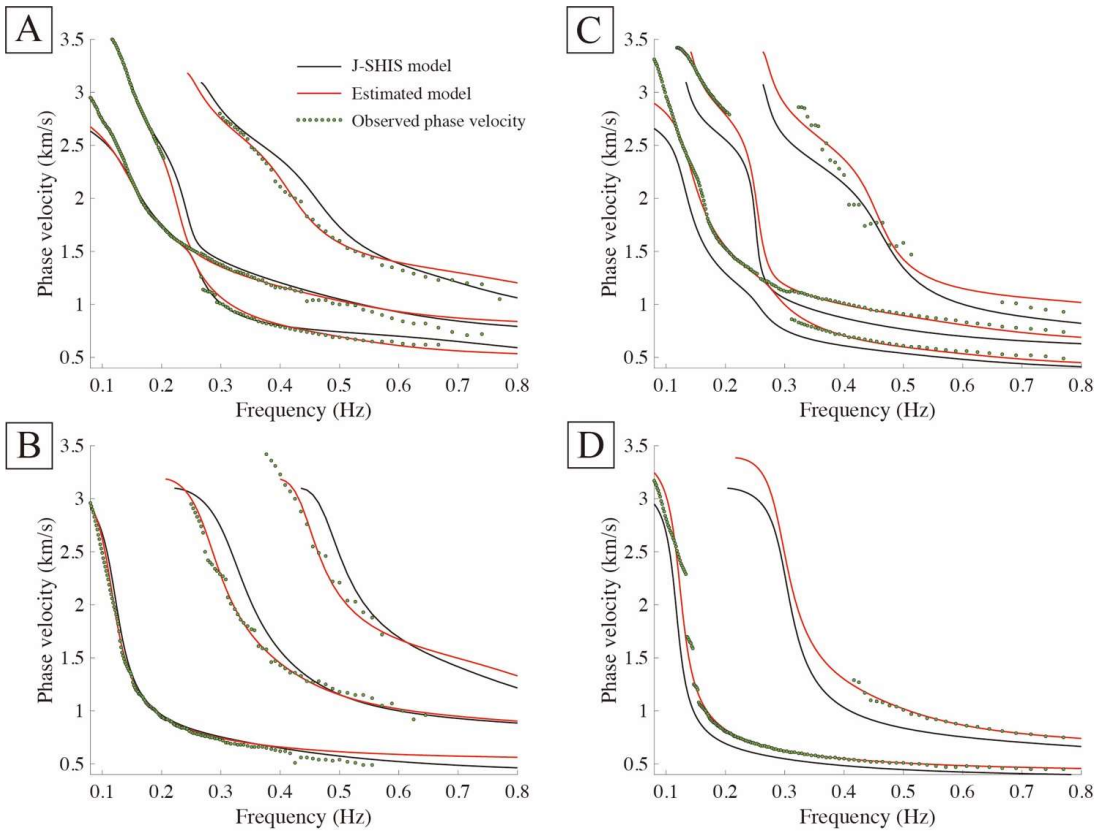

Figure 3.13. *Comparison of the dispersion curves estimated from the J-SHIS model and our estimated model. (A–B) Theoretical dispersion curves of (A) the Rayleigh wave and (B) the Love wave. The black line indicates the theoretical dispersion curves from the J-SHIS model at the 'a' on the survey line of Tokyo (2002) in Fig. 3.11A. The red line indicates the theoretical dispersion curves from our estimated model at the red circle in Fig. 3.11A. Green dots indicate observed phase velocities at the red circle in Fig. 3.11A. (C–D) Same as (A) and (B), but at the 'b' on the survey line of Chiba (1999) in Fig. 3.11A.*

A comparison of the theoretical dispersion curves suggested by the J-SHIS model and our observed dispersion curves showed that only the fundamental mode dispersion curves were consistent with the observed curves in the west ('a' in Fig. 3.11A), with the higher modes being

different from the observed curves (Fig. 3.13A, B). In the eastern part ('b' in Fig. 3.11A), however, the fundamental-mode dispersion curves differed from the observed curves (Fig. 3.13C, D). These results indicated that our velocity model accurately reflected the S-wave velocity structure, which in turn reflected the observed dispersion curves using multimodal joint inversion. The S-wave velocity model which better explain the property of propagation of surface waves improve the earthquake simulation and hazard assessment. Our velocity model revealed that the sediments were relatively softer towards the east and northeast (Figs. 3.8 and 3.9).

The S-wave velocity of the basement rock tended to be higher towards the north (Figs. 3.11B and 3.9D), which was generally consistent with the P-wave velocity reported by Koketsu et al. (2009). The increase in velocity towards the north likely reflects the geological belt of basement rocks whose age increases from south to north (Suzuki, 2002; Yajima, 1981). Although the geological model and P-wave velocity of Koketsu et al. (2009) suggested a linear boundary, our model showed a curved velocity contour. Considering the complex formation of the basement rock of the Kanto Basin, it is likely that these boundaries are nonlinear. Our velocity model revealed the distribution of basement rock at a high resolution while using only surface-wave dispersion data.

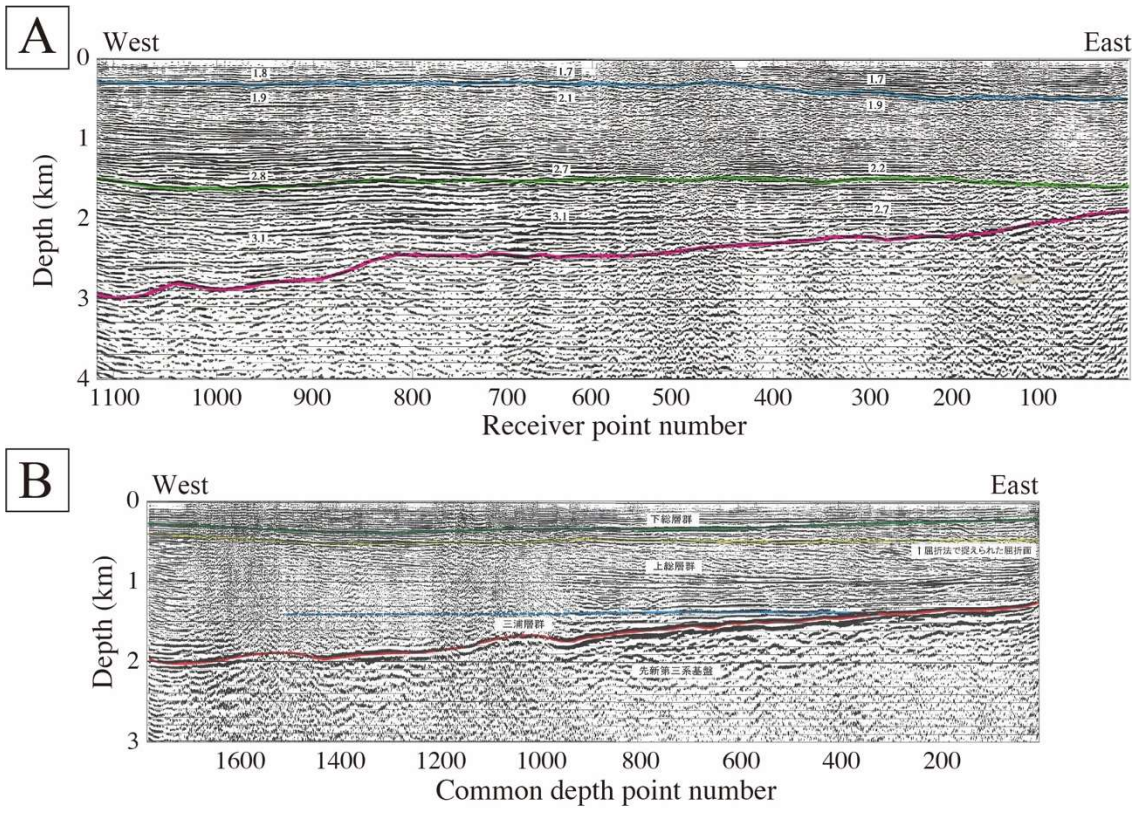

Figure 3.14. *Interpretation of P-wave seismic profile. (A) The P-wave seismic profile and its interpretation of Tokyo (2004). Blue, green, and red lines indicate the boundaries between the Shimousa and Kazusa group, Kazusa and Miura group, and Miura group and basement rock, respectively. (B) The P-wave seismic profile and its interpretation of Chiba (1999). Green, blue, and red lines indicate the boundaries between the Shimousa and Kazusa group, Kazusa and Miura group, and Miura group and basement rock, respectively. The yellow line indicates the boundary of the refraction survey (Chiba, 1999; Tokyo, 2004).*

3.5. Conclusion

This study proposed a three-dimensional S-wave velocity model estimated by joint inversion using multimodal Rayleigh and Love waves. Including higher modes improved the accuracy and precision of the inverted solutions by at least 50% in the simulation test. The error of inversion using actual observed data decreased by more than 98% when I added the first and second overtone to the fundamental mode. The high-precision multimodal joint inversion constructed smooth three-dimensional S-wave velocity model, despite the inversions being independent. Our estimated model revealed a low-velocity anomaly of sediments towards the east and a curved velocity contour of the basement rock. Such structures better explain the observed surface-wave dispersion curves than the J-SHIS model. This model could successfully estimate the three-dimensional S-wave velocity, including that of the basement rock, using only surface-wave dispersion data from ambient noise, which has significant implications. The high-resolution three-dimensional S-wave velocity model is essential to understanding the complex amplification of surface waves which cause strong motion, especially in a basin. Our velocity model can improve the earthquake simulation and hazard assessment.

References

Aki, K. Space and time spectra of stationary stochastic waves, with special reference to microtremors. *Bulletin. Earthquake Research Institute, University of Tokyo*, *35*(3), 415–456 (1957).

Arfken, G. B., Weber, H. J., & Harris, F. E. *Mathematical Methods for Physicists: A Comprehensive Guide*. London: Academic Press (2005).

Boaga, J., Cassiani, G., Strobbia, C. L., & Vignoli, G. Mode misidentification in Rayleigh waves: Ellipticity as a cause and a cure. *Geophysics*, *78*(4). https://doi.org/10.1190/GEO2012-0194.1 (2013).

Boúe, P., Denolle, M., Hirata, N., Nakagawa, S., & Beroza, G. C. Beyond basin resonance : Characterizing wave propagation using a dense array and the ambient seismic field. *Geophysical Journal International*, *206*(2), 1261–1272. https://doi.org/10.1093/gji/ggw205 (2016).

Chiba. *Subsurface structure survey in Chiba prefecture in 1999 (in Japanese)* (1999).

Denolle, M. A., Miyake, H., Nakagawa, S., Hirata, N., & Beroza, G. C. Long-period seismic amplification in the Kanto Basin from the ambient seismic field. *Geophysical Research Letters*, *41*(7), 2319–2325. https://doi.org/10.1002/2014GL059425 (2014).

Denolle, M. A., Boué, P., Hirata, N., & Beroza, G. C. Strong Shaking Predicted in Tokyo From an Expected M7+ Itoigawa-Shizuoka Earthquake. *Journal of Geophysical Research: Solid Earth*, *123*(5), 3968–3992. https://doi.org/10.1029/2017JB015184 (2018).

Efron, B., & Tibshirani, R. J. *An Introduction to the Bootstrap*. New York: Chapman and Hall/CRC. (1994).

Erdélyi, A., Magnus, W., Oberhettinger, F., & Tricomi, F. G. *Tables of Integral Transforms*. New York: McGraw-Hill. (1954).

Fu, L., Pan, L., Li, Z., Dong, S., Ma, Q., & Chen, X. Improved High-Resolution 3D Vs Model of Long Beach, CA: Inversion of Multimodal Dispersion Curves From Ambient Noise of a Dense Array. *Geophysical Research Letters*, *49*(4). https://doi.org/10.1029/2021GL097619 (2022).

Grayver, A. V., & Kuvshinov, A. V. Exploring equivalence domain in nonlinear inverse problems using Covariance Matrix Adaption Evolution Strategy (CMAES) and random sampling. *Geophysical Journal International*, *205*(2), 971–987. https://doi.org/10.1093/gji/ggw063 (2016).

Haney, M. M., Mikesell, T. D., van Wijk, K., & Nakahara, H. Extension of the spatial autocorrelation (SPAC) method to mixed-component correlations of surface waves. *Geophysical Journal International*, *191*(1), 189–206. https://doi.org/10.1111/j.1365-246X.2012.05597.x (2012).

Hansen, N., & Ostermeier, A. Completely derandomized self-adaptation in evolution strategies. *Evolutionary Computation*, *9*(2), 159–195. https://doi.org/10.1162/106365601750190398 (2001).

Hansen, Nikolaus. The CMA Evolution Strategy: A Tutorial. Retrieved from http://arxiv.org/abs/1604.00772 (2016).

Herrmann, R. B. Computer programs in seismology: An evolving tool for instruction and research. *Seismological Research Letters*, *84*(6), 1081–1088. https://doi.org/10.1785/0220110096 (2013).

Hu, S., Luo, S., & Yao, H. The frequency-bessel spectrograms of multicomponent cross-correlation functions from seismic ambient noise. *Journal of Geophysical Research: Solid Earth*, *125*(8), 1–20. https://doi.org/10.1029/2020JB019630 (2020).

Kano, M., Nagao, H., Nagata, K., Ito, S., Sakai, S., Nakagawa, S., et al. Seismic wavefield imaging of long-period ground motion in the Tokyo metropolitan area, Japan. *Journal of Geophysical Research: Solid Earth*, *122*(7), 5435–5451. https://doi.org/10.1002/2017JB014276 (2017).

Kano, M., Nagao, H., Sakai, S., Nakagawa, S., Mizusako, S., Hori, M., Hirata, N., Shiomi, K., Honda, R. Azimuth Verification of the MeSO-net Seismographs. *Zisin*, *68*(2), 31–44. https://doi.org/10.4294/zisin.68.31 (2015).

Kitsunezaki, C., Goto, N., Kobayashi, Y., Ikawa, T., Horike, M., Saito, T., et al. Estimation of P- and S- Wave Velocities in Deep Soil Deposits for Evaluating Ground Vibrations in Earthquake. *Japan Society for Natural Disaster Science*, *9*(3), 1–17. (1990).

Koketsu, K., & Kikuchi, M. Propagation of seismic ground motion in the Kanto basin, Japan. *Science*, *288*(5469), 1237–1239. https://doi.org/10.1126/science.288.5469.1237 (2000).

Koketsu, K., Miyake, H., Afnimar, & Tanaka, Y. A proposal for a standard procedure of modeling 3-D velocity structures and its application to the Tokyo metropolitan area, Japan. *Tectonophysics*, *472*(1–4), 290–300. https://doi.org/10.1016/j.tecto.2008.05.037 (2009).

Komazawa, M., & Hasegawa, I. The graven structure suggested by the gravimetric basement in the Kanto district, central Japan. *Memoirs of the Geological Society of Japan*, *31*, 57-74 (in Japanese). (1988).

Löer, K., Riahi, N., & Saenger, E. H. Three-component ambient noise beamforming in the Parkfield area. *Geophysical Journal International*, *213*(3), 1478–1491. https://doi.org/10.1093/GJI/GGY058 (2018).

Luo, Y., Xia, J., Liu, J., Liu, Q., & Xu, S. Joint inversion of high-frequency surface waves with fundamental and higher modes. *Journal of Applied Geophysics*, *62*(4), 375–384. https://doi.org/10.1016/j.jappgeo.2007.02.004 (2007).

Munch, F. D., Khan, A., Tauzin, B., Zunino, A., & Giardini, D. Stochastic Inversion of P -to-S Converted Waves for Mantle Composition and Thermal Structure: Methodology and Application. *Journal of Geophysical Research: Solid Earth*, 2018JB016032. https://doi.org/10.1029/2018JB016032 (2018).

National Research Institute for Earth Science and Disaster Resilience. Shallow and deep layers combined model (SDLCM). National Research Institute for Earth Science and Disaster Resilience. https://doi.org/10.17598/nied.0012 (2019).

National Research Institute for Earth Science and Disaster Resilience. *NIED MeSO-net*. National Research Institute for Earth Science and Disaster Resilience. https://doi.org/10.17598/NIED.0023 (2021).

Sato, H., Hirata, N., Koketsu, K., Okaya, D., Abe, S., Kobayashi, R., et al. Geology: Earthquake source fault beneath Tokyo. *Science*, *309*(5733), 462–464. https://doi.org/10.1126/science.1110489 (2005).

Senna, S., Wakai, A., Fujiwara, H., Jin, K., Yatagai, A., Suzuki, H., et al. Modeling of the subsurface structure from the seismic bedrock to the ground surface for a broadband strong motion evaluation in Japan. *Earthquake Geotechnical Engineering for Protection and Development of Environment and Constructions- Proceedings of the 7th International Conference on Earthquake Geotechnical Engineering, 2019*, *13*(5), 4931–4938. https://doi.org/10.20965/jdr.2013.p0889 (2019).

Suzuki, H. Underground Geological Structure beneath the Kanto Plain, Japan (in Japanese with English abstract). *Report of the National Research Institute for Earth Science and Disaster Prevention*, *63*, 1–19. https://doi.org/http://doi.org/10.24732/nied.00001131 (2002).

Takagi, R., Nishida, K., Maeda, T., & Obara, K. Ambient seismic noise wavefield in Japan characterized by polarization analysis of Hi-net records. *Geophysical Journal International*, *215*(3), 1682–1699. https://doi.org/10.1093/gji/ggy334 (2018).

Tokyo. *Subsurface structure survey of Kanto plain in 2004 (in Japanese)*. (2004).

Viens, L., Jiang, C., & Denolle, M. A. Imaging the Kanto Basin bedrock with noise and earthquake autocorrelations. *Geophysical Research Letters*, 1–14. (2020).

Wang, J., Wu, G., & Chen, X. Frequency-Bessel Transform Method for Effective Imaging of Higher-Mode Rayleigh Dispersion Curves From Ambient Seismic Noise Data. *Journal of Geophysical Research: Solid Earth*, *124*(4), 3708–3723. https://doi.org/10.1029/2018JB016595 (2019).

Wu, G. Xiong, Pan, L., Wang, J. nan, & Chen, X. Shear Velocity inversion using multimodal dispersion curves from ambient seismic noise data of USArray transportable array. *Journal of Geophysical Research: Solid Earth*, *125*(1), 1–14. https://doi.org/10.1029/2019JB018213 (2020).

Yajima, T. Petrological characteristics and geological structure of the pre-Tertiary basement of Kanto plain. *Memoirs of the Geological Society of Japan*, *20*, 187-206 (in Japanese). (1981).

Yamanaka, H., & Yamada, N. Estimation of 3D S-wave Velocity Model of the Kanto Basin, Japan, Using Rayleigh Wave Phase Velocity. *Bulletin of the Earthquake Research Institute*, *81*(3/4), 295–301. (2006).

Yamanaka, H., Takemura, M., Ishida, H., Ikeura, T., Nozawa, T., Sasaki, T., & Niwa, M. Array Measurements of Long-Period Microtremors and Estimation of S-Wave Velocity Structure in the Western Part of the Tokyo Metropolitan Area. *Zisin*, *47*, 163–172. (1994).

Yamaya, L., Mochizuki, K., Akuhara, T., & Nishida, K. Sedimentary Structure Derived From Multi-Mode Ambient Noise Tomography With Dense OBS Network at the Japan Trench. *Journal of Geophysical Research: Solid Earth*, *126*(6), 1–20. https://doi.org/10.1029/2021JB021789 (2021).

Zhan, W., Pan, L., & Chen, X. A widespread mid-crustal low-velocity layer beneath Northeast China revealed by the multimodal inversion of Rayleigh waves from ambient seismic noise. *Journal of Asian Earth Sciences*, *196*(April), 104372. https://doi.org/10.1016/j.jseaes.2020.104372 (2020).

Chapter 4

Spatial and temporal seismic velocity changes on Kyushu Island during the 2016 Kumamoto earthquake

Abstract

Monitoring earthquake faults and volcanoes contributes to our understanding of their dynamic mechanisms and our ability to predict future earthquakes and volcanic activity. I report here on spatial and temporal variations of seismic velocity around the seismogenic fault of the 2016 Kumamoto earthquake [moment magnitude (Mw) 7.0] based on ambient seismic noise. Seismic velocity near the rupture faults and the Aso volcano decreased during the earthquake. The velocity reduction near the faults may have been due to formation damage, a change in a stress state, and an increase in pore pressure. Further, I mapped the post-earthquake fault-healing process. The largest seismic velocity reduction observed at the Aso volcano during the earthquake was likely caused by pressurized volcanic fluids. The large increase in seismic velocity at the volcano's magma body was observed ~3 months after the earthquake, which may have responded to depressurization caused by the eruption. This study demonstrates the usefulness of continuous monitoring of faults and volcanoes.

Keywords: Ambient noise, Monitoring, Kumamoto Earthquake, Aso volcano

4.1. Introduction

Seismic velocity in crustal rocks changes during earthquakes by several mechanisms related to, for example, fault zone damage, pore pressure and stress state changes (for example, pressure perturbation), and healing processes (Brenguier et al., 2008a; Brenguier et al., 2014; Chaves & Schwartz, 2016; Minato et al., 2012; Nakata & Snieder, 2011; Niu et al., 2008; Vidale & Li, 2003; Wegler & Sens-Schönfelder, 2007;). Seismic velocity variations can often be explained by the presence of cracks; earthquake ruptures and associated abnormal pore pressure generate open cracks in the crust, and the generation of cracks changes the crust's elastic properties, including seismic velocity (Toksöz et al., 1976; Tsuji et al., 2008). Therefore, seismic velocity is a key geophysical property for characterizing dynamic processes and the status of deep faults. Further, previous studies have shown that seismic velocity associated with eruptions in volcanic areas varies greatly, mainly because of increased pore pressure around the magmatic body (Brenguier et al., 2014; Brenguier et al., 2016; Brenguier et al., 2008b; Budi-Santoso & Lesage, 2016). In particular, seismic velocity shows large variation under high pore pressure conditions because even minor increases in pore pressure under these conditions easily generate cracks, thereby influencing seismic velocity (Toksöz et al., 1976).

Several studies have observed changes in seismic velocity due to earthquakes or volcanic activity by using multiplet earthquake analysis (Hotovec-Ellis et al., 2014; Poupinet et al., 1984), controlled source experiments (Nishimura et al., 2000; Niu et al., 2008), and seismic interferometry (Brenguier et al., 2008a; Brenguier et al., 2014; Brenguier et al., 2008b; Minato et al., 2012; Nakata & Snieder, 2011; Obermann et al., 2014; Obermann et al., 2013; Wegler & Sens-Schönfelder, 2007). Although seismic velocity variation between several seismometer pairs has been reported using these approaches, temporal variation of seismic velocity along intraplate faults has yet to be mapped using many seismometer pairs. Here, by applying seismic interferometry to ambient noise data, I reveal the temporal and spatial variation of seismic velocity due to the 2016 Kumamoto earthquake and volcanic activity at Aso volcano in central Kyushu Island, Japan.

The 2016 Kumamoto earthquake took place in the central part of Kyushu Island, where dozens of Hi-net seismic stations (Okada et al., 2004) were deployed (Fig. 4.1). This earthquake comprised a series of temblors along with the Hinagu-Futagawa fault system (Asano & Iwata, 2016; Geospatial Information Authority of Japan; Kato et al., 2016; Yagi et al., 2016). Their source mechanisms typically indicated right-lateral motion, consistent with the north-south tectonic extension of central Kyushu (Matsumoto et al., 2015). The series began along with the Hinagu fault system (oriented north-northeast–south-southwest) with a moment magnitude (Mw) 6.2 foreshock on 14 April (Fig. 4.1). The largest event of the series (Mw 7.0),

the mainshock, occurred 28 hours later (16 April) along with the Futagawa fault system (oriented northeast-southwest) (Asano & Iwata, 2016; Yagi et al., 2016). The maximum displacement along the fault plane, modeled from surface deformation data, was ~6 m and was observed west of Mount Aso (Yagi et al., 2016), and the depth of the fault rupture was shallower than 10 km. The mainshock rupture was halted at the Aso caldera complex. Two hours after the mainshock, a series of ruptures occurred successively farther northeast, beginning with an Mw 5.8 event near Mount Aso (Fig. 4.1). High volcanic tremor activity around Mount Aso was observed before the Kumamoto earthquake (Ozawa et al., 2016), and the higher activity level continued after the earthquake. Aso volcano erupted on 16 April, and 1 May 2016, and these small eruptions were followed by a large eruption on 7 and 8 October 2016 (Miyakawa et al., 2016). The spatial and temporal variation of seismic velocity derived by seismic interferometry can be used to estimate stress and pressure perturbation associated with seismic activity. Therefore, we can infer that stress and pressure perturbation due to the 2016 earthquake likely caused the other earthquakes and activated the volcano.

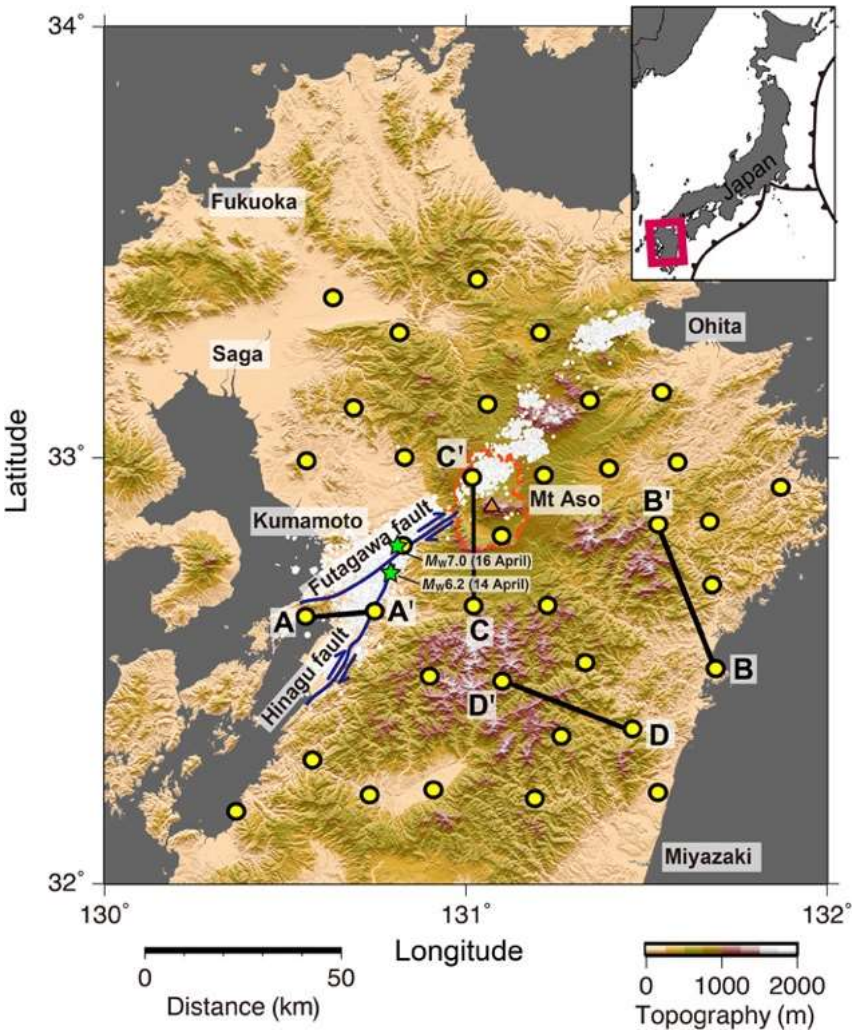

Figure 4.1. *Map of central Kyushu Island, Japan, with locations of Hi-net stations (yellow dots). Hypocenters of large earthquakes and aftershocks associated with the 2016 Kumamoto earthquake are shown by green stars and white dots, respectively. A dashed orange line outlines the Aso caldera. The black lines connect the seismometer pairs shown in Figs. 4.3, 4.2 and 4.4. The base map is a 10-m mesh digital elevation model published by the Geospatial Information Authority of Japan. I drew this figure with Generic Mapping Tools (Wessel & Smith, 1998).*

4.2. Data and Methods

4.2.1 Computing daily cross-correlations

I divided 1 day of continuous ambient noise data into 30-min segments with a 50% overlap (Seats et al., 2012). I then corrected the instrumental response and applied a 0.1- to 0.9-Hz band-pass filter to each segment. To remove earthquake data, I rejected any segment in which the maximum absolute value exceeded a specified threshold (Bensen et al., 2007; Seats et al., 2012). I computed the mean and SD of the absolute value in each window. I applied four threshold values: 5, 7, 9, and 11 times the SD of the mean. To keep a certain number of segments each day, I gradually increased the threshold value until more than half of the segments satisfied the threshold. The daily cross-correlations were computed by stacking each segment of power-normalized cross-correlations (cross-coherence) between receiver pairs in the frequency domain (Nakata et al., 2015; Nakata et al., 2011).

4.2.2 Estimating seismic velocity change by stretching interpolation

To estimate seismic velocity changes, I used a stretching interpolation technique (Hadziioannou et al., 2009; Meier et al., 2010; Minato et al., 2012). The method elongates the time axis and finds the most similar trace to the reference trace

$$f_{\varepsilon}^{cur}(t) = f^{cur}\big(t(1+\varepsilon)\big), \tag{4.1}$$

$$C(\varepsilon) = \frac{\int f_{\varepsilon}^{cur}(t) f^{ref}(t)dt}{\left(\int \left(f_{\varepsilon}^{cur}(t)\right)^2 dt \int \left(f^{ref}(t)\right)^2 dt\right)^{1/2}}, \tag{4.2}$$

where ε is a stretching parameter, f^{ref} represents the reference trace, f^{cur} represents the current trace, and $C(\varepsilon)$ is the correlation coefficient between the reference and

the current trace. The parameter ε corresponds to a relative time shift $\left(\frac{\Delta t}{t}\right)$ and relates to a velocity change $\left(\frac{\Delta v}{v}\right)$ as follows

$$\varepsilon = \frac{\Delta t}{t} = -\frac{\Delta v}{v}, \tag{4. 3}$$

I estimated the relative velocity change ϵ that maximizes $C(\varepsilon)$ by adopting a grid search algorithm and a ternary search algorithm. A positive value of ε indicates a decrease in velocity compared to the reference trace.

In our study, the stretching interpolation technique was applied to the coda of cross-correlations because the coda is more sensitive to velocity change than the direct wave (Meier et al., 2010) and less sensitive to variations in noise sources (Chaves & Schwartz, 2016). The reference trace was defined as the coda of cross-correlations of a 1-year stack, and the current trace was defined as the coda of cross-correlations of a 30-day stack. Following Meier *et al.* (Meier et al., 2010), I selected a 100-s window for the coda. I calculated $C(\varepsilon)$ for the range $-0.025 < \varepsilon < 0.025$ with a step size of 0.0005 and picked ε with the maximum value of $C(\varepsilon)$. By applying the ternary search method, I estimated the seismic velocity change ε with a resolution of $\sim 5 \times 10^{-7}$. I further divided the 100-s window into six smaller time windows of 50 s each and applied the stretching interpolation technique in each window to compute SDs of estimates of ε (Meier et al., 2010). The measured velocity change was considered to represent the velocity change in the middle of the 30-day window. By moving the 30-day window used for the current trace, I estimated the daily variation of the velocity change.

Cross-correlations have causal (positive-time) and anticausal (negative-time) sides, corresponding to a wave traveling from station D to station D′ and from station D′ to station D (for example, Fig. 4.2). Therefore, the stretching interpolation technique can be applied to both positive- and negative-time parts. However, I used only the positive- or negative-time part to reduce the effects of strong volcanic tremors from the Aso volcano (Kawakatsu et al., 2000; Sassa, 1935), as described later.

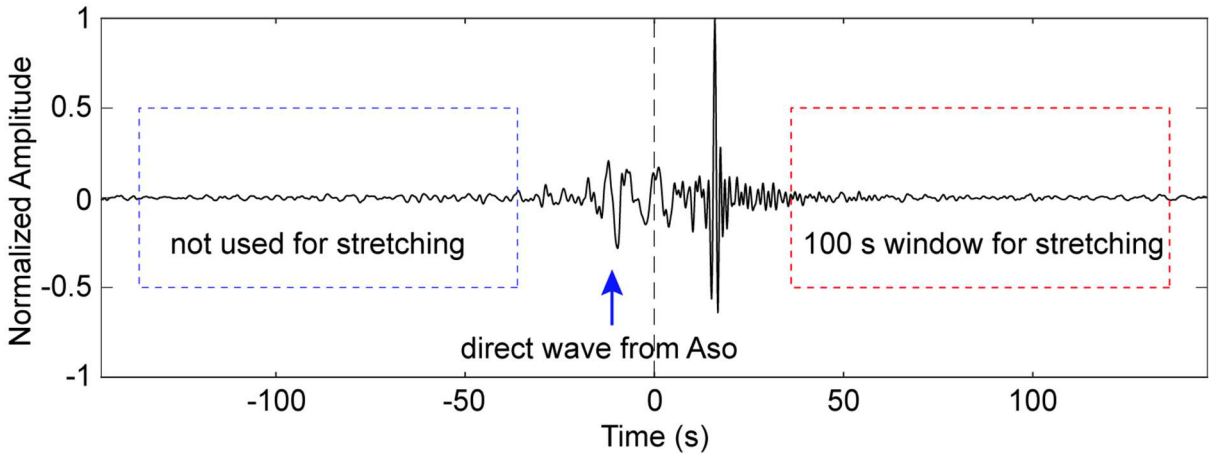

Figure 4.2. *Asymmetry of cross-correlation between station D and D′ (1-year stack) due to tremors from Aso volcano. The receiver location is shown in Fig. 4.1. Positive time indicates the wave traveling from D to D′, and negative time indicates the wave traveling from D′ to D and includes the direct wave from Aso volcano. Dashed lines show the 100-s window for the stretching interpolation, but I applied the stretching technique only to the positive-time (red dashed rectangle) window that does not include the direct wave from Aso in the domain.*

The estimated velocity change is the relative velocity variation of the reference trace, including ambient noise before and after the 2016 Kumamoto earthquake. To measure the velocity change caused by the earthquake, I subtracted averaged velocity variations before the earthquake from the estimated velocity change ε as follows

$$\varepsilon' = \varepsilon - \varepsilon_0, \tag{4. 4}$$

I note that the averaged velocity change ε_0 was obtained by averaging the estimates of velocity changes before the earthquake (from 15 December 2015 to 29 March 2016). In this chapter, I display the relative velocity variation $\frac{\Delta v}{v} = -\varepsilon'$ to clarify the velocity changes associated with the 2016 earthquake.

4.2.3 Estimating seismic velocity change by MWCS analysis

I also tested an MWCS analysis (Brenguier et al., 2008a; Brenguier et al., 2008b; Clarke et al., 2011; Sens-Schönfelder & Wegler. 2006) to estimate seismic velocity change (Fig. 4.4). Similar to the stretching interpolation, I computed temporal velocity change between the coda of cross-correlations of a 1-year stack and the coda of cross-correlations of a 30-day

stack. The frequency range in this analysis was 0.1 to 0.9 Hz. I applied MWCS analysis for the time window between the starting time of the window for the stretching interpolation analysis and a lapse time of 60 s (Brenguier et al., 2014). In our analysis, I use a moving time window of 10 s with an overlap of 80% (Brenguier et al., 2014; Chaves & Schwartz, 2016). I basically followed the MWCS processing procedures of Clarke *et al*. (2011). However, I did not apply phase unwrapping of the cross-spectrum between the current and reference traces in each moving time window because it was difficult to obtain stable results for several receiver pairs after applying phase unwrapping. Therefore, the maximum velocity change I could measure in this approach was limited as lapse time and frequency increased. For example, at a lapse time of 60 s and a frequency of 0.80 Hz, the maximum velocity change is ~1%. This value is mostly within the range of estimated velocity variation by the stretching interpolation (Fig. 4.4).

4.2.4 Influence of volcanic tremors from Aso volcano

The ambient noise data used in this study include persistent volcanic tremors from the Aso volcano (Kawakatsu et al., 2000; Sassa, 1935). In the cross-correlations, I observed strong signals associated with volcanic tremors from the Aso volcano (for example, see Fig. 4.2). The direct wave from Aso was detected as a low-frequency signal. Because the tremors at Aso were spatially localized, they were not symmetric in the cross-correlations. However, even if the noise is localized, the effect of noise directivity can be reduced by using the coda wave (Colombi et al., 2014).

The disadvantage of the stretching interpolation technique is that it can induce an apparent velocity change if the frequency component of the ambient noise varies (Zhan et al., 2013). Therefore, if the frequency component of the tremors at Aso varied, then an apparent velocity change would be introduced in the estimated velocity change. In our analysis, to reduce the effects of the tremors at Aso, I applied the stretching interpolation technique to either the causal or the anticausal part of the coda, choosing that in which the signals of the tremors at Aso were weak. For this purpose, I first estimated the domain (causal or anticausal) of the direct waves from Aso based on the geometry among Aso volcano and the two stations used for the cross-correlations, and then selected the opposite window for the stretching analysis (for example, positive-time in Fig. 4.2).

The cross-correlation coefficient in the stretching analysis across the Aso volcano is lower after the large eruption on 7 and 8 October (Fig. 4.3). The lower coefficient in the stretching analysis demonstrates that the ambient noise characteristics around Aso, such as source locations and frequency components of noise, were changed by the large eruption. Because the seismometer pair (C-C′) crosses the Aso noise source, I could not efficiently remove the influence of ambient noise variation at the Aso volcano.

On the other hand, temporal change in seismic velocity measured by the MWCS is likely less affected by a temporal change in the amplitude spectrum of ambient noise because only phase information is used in velocity variation measurements (Zhan et al., 2013). However, in the MWCS, I need to assume a constant time shift in each moving time window. Although a longer time window in the MWCS reduces the fluctuation in time shift measurements due to noise, the assumption of a constant time shift is more erroneous when the window length is increased (Hadziioannou et al., 2011).

To evaluate the reliability of measurements of temporal velocity change by the stretching interpolation and the MWCS for our data, I compared temporal velocity variations of several receiver pairs using both techniques (Fig. 4.4). The velocity change derived from the MWCS is similar to that from the stretching interpolation between A and A′ (Fig. 4.4A). For this receiver pair, I observed high stability in velocity change estimation during linear regression in the MWCS (Fig. 4.4D). However, the velocity changes derived by the MWCS are different from those by the stretching interpolation for the receiver pairs of B-B′ and C-C′ (Fig. 4.4, B and C). Between B and B′, the measured time shifts are not well fitted to the straight line in the negative-lag time where direct waves from Aso are included (Fig. 4.4E). Between C and C′, the measured time shifts do not show a clear linear trend in positive- and negative-lag times, indicating the difficulty of linear regression in measuring velocity change (Fig. 4.4F). That probably indicates that both positive- and negative-lag times are affected by the tremors at Aso because the Aso volcano is located between C and C′ (Fig. 4.1).

To stabilize velocity change estimation in the MWCS, we usually use both positive- and negative-lag times. However, because virtual seismograms for either positive- or negative-lag time or both around Aso volcano are influenced by tremors at Aso (Fig. 4.2), using both lag times decreased the stability of velocity estimation (that is, lack of a clear linear trend in Fig. 4.4, E and F). On the other hand, I could apply the stretching interpolation by selecting either positive- or negative-lag time where the influence of tremors at Aso was small. Thus, I obtained more stable results using the stretching interpolation in central Kyushu Island.

4.2.5 Mapping changes in seismic velocity

I obtained seismic velocity changes between pairs of seismic stations (Fig. 4.5). For each station, I estimated velocity changes between that station and other stations within <40 km. The averaged velocity changes were assigned at each station as in the study by Brenguier et al. (2014). I then used a linear interpolation technique to obtain a map of the velocity changes (see Fig. 4.6).

4.2.6 Proxy of depth resolution

To evaluate the depth range associated with the estimated surface wave velocity changes (Figs. 4.3 and 4.6), I calculated depth-dependent sensitivity kernels for fundamental

mode Rayleigh waves with respect to *S*-wave velocity (Fig. 4.7) (Takeuchi & Saito, 1972). The sensitivity kernels were computed by the DISPER 80 program (Saito, 1988) for a 1D layered model near Mount Aso estimated by Nishida et al. (2008). A similar evaluation method is described by Chaves & Schwartz (2016). Note that the sensitivity kernels for higher frequencies might not be accurate because Nishida et al. (2008) analyzed Love and Rayleigh waves below 0.2 Hz, and shallow sediments were not included in their model.

4.3. Results

To retrieve virtual seismograms of seismic waves propagating between pairs of stations (Fig. 4.3, A to C), I applied seismic interferometry (Derode et al., 2003; Wapenaar & Fokkema, 2006) to the ambient noise recorded at 36 Hi-net seismic stations (Fig. 4.1) from December 2015 to November 2016. I estimated the daily variation of seismic velocity by applying a stretching interpolation technique (Meier et al., 2010) and a moving-window cross-spectral (MWCS) technique (Brenguier et al., 2008a; Brenguier et al., 2008b; Clarke et al., 2011; Sens-Schönfelder & Wegler, 2006) to the coda wave on the virtual seismogram. Although the relative velocity changes are calculated from both techniques, the results from the MWCS were unstable mainly because of tremors at Mount Aso. Therefore, I decided to use the stretching technique for further analyses. By assuming that surface waves were dominant in the coda (Obermann et al., 2015), I used the frequency-dependent depth sensitivity of surface waves in our interpretation (Fig. 4.7). The surface wave velocity is closely related to the S-wave velocity (Xia et al., 1999); thus, I inferred that the seismic velocity variation estimated in this study (Fig. 4.3) was induced mainly by the S-wave velocity variation.

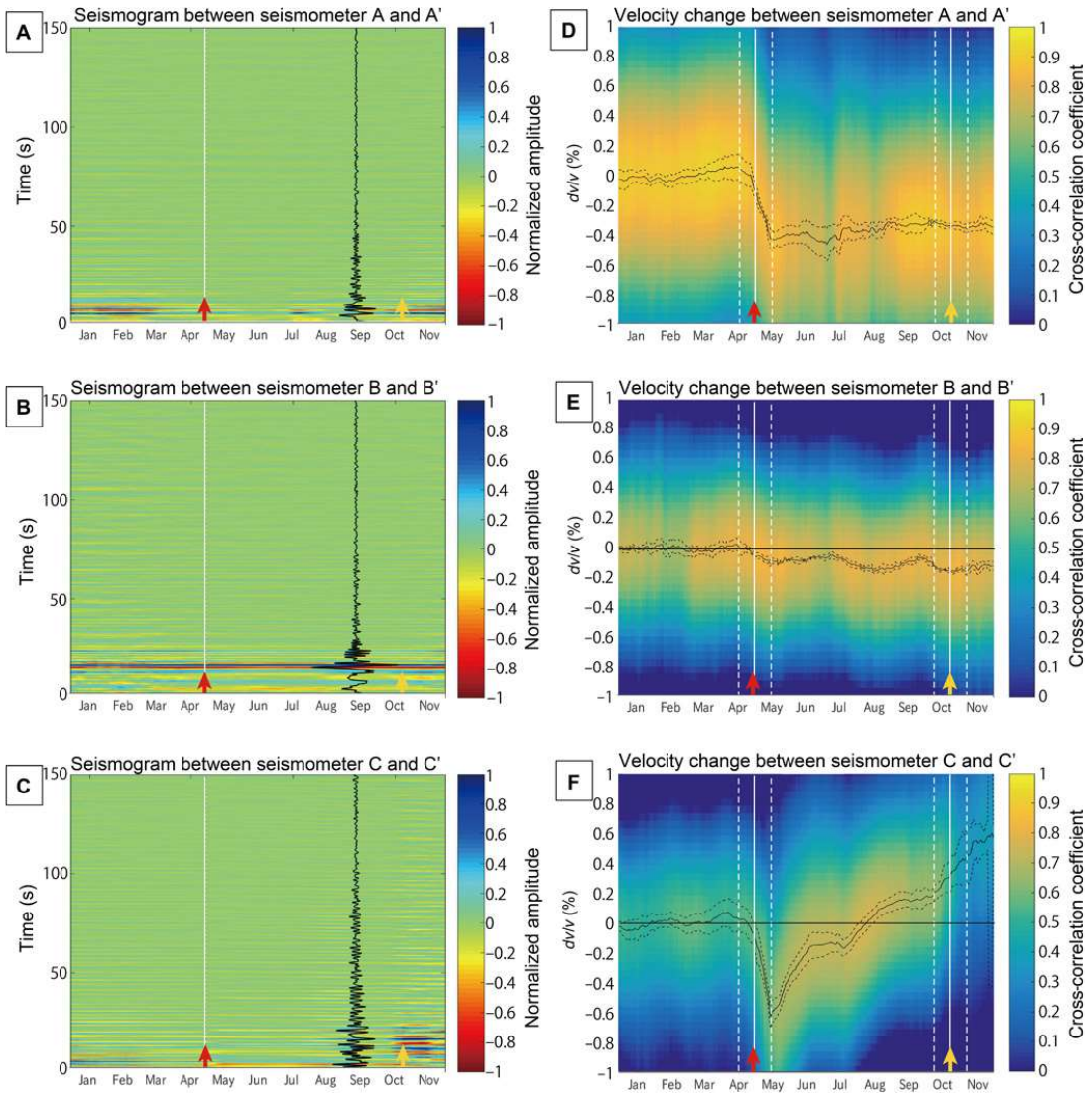

Figure 4.3. *Temporal variation of seismic traces and velocity between three seismometer pairs. (A to C) Typical seismic traces (cross-correlations) between seismometer pairs: (A) across the fault plane from A to A' in Fig. 4.1, (B) far from the fault (from B to B' in Fig. 4.1), and (C) across Mount Aso (magmatic body; from C to C' in Fig. 4.1). The vertical axis shows travel time in seconds, and the horizontal axis shows dates from December 2015 to November 2016. The red arrows indicate the date of the mainshock and volcanic eruption (16 April), and the yellow arrows indicate the date of the large eruption of the Aso volcano (7 and 8 October). (D to F) Typical seismic velocity variation between station pairs derived from the seismic traces displayed in (A) to (C). Background color indicates the cross-correlation coefficient obtained by trace stretching; black curves show daily variations of the estimated velocity changes (dvv)(dvv) with respect to changes before the Kumamoto earthquake, defined at the maximum value of the coefficient; and dashed black curves indicate the SD of the velocity change estimation. White dashed lines show the time window (30 days) influenced by the mainshock and the largest eruption.*

To measure the seismic velocity change associated with the 2016 Kumamoto earthquake, I determined velocity changes relative to the averaged change over 4 months before the mainshock (dvv d v v ; Fig. 4.3, D to F, and Figs. 4.5 and 4.8). To stabilize the results, I estimated the daily variation of the velocity change by moving the 30-day window. Although the temporal resolution of our estimated velocity variation is not high enough to correlate the variation with minor events (for example, small aftershocks), we were able to identify the first-order dynamic variation (for example, pressure variation) of the seismogenic faults and volcano during the entire earthquake sequence. Because the surface wave velocity has dispersion characteristics, the depth sensitivity is related to the frequency range of the analyzed ambient noise (Fig. 4.7). Our results using the frequency range of 0.1 to 0.9 Hz were sensitive to S-wave velocity variations from the surface to a depth of ~10 km. Using the velocity changes measured between all pairs of stations with an interstation distance of <40 km (Fig. 4.5), I mapped seismic velocity changes in the area around the seismogenic faults and Aso volcano, central Kyushu Island (Fig. 4.6) (Brenguier et al., 2014).

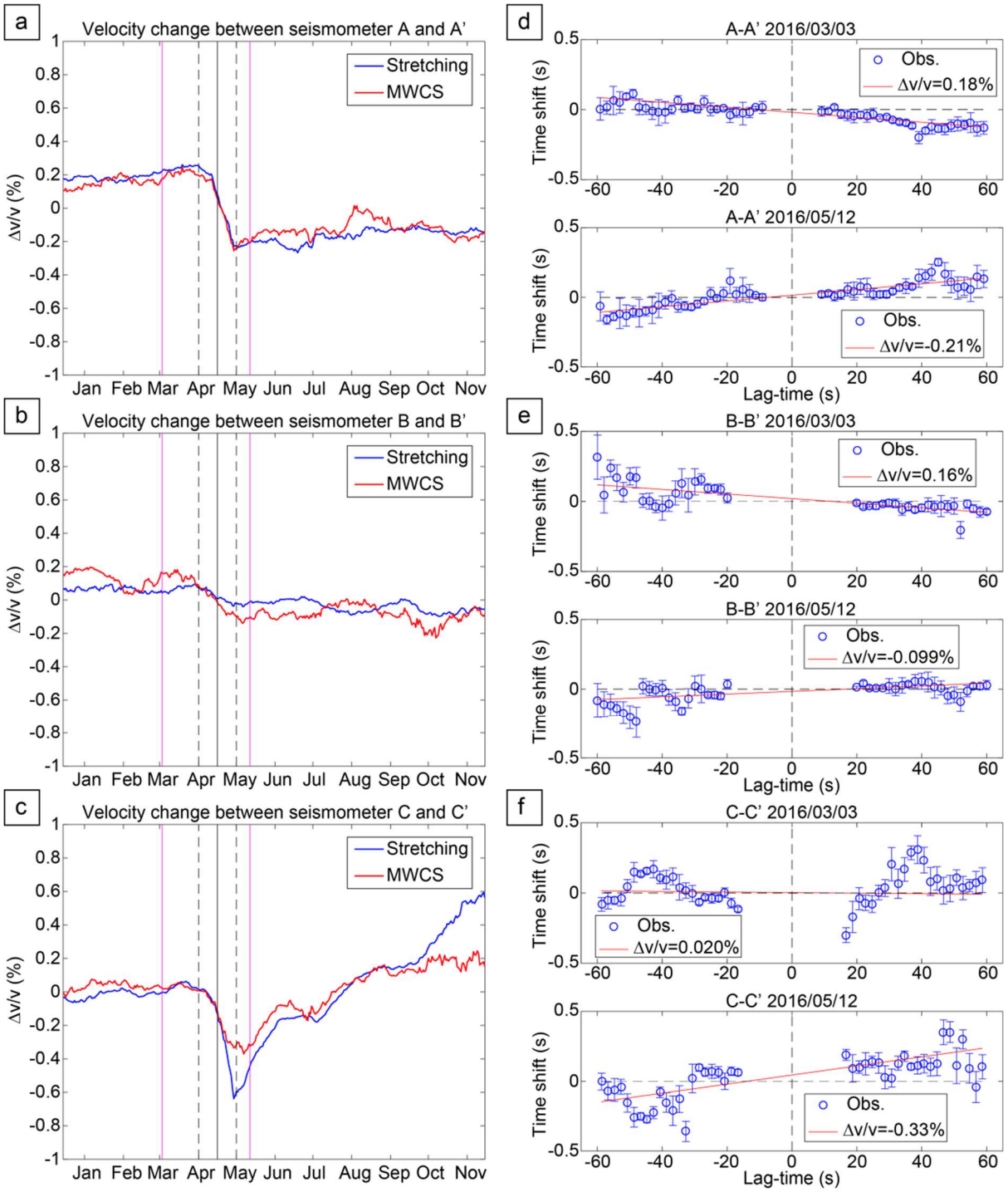

Figure 4.4. *Comparison of temporal seismic velocity changes derived from the stretching interpolation and the MWCS. (a)-(c) Temporal velocity change between three-receiver pairs by the stretching interpolation (blue) and the MWCS (red): (a) across the fault plane from A to A' in Fig. 4.1, (b) far from the fault (from B to B' in Fig. 4.1), and (c) across Mount Aso (magmatic body; from C to C' in Fig. 4.1). Vertical black dashed lines show the time window (30 days) influenced by the mainshock. (d)- (f) Time shift at each lag time measured by the MWCS on two days indicated by vertical magenta lines in panels (a)-(c). Direct waves from Aso are dominant in negative-lag time. In this figure, I did not subtract averaged velocity*

variations before the earthquake (ε_0 in equation 4.4) to remove possible shifts in velocity variations between the stretching interpolation and the MWCS.

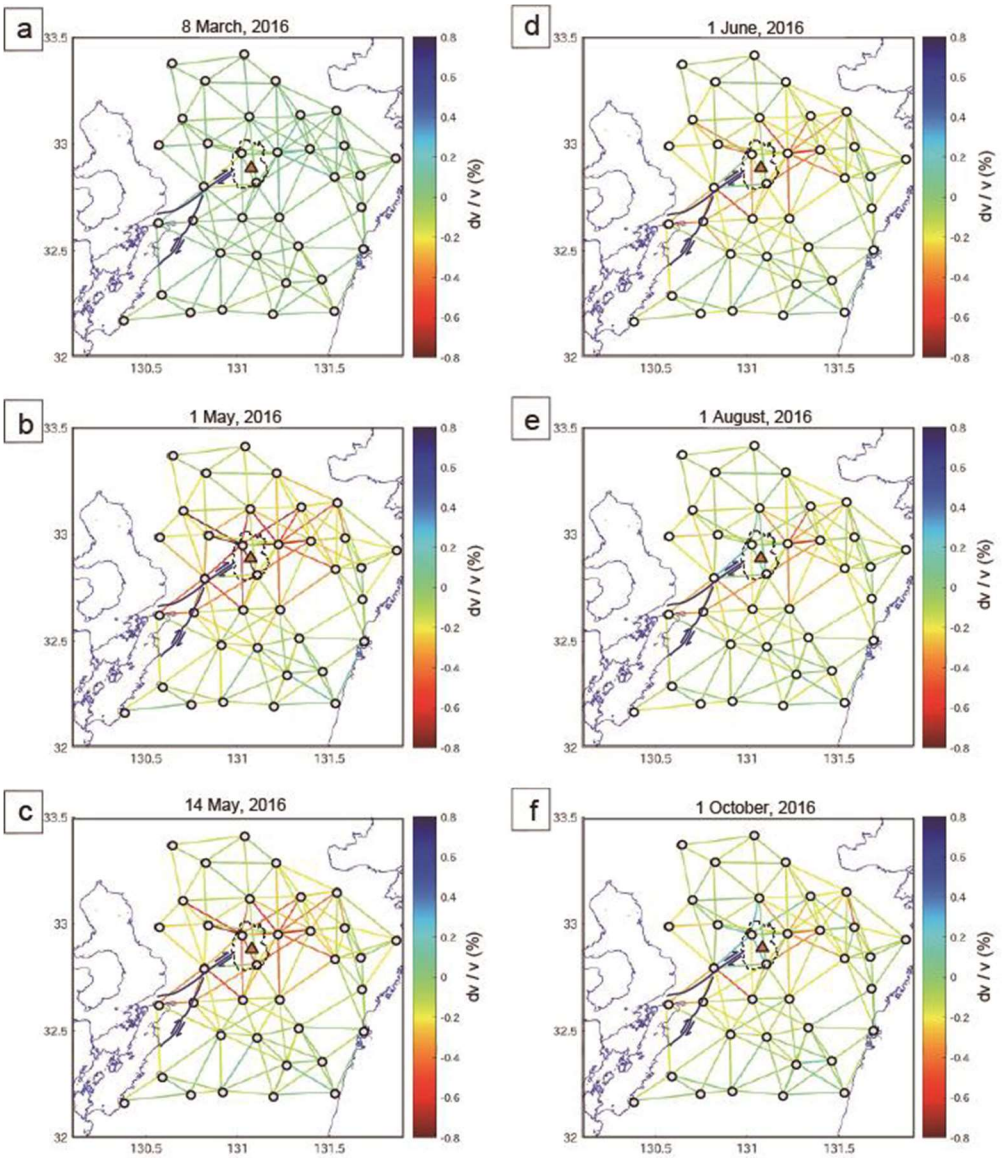

Figure 4.5. *Spatial and temporal variation of seismic velocity in central Kyushu during the 2016 Kumamoto earthquake. The seismic velocity changes* $\frac{\Delta v}{v}$ *between station pairs in each time window (30 days) relative to the averaged pre-earthquake value are displayed. The changes on a central date in each time window are displayed: (a) 8 March, (b) 1 May, (c) 14 May, (d) 1 June, (e) 1 August, and (f) 1 October, 2016. Dots are Hi-net stations.*

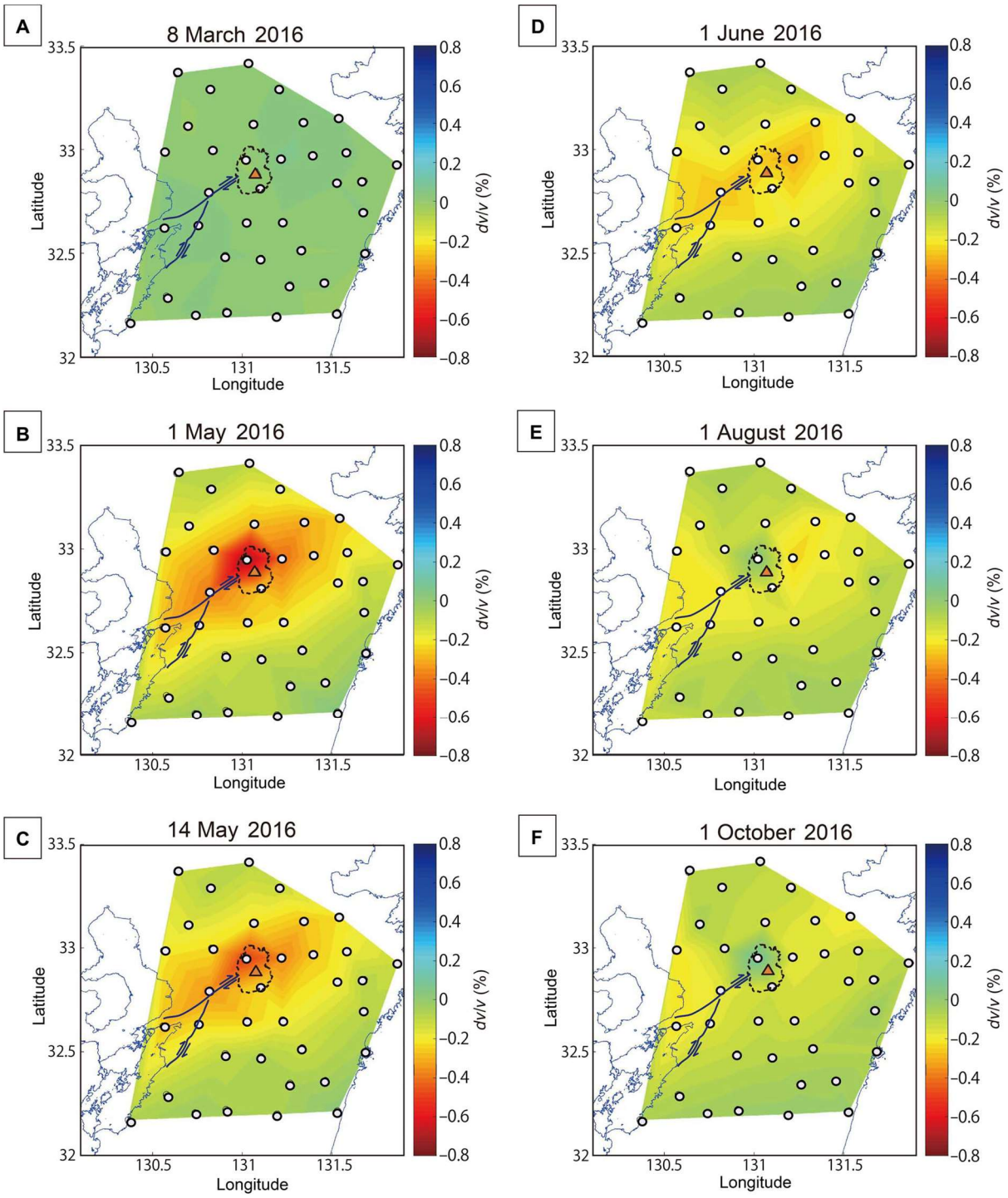

Figure 4.6. *Spatial and temporal variation of seismic velocity in central Kyushu during the 2016 Kumamoto earthquake. The surface wave velocity changes* $\frac{\Delta v}{v}$ *within each time window (30 days) relative to the averaged pre-earthquake value are displayed. Each panel shows the central date within the 30-day window: (A) 8 March 2016, (B) 1 May 2016, (C) 14 May 2016,*

(D) 1 June 2016, (E) 1 August 2016, and (F) 1 October, 2016. Warm colors indicate regions where seismic velocity was decreased. White dots are Hi-net stations.

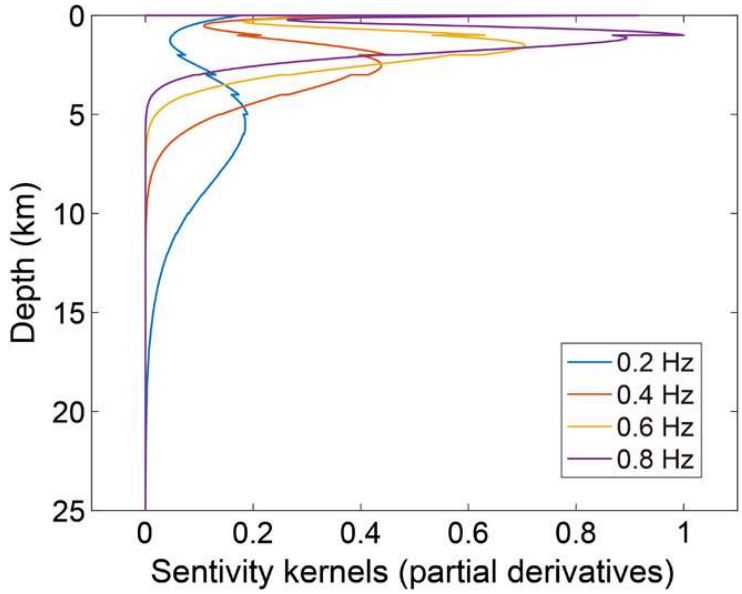

Figure 4.7. *Depth-dependent S-wave sensitivity kernels (partial derivatives) for fundamental mode Rayleigh waves with respect to S-wave velocity, which constitute a proxy for depth resolution. The sensitivity kernels were computed by using the DISPER 80 program (Saito, 1988) for a one-dimensional (1D) layered model near the Aso volcano estimated by Nishida et al. (2008). Sensitivity kernels were normalized by the maximum amplitude at 0.8 Hz.*

4.4. Discussion

Before the 2016 Kumamoto earthquake, I could not detect large velocity variation in most central Kyushu. Small seismic velocity fluctuations detected around Mount Aso before the earthquake may have been related to volcanic activity, including a small eruption. During the 2016 earthquake, seismic velocity around the Hinagu-Futagawa fault system and Mount Aso decreased greatly (Figs. 4.3, D and F, and 4.6B). Because the depth range in which the variation of seismic velocity could be estimated (<10 km in depth) includes the depth of the fault plane with maximum slip (~5 km depth) (Yagi et al., 2016), the velocity variation could be related to fault zone damage and stress and pressure changes around the deep rupture fault. Around the Hinagu-Futagawa fault system (Fig. 4.3D), seismic velocity was reduced by 0.3 to 0.4%. This velocity reduction is similar to that observed during the 2012 Costa Rica earthquake (Mw 7.6) in a subduction zone setting (~0.6%) (Chaves & Schwartz, 2016) but is larger than the reduction during the 2004 Mw 6.0 Parkfield earthquake (<0.1%) (Brenguier et al., 2008a). These velocity reductions around the seismogenic fault also depend on the interval of

seismometer pairs. Because the interval between Hi-net seismometers displayed in Fig. 4.3D is ~20 km (Fig. 1), the seismic velocity reduction within the narrow fault damage zone may have been larger (>0.4%). Laboratory experiments that used a similar lithology (Tsuji et al., 2006) demonstrated that S-wave velocity at an effective pressure of ~50 MPa (corresponding to a depth of ~5 km) decreases by ~0.36% if the stress perturbation is ~1 MPa (Moore et al., 2017). Such a velocity reduction related to crack opening could thus account for the observed velocity reduction around the fault zone. Because seismic velocity around the stress accumulation area at the fault edge also decreased, the crack opening due to formation damage or stress perturbation (increase in pore pressure) could be a primal mechanism for the velocity reduction. Even far from the seismogenic faults and volcano, seismic velocity decreased slightly during the earthquake (Figs. 4.3E and 4.6), suggesting that pressure perturbation and surface damage due to earthquake vibration occurred widely in central Kyushu.

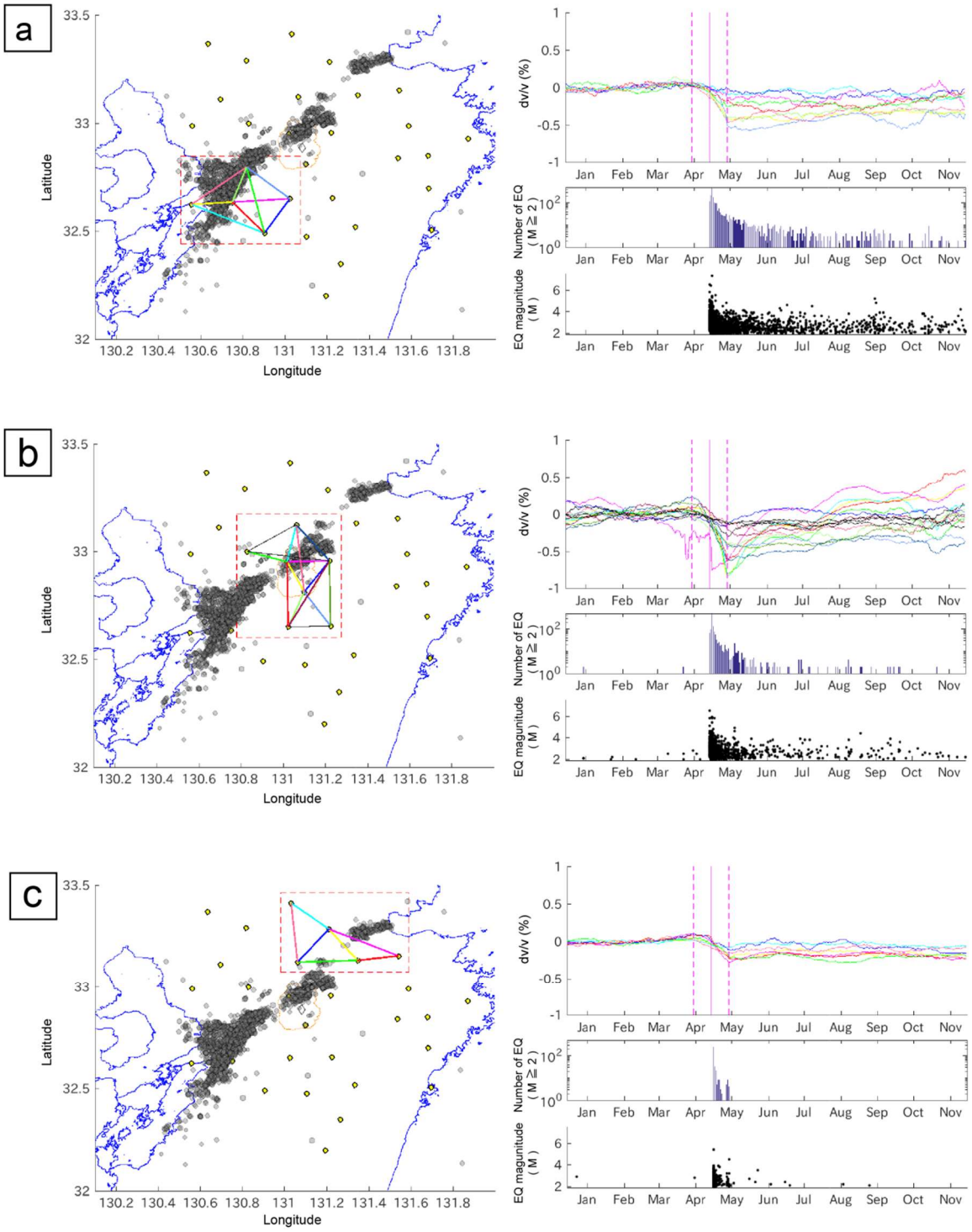
a
b
c
Latitude
Longitude
33.5
33
32.5
32
130.2 130.4 130.6 130.8 131 131.2 131.4 131.6 131.8
dv/v (%)
1
0.5
0
-0.5
-1
Jan Feb Mar Apr May Jun Jul Aug Sep Oct Nov
Number of EQ (M ≧ 2)
10^2
10^0
EQ magunitude (M)
6
4
2

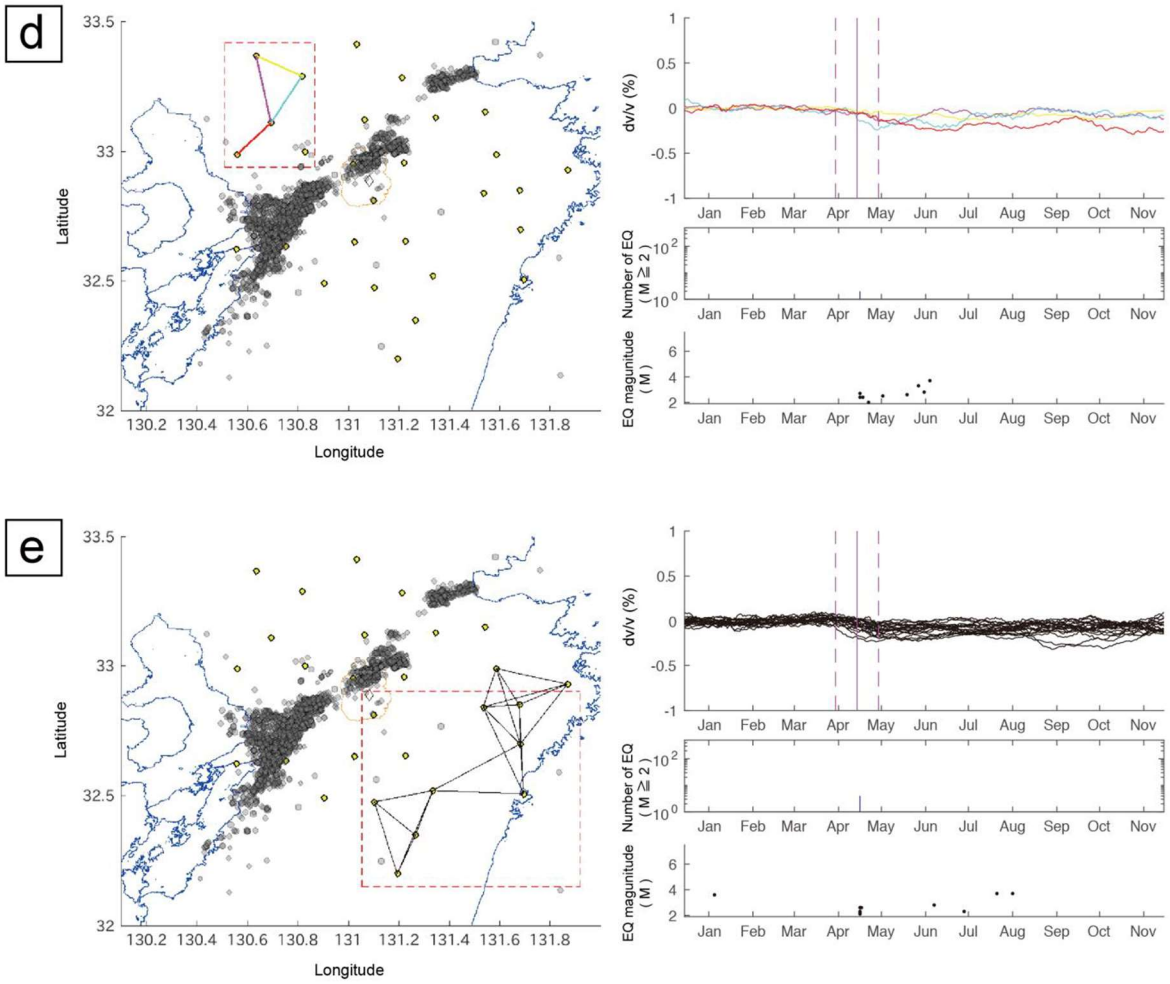

Figure 4.8. *Temporal variation of seismic velocity between each receiver pair in relation to earthquake activity. (a) (left) Hi-net stations located around the faults (yellow circles) and earthquake hypocenters (gray circles). I show data only for earthquakes with magnitude > 2. (top right) Temporal variation of seismic velocity between the receiver pairs is shown in the left panel. The color of each line shows data for the receiver pair connected with a line of the same color in the left panel. The vertical solid and dashed magenta lines show the time of the mainshock and the time window (30 days) influenced by the mainshock, respectively. (middle right) A number of earthquakes occur in the red dashed rectangle area in the left panel each day, and (lower right) the earthquake magnitudes. (b)–(e) same as panel (a), but around (b) Aso volcano and on the (c) northeastern, (d) northwestern, and (e) southern and southeastern sides of Aso. In panel (e), I did not clarify the seismometer pairs because of the large number of pairs.*

After the 2016 Kumamoto earthquake (from mid-April to November), seismic velocity changes around the Hinagu-Futagawa fault system reflected gradual healing (Fig. 4.6,

C to F). Open cracks temporarily generated in the fault zone by the earthquake could have been closed by several mechanisms, allowing seismic velocity to recover (Li et al., 2006; Wu et al., 2016). The short-term velocity recovery could be explained by crack closing due to a reduction in pore pressure. However, healing was not complete in most areas around the seismogenic faults, and the pre-earthquake state was not attained during our observation period (7 months after the earthquake; Fig. 4.3D). Such a longer-term velocity reduction around the seismogenic faults could be caused by stress change or damages related to fault displacement. Seismic velocity temporarily decreased even after the earthquake, suggesting that aftershocks continued to generate fault zone damage and stress state changes. Especially the seismic velocity at the eastern and western edges of the Hinagu-Futagawa fault system, where the aftershocks were concentrated (Asano & Iwata, 2016; Geospatial Information Authority of Japan; Kato et al., 2016; Yagi et al., 2016), did not recover (Fig. 4.8), and the seismic velocity in these areas continued to fluctuate several months after the mainshock (September to November 2016). Far from the seismogenic faults and the volcano (Fig. 4.3E), seismic velocity slightly decreased or fluctuated after the earthquake, possibly owing to temporal formation weakening in a wide area (>50 km from the faults and volcano), such as pore pressure increase due to vibration. Although several mechanisms influence the velocity recovering process, the spatiotemporal variation of seismic velocity estimated in this study could be important information for estimating fault strength recovery processes and future earthquake activity.

The largest seismic velocity reduction (0.7 to 0.8%), which occurred soon after the 2016 earthquake (Figs. 4.3F and 4.6B), was observed in the western part of the Aso caldera, where there is a magmatic body at a depth of <10 km (Miyakawa et al., 2016). The large velocity reductions were observed at several receiver pairs across the Aso magmatic body (Fig. 4.8B). During the 2011 Tohoku-oki earthquake, similar seismic velocity reduction was also observed in a volcanic area far from the seismogenic fault (Brenguier et al., 2014). The earthquake shaking could mobilize fluids around the magmatic body, and this fluid could inflate the shallower formation and open cracks. Under high pore pressure conditions around a magmatic body, seismic velocity is sensitive to stress or pore pressure changes because thin cracks are easily generated (Toksöz et al., 1976; Tsuji et al., 2008). The stress perturbation around the magmatic body during the 2016 earthquake was estimated to be ~1.8 MPa (Ozawa et al., 2016), and these stress changes are sufficient to open a preexisting crack (Walter, 2007). Open cracks generated around the magma chamber by the 2016 earthquake caused the seismic velocity to decrease greatly. Although it is possible that strong earthquake shaking weakened the volcanic body without fluid pressure, rapid velocity recovering in the Mount Aso area (Fig. 4.3F) could demonstrate that the velocity reduction is mainly associated with fluid pressure.

Seismic velocity at the Aso caldera recovered rapidly and was faster than the pre-earthquake velocity after July 2016 (Figs. 4.3F and 4.6, E and F). High volcanic activity after

the earthquake, including eruptions on 16 April and 1 May, 2016, may have caused depressurization, leading to the increased seismic velocity, a phenomenon observed at other volcanoes (Brenguier et al., 2016). Furthermore, seismic velocity around the Aso caldera again increased greatly after the large eruption on 7 and 8 October (Fig. 4.3F).

To reveal the vertical velocity change (that is, the change with depth), I calculated the temporal velocity variations in different frequency ranges for two seismometer pairs (Fig. 4.9): (i) one across the seismogenic Futagawa fault (A-A′ station pair) and (ii) the other across the Aso caldera (C-C′ station pair). The frequency dependence displayed by these two seismometer pairs had different characteristics. As the frequency became higher, the changes in seismic velocity across the seismogenic fault became greater (Fig. 4.9A), characteristics similar to those reported across the fault of the Mw 6.0 Parkfield earthquake (Wu et al., 2016). This result suggests that the damage was intensive around the fault zone from the surface to the depth of the largest fault rupture at ~5 km. In contrast, the seismic velocity variations around the Aso caldera were similar in both low-frequency (0.1 to 0.6 Hz) and high-frequency (0.4 to 0.9 Hz) ranges (Fig. 4.9B). A similar trend was observed in the case of the Mw 6.5 San Simeon earthquake (Wu et al., 2016). This result indicates that the depth range of the velocity change was deeper at the Aso caldera than in the fault zone. If S-wave velocity at the Aso caldera decreased only at shallower depths (<5 km), then the resulting velocity variation in the lower frequency range would be smaller than that in the higher frequency range because Rayleigh waves at low frequencies have low sensitivity at a shallower depth (Fig. 4.7). Therefore, S-wave velocity should decrease at depths of about 3 to 10 km, where lower frequency Rayleigh waves have larger sensitivity (Fig. 4.7). Because this depth range roughly agrees with the location of the magma chamber (Miyakawa et al., 2016), the seismic velocity may have been reduced around the magma chamber during the earthquake. Another possible cause of the velocity variation in the volcanic area is rainfall (Sens-Schönfelder & Wegler, 2006). However, the seismic velocity indicated by the higher frequency component, which reflects velocity at shallow depth, in the Mount Aso area did not show any clear effect that could be attributed to precipitation (C-C′ station pair; Fig. 4.9B). I, therefore, concluded that the seismic velocity variation revealed in this study (Figs. 4.3 and 4.6) was not greatly influenced by rainfall.

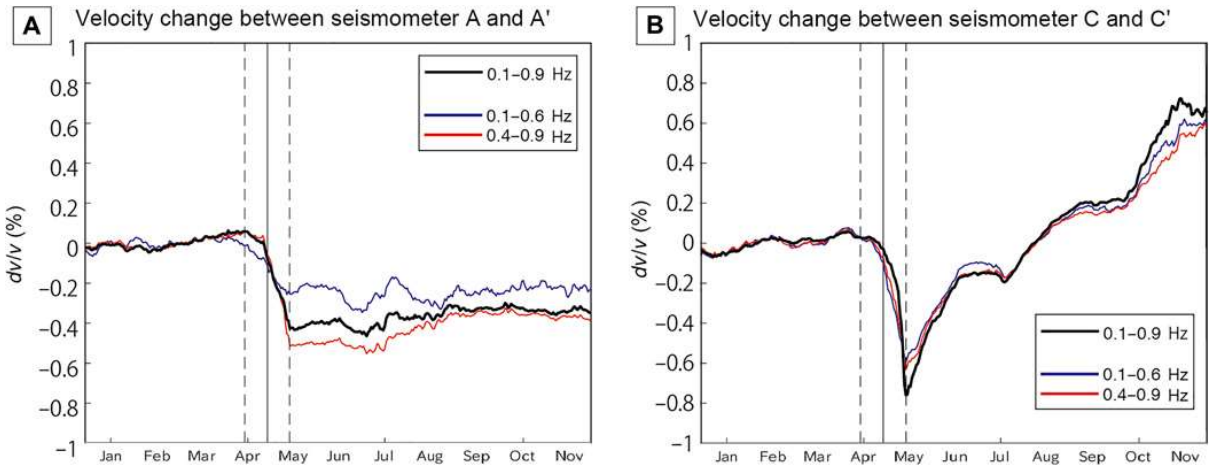

Figure 4.9. *Frequency dependence of temporal variations of seismic velocity between two typical seismometer pairs. (A) Across the fault plane from A to A' in Fig. 4.1. (B) Across Mount Aso from C to C' in Fig. 4.1. Curves show daily variations of the estimated velocity change* $\frac{\Delta v}{v}$ *with respect to changes before the Kumamoto earthquake. Vertical dashed lines show the time window (30 days) influenced by the mainshock. The frequency-dependent velocity variation is likely associated with surface wave dispersion (Wu et al., 2016), supporting our assumption that the coda waves were dominated by surface waves.*

4.5. Conclusion

Here, I report mapping results showing the continuous temporal variation in seismic velocity across the fault and volcano during the Kumamoto earthquake. Past studies have used similar approaches for velocity estimation, but the higher spatial resolution of our estimated seismic velocity variation in a broad area allowed us to identify the spatial distribution of the damage zone or stress state. This approach can be applied anywhere permanent seismometers are deployed, such as Hi-net in the Japanese islands (Okada et al., 2004) and arrays in the United States (Bensen et al., 2008). Velocity changes due to slow slip or foreshocks identified through this crustal-scale monitoring could thus be used to estimate future earthquakes. The denser deployment of seismometers around fault zones and volcanoes (Obermann et al., 2013) would allow local anomalies related to earthquake and volcanic activities to be accurately resolved.

References

Asano, K. & Iwata, T., Source rupture processes of the foreshock and mainshock in the 2016 Kumamoto earthquake sequence estimated from the kinematic waveform inversion of strong motion data. Earth Planets Space 68, 147 (2016).

Bensen, G. D., Ritzwoller, M. H. & Shapiro, N. M., Broadband ambient noise surface wave tomography across the United States. J. Geophys. Res. 113, B05306 (2008).

Bensen, G. D., Ritzwoller, M. H., Barmin, M. P., Levshin, A. L., Lin, F., Moschetti, M. P., Shapiro, N. M. & Yang, Y., Processing seismic ambient noise data to obtain reliable broad-band surface wave dispersion measurements. Geophys. J. Int. 169, 1239–1260 (2007).

Brenguier, F., Campillo, M., Hadziioannou, C., Shapiro, N. M., Nadeau, R. M. & Larose, E., Postseismic relaxation along the San Andreas fault at Parkfield from continuous seismological observations. Science 321, 1478–1481 (2008).

Brenguier, F., Campillo, M., Takeda, T., Aoki, T., Shapiro, N. M., Briand, X., Emoto, K. & Miyake, H., Mapping pressurized volcanic fluids from induced crustal seismic velocity drops. Science 345, 80–82 (2014).

Brenguier, F., Rivet, D., Obermann, A., Nakata, N., Boué, P., Lecocq, T., Campillo, M. & Shapiro, N., 4-D noise-based seismology at volcanoes: Ongoing efforts and perspectives. J. Volcanol. Geotherm. Res. 321, 182–195 (2016).

Brenguier, F., Shapiro, N. M., Campillo, M., Ferrazzini, V., Dupute, Z., Coutant, O., & Nercessian, A., Towards forecasting volcanic eruptions using seismic noise. Nat. Geosci. 1, 126–130 (2008).

Budi-Santoso, A. & Lesage, P., Velocity variations associated with the large 2010 eruption of Merapi volcano, Java, retrieved from seismic multiplets and ambient noise cross-correlation. Geophys. J. Int. 206, 221–240 (2016).

Chaves, E. J. & Schwartz, S. Y., Monitoring transient changes within overpressured regions of subduction zones using ambient seismic noise. Sci. Adv. 2, e1501289 (2016).

Clarke, D., Zaccarelli, L., Shapiro, N. M. & Brenguier, F., Assessment of resolution and accuracy of the Moving Window Cross Spectral technique for monitoring crustal temporal variations using ambient seismic noise. Geophys. J. Int. 186, 867–882 (2011).

Colombi, A., Chaput, J., Brenguier, F., Hillers, G., Roux, P. & Campillo, M., On the temporal stability of the coda of ambient noise correlations. C. R. Geosci. 346, 307–316 (2014).

Derode, A., Larose, E., Campillo, M. & Fink, M., How to estimate the Green's function of a heterogeneous medium between two passive sensors? Application to acoustic waves. Appl. Phys. Lett. 83, 3054–3056 (2003).

Geospatial information authority of Japan, coseismic fault model in the 2016 Kumamoto earthquake (geospatial information authority of Japan, 2016); www.gsi.go.jp/common/ 000140781.pdf.

Hadziioannou, C., Larose, E., Baig, A., Roux, P. & Campillo, M., Improving temporal resolution in ambient noise monitoring of seismic wave speed. J. Geophys. Res. 116, B07304 (2011).

Hadziioannou, C., Larose, E., Coutant, O., Roux, P. & Campillo, M., Stability of monitoring weak changes in multiply scattering media with ambient noise correlation: Laboratory experiments. J. Acoust. Soc. Am. 125, 3688–3695 (2009).

Hotovec-Ellis, A. J., Gomberg, J., Vidale, J. E. & Creager, K. C., A continuous record of intereruption velocity change at Mount St. Helens from coda wave interferometry. J. Geophys. Res. 119, 2199–2214 (2014).

Kato, A., Fukuda, J., Nakagawa, S. & Obara, K., Foreshock migration preceding the 2016 Mw 7.0 Kumamoto earthquake, Japan. Geophys. Res. Lett. 43, 8945–8953 (2016).

Kawakatsu, H., Kaneshima, S., Matsubayashi, H., Ohminato, T., Sudo, Y., Tsutsui, T., Uhira, K., Yamasato, H., Ito, H. & Legrand, D., Aso94: Aso seismic observation with broadband instruments. J. Volcanol. Geotherm. Res. 101, 129–154 (2000).

Li, Y.-G., Chen, P., Cochran, E. S., Vidale, J. E. & Burdette, T., Seismic evidence for rock damage and healing on the San Andreas fault associated with the 2004 M 6.0 Parkfield earthquake. Bull. Seismol. Soc. Am. 96, S349–S363 (2006).

Matsumoto, S., Nakao, S., Ohkura, T., Miyazaki, M., Shimizu, H., Abe, Y., Inoue, H., Nakamoto, M., Yoshikawa, S. & Yamashita, Y., Spatial heterogeneities in tectonic stress in Kyushu, Japan and their relation to a major shear zone. Earth Planets Space 67, 172 (2015).

Meier, U., Shapiro, N. M. & Brenguier, F., Detecting seasonal variations in seismic velocities within Los Angeles Basin from correlations of ambient seismic noise. Geophys. J. Int. 181, 985–996 (2010).

Minato, S., Tsuji, T., Ohmi, S. & Matsuoka, T., Monitoring seismic velocity change caused by the 2011 Tohoku-oki earthquake using ambient noise records. Geophys. Res. Lett. 39, L09309 (2012).

Miyakawa, A., Sumita, T., Okubo, Y., Okuwaki, R., Otsubo, M., Uesawa, S. & Yagi, Y., Volcanic magma reservoir imaged as a low-density body beneath Aso volcano that terminated the 2016 Kumamoto earthquake rupture. Earth Planets Space 68, 208 (2016).

Moore, J. D. P., Yu, H., Tang, C.-H., Wang, T., Barbot, S., Peng, D., Masuti, S., Dauwels, J., Hsu, Y.-J., Lambert, V., Nanjundiah, P., Wei, S., Lindsey, E., Feng, L. & Shibazaki, B., Imaging the distribution of transient viscosity after the 2016 Mw 7.1 Kumamoto earthquake. Science 356, 163–167 (2017).

Nakata, N. & Snieder, R., Near-surface weakening in Japan after the 2011 Tohoku-Oki earthquake. Geophys. Res. Lett. 38, L17302 (2011).

Nakata, N., Chang, J. P., Lawrence, J. F. & Boué, P., Body wave extraction and tomography at Long Beach, California, with ambient-noise interferometry. J. Geophys. Res. 120, 1159–1173 (2015).

Nakata, N., Snieder, R., Tsuji, T., Larner, K. & Matsuoka, T., Shear wave imaging from traffic noise using seismic interferometry by cross-coherence. Geophysics 76, SA97–SA106 (2011).

Nishida, K., Kawakatsu, H. & Obara, K., Three-dimensional crustal S wave velocity structure in Japan using microseismic data recorded by Hi-net tiltmeters. J. Geophys. Res. 113, B10302 (2008).

Nishimura, T., Uchida, N., Sato, H., Ohtake, M., Tanaka, S. & Hamaguchi, H., Temporal changes of the crustal structure associated with the M6.1 earthquake on September 3, 1998, and the volcanic activity of Mount Iwate, Japan. Geophys. Res. Lett. 27, 269–272 (2000).

Niu, F., Silver, P. G., Daley, T. M., Cheng, X. & Majer, E. L., Preseismic velocity changes observed from active source monitoring at the Parkfield SAFOD drill site. Nature 454,204–208 (2008).

Obermann, A., Froment, B., Campillo, M., Larose, E., Planès, T., Valette, B., Chen, J. H. & Liu, Q. Y., Seismic noise correlations to image structural and mechanical changes associated with the M w 7.9 2008 Wenchuan earthquake. J. Geophys. Res. 119, 3155–3168 (2014).

Obermann, A., Kraft, T., Larose, E. & Wiemer, S., Potential of ambient seismic noise techniques to monitor the St. Gallen geothermal site (Switzerland). J. Geophys. Res. 120, 4301–4316 (2015).

Obermann, A., Planès, T., Larose, E. & Campillo, M., Imaging preeruptive and coeruptive structural and mechanical changes of a volcano with ambient seismic noise. J. Geophys. Res. 118, 6285–6294 (2013).

Okada, Y., Kasahara, K., Hori, S., Obara, K., Sekiguchi, S., Fujiwara, H. & Yamamoto, A., Recent progress of seismic observation networks in Japan—Hi-net, F-net, K-NET and KiK-net. Earth Planets Space 56, xv–xxviii (2004).

Ozawa, T., Fujita, E. & Ueda, H., Crustal deformation associated with the 2016 Kumamoto Earthquake and its effect on the magma system of Aso volcano. Earth Planets Space 68, 186 (2016).

Poupinet, G., Ellsworth, W. L. & Frechet, J., Monitoring velocity variations in the crust using earthquake doublets: An application to the Calaveras Fault, California. J. Geophys. Res. 89, 5719–5731 (1984).

Saito, M., DISPER 80: A subroutine package for the calculation of seismic normal mode solution, in Seismological Algorithms, D. J. Doornbos, Ed. (Academic Press Limited, 1988).

Sassa, K., Volcanic micro-tremors and eruption-earthquakes. Mem. Coll. Sci. Kyoto Univ. Ser. A 18, 255–293 (1935).

Seats, K. J., Lawrence, J. F. & Prieto, G. A., Improved ambient noise correlation functions using Welch's method. Geophys. J. Int. 118, 513–523 (2012).

Sens-Schönfelder, C. & Wegler, U., Passive image interferometry and seasonal variations of seismic velocities at Merapi Volcano, Indonesia. Geophys. Res. Lett. 33, L21302 (2006).

Takeuchi, H. & Saito, M., Seismic surface waves. Methods Comput. Phys. 11, 217–295 (1972).

Toksöz, M. N., Cheng, C. H. & Timur, A., Velocities of seismic waves in porous rocks. Geophysics 41, 621–645 (1976).

Tsuji, T., Kimura, G., Okamoto, S., Kono, F., Mochinaga, H., Saeki, T. & Tokuyama, H., Modern and ancient seismogenic out-of-sequence thrusts in the Nankai accretionary prism: Comparison of laboratory-derived physical properties and seismic reflection data. Geophys. Res. Lett. 33, L18309 (2006).

Tsuji, T., Tokuyama, H., Pisani, P. C. & Moore, G., Effective stress and pore pressure in the Nankai accretionary prism off the Muroto Peninsula, southwestern Japan. J. Geophys. Res. 113, B11401 (2008).

Vidale, J. E. & Li, Y.-G., Damage to the shallow Landers fault from the nearby Hector Mine earthquake. Nature 421, 524–526 (2003).

Walter, T. R., How a tectonic earthquake may wake up volcanoes: Stress transfer during the 1996 earthquake–eruption sequence at the Karymsky Volcanic Group, Kamchatka. Earth Planet. Sci. Lett. 264, 347–359 (2007).

Wapenaar, K. & Fokkema, J., Green's function representations for seismic interferometry. Geophysics 71, SI33–SI46 (2006).

Wegler, U. & Sens-Schönfelder, C., Fault zone monitoring with passive image interferometry. Geophys. J. Int. 168, 1029–1033 (2007).

Wessel, P. & Smith, W. H. F., New, improved version of generic mapping tools released. Eos Trans. Am. Geophys. Union 79, 579 (1998).

Wu, C., Delorey, A., Brenguier, F., Hadziioannou, C., Daub, E. G. & Johnson, P., Constraining depth range of S wave velocity decrease after large earthquakes near Parkfield, California. Geophys. Res. Lett. 43, 6129–6136 (2016).

Xia, J., Miller, R. D. & Park, C. B., Estimation of near-surface shear-wave velocity by inversion of Rayleigh waves. Geophysics 64, 691–700 (1999).

Yagi, Y., Okuwaki, R., Enescu, B., Kasahara, A., Miyakawa, A. & Otsubo, M., Rupture process of the 2016 Kumamoto earthquake in relation to the thermal structure around Aso volcano. Earth Planets Space 68, 118 (2016).

Zhan, Z., Tsai, V. C. & Clayton, R. W., Spurious velocity changes caused by temporal variations in ambient noise frequency content. Geophys. J. Int. 194, 1574–1581 (2013).

Chapter 5

Temporal changes in anthropogenic seismic noise levels associated with economic and leisure activities during the COVID-19 pandemic

Abstract

Seismic ambient noise with frequencies >1 Hz includes noise related to human activities. A reduction in seismic noise during the COVID-19 pandemic has been observed worldwide, as restrictions were imposed to control outbreaks of the SARS-CoV-2 virus. In this context, I studied the effect of changes in anthropogenic activities during COVID-19 on the seismic noise levels in the Tokyo metropolitan area, Japan, considering the time of day, day of the week, and seasonal changes. The results showed the largest reduction in noise levels during the first state of emergency under most conditions. After the first state of emergency was lifted, the daytime noise reverted to previous levels immediately on weekdays and gradually on Sundays. That was likely because economic activities instantly resumed while non-essential outings were still mostly avoided on Sundays. Furthermore, the daytime noise level on Sundays was strongly reduced regardless of changes on weekdays after the second state of emergency, which restricted activities mainly at night. Sunday noise levels gradually increased from the middle of the second state of emergency, suggesting a gradual reduction in public concern about COVID-19 following a decrease in infections. Our findings demonstrate that seismic noise can be used to monitor social activities.

Keywords: Anthropogenic seismic noise, Monitoring, social activity, COVID-19

5.1. Introduction

Ambient seismic noise recorded by seismometers includes microseisms and anthropogenic or cultural noise. Microseisms are caused by the coupling between the ocean and the solid Earth at frequencies mostly <1 Hz (Longuet-Higgins, 1950), whereas anthropogenic seismic noise, especially in urban areas, includes seismic signals generated by human activities such as moving people and industrial activities (Díaz et al., 2017; Groos & Ritter, 2009; Larose et al., 2015; McNamara & Buland, 2004). A recent study reported an increase in ambient seismic noise in response to an increase in the gross domestic product (GDP), which is associated with the magnitude of human activity (Hong et al., 2020). Because an increase in ambient noise can be attributed to a wide range of human activities, ambient seismic noise in urban areas tends to be stronger and more complex. For instance, Díaz et al. (2017) monitored road traffic and subway trains along an avenue approximately 150 m away for frequencies >1 Hz. They succeeded in detecting signals generated by various anthropogenic noises, including not only road traffic but also rock concerts and football games. Considering the temporary absence of a specific noise source, Green et al. (2008) monitored the ambient seismic noise during a complete shutdown of the subway system during an industrial strike and found a clear reduction for frequencies >25 Hz within a distance of 100 m, but no reduction at a distance of ~600 m from the nearest subway line. Hence, ambient seismic noise includes various anthropogenic noises, depending on the frequency, time, and distance (Kuzma et al., 2009; Riahi & Gerstoft, 2015).

The outbreak of the SARS-CoV-2 virus responsible for COVID-19 has immensely impacted and restricted the routine lives of people worldwide. After the first report of COVID-19 in December 2019, it spread rapidly and exponentially around the globe, and the World Health Organization (WHO) declared it a pandemic on March 13, 2020 (Sohrabi et al., 2020). Many countries went into lockdown to contain major COVID-19 outbreaks, and daily life changed globally during the COVID-19 pandemic (Gössling et al., 2020). The large-scale restrictions on human activities during the pandemic also presented a rare opportunity to distinguish anthropogenic seismic noise from ambient seismic noise clearly. Poli et al. (2020) and Xiao et al. (2020) compared ambient seismic noise levels before and during pandemic-related lockdowns using continuous seismic records for Italy and China, respectively and observed a clear decrease in noise levels during the lockdown. Poli et al. (2020) found that the noise level was significantly reduced in the frequency band of 1–10 Hz. The decrease in noise level for China was much larger than for Italy (Xiao et al., 2020). Xiao et al. (2020) inferred that this was caused by the difference in the strictness of enforcing restrictions by the governments of the two countries. Lecocq et al. (2020) investigated noise levels worldwide. They found that the noise level in the frequency range of 4–14 Hz was sensitive to lockdowns

and was reduced by up to 50% during the lockdown. While the reduction was highest in populated areas, the seismic quiescence extended several kilometers. At the local scale, continuous fiber-optic distributed acoustic sensing recordings showed a spatial reduction in noise levels corresponding to COVID-19 responses (Lindsey et al., 2020). A 50% decrease in vehicular noise was observed in one commuter sector immediately following a stay-at-home order, even though the traffic near hospitals persisted.

Since the first case was reported on January 28, 2020, the number of confirmed cases in Japan increased, with the case curve showing several peaks. Figure 5.1 shows the number of new COVID-19 cases in Tokyo. The national and local governments took measures against the tide of COVID-19, depending on the number of new cases. The first wave started in late February 2020. To prevent the spread of infection, restrictions, such as school closures and the cancellation of public events were issued. In Tokyo, schools remained closed from March 2 to June 30, 2020 (yellow shaded area in Fig. 5.1). In response to the COVID-19 pandemic, the Japanese government declared the first state of emergency in Tokyo from April 7 to May 25, 2020 (pink shaded area in Fig. 5.1), during which many people voluntarily refrained from going out. However, trains and road traffic did not stop because economic activities continued. After the first wave, the Japanese government took measures to improve the economy, such as encouraging domestic travel. In Tokyo, based on the daily case situation, domestic travel was encouraged from October 2020; the government campaign was called “Go To Travel” (light blue shaded area in Fig. 5.1). However, these economic recovery measures were stopped on December 28 because the third wave started. Because the number of new COVID-19 cases rapidly increased in the third wave, the second state of emergency was declared from January 7 to March 21, 2021 (purple shaded area in Fig. 5.1). The second state of emergency focused on restricting activity at night.

Yabe et al. (2020) reported a reduction in seismic noise in the Tokyo metropolitan area associated with reduced social activity due to COVID-19 during the first wave. To monitor the seismic noise level, data from 18 seismic stations of the Metropolitan Seismic Observation Network (MeSO-net) for the period January 2018 to June 2020 were used. They observed a two-step seismic noise reduction. The first reduction occurred when schools were closed at frequencies mainly >20 Hz. The second reduction occurred when the first state of emergency was declared, mainly in the frequency range of 1-20 Hz, reflecting a decrease in social activities in the entire Tokyo metropolitan area (Yabe et al., 2020).

In this study, I monitored temporal changes in the seismic noise level around Tokyo one year after the outbreak of COVID-19, using data from 101 seismic stations from April 2017 to mid-March 2021. I investigated the variation in the noise level in different periods and on different days of the week in the two frequency bands in which the noise reduction was reported previously. In addition, since the estimated temporal variation in the noise level

showed clear seasonal variations, I modeled the seasonal variations by assuming a simple annual cycle based on the data of the past 2 years. I then emphasized the temporal variations in the noise level due to COVID-19 by correcting for the seasonal variations.

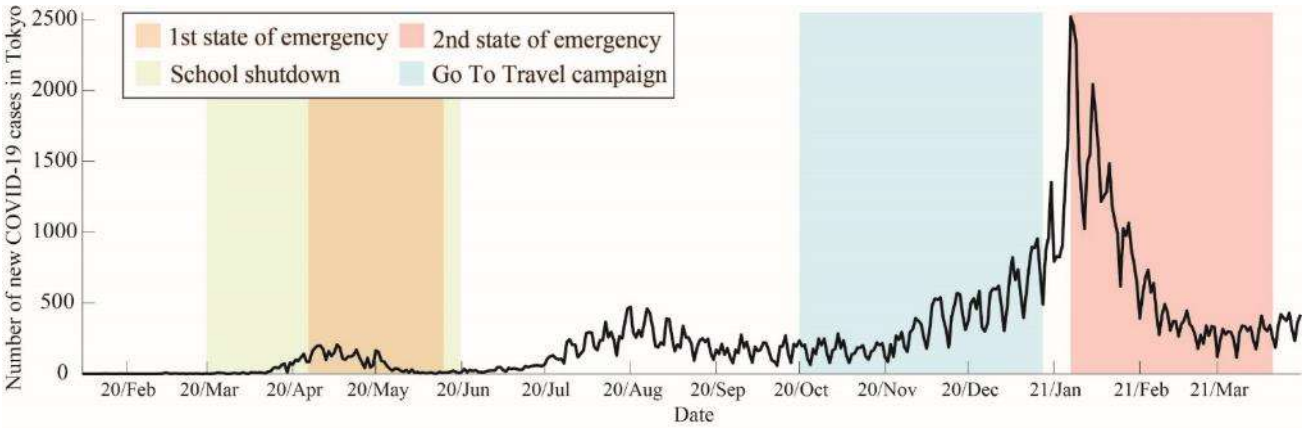

Figure 5.1. *The number of new COVID-19 cases in Tokyo. The black solid line indicates the number of new COVID-19 cases in Tokyo; the orange and pink shaded areas represent the periods of the first and second states of emergency states in Tokyo, respectively; the green shaded area represents the period of school closures; the light blue shaded area represents the period of the Go-To Travel campaign.*

5.2. Data Source and Calculation of Power Spectral Density

I used publicly available, continuous, three-component ground acceleration data recorded by the MeSO-net. The MeSO-net stations have acceleration sensors with a sampling rate of 200 Hz and are installed at depths of ~20 m to reduce the influence of anthropogenic noise (Kasahara et al., 2009; Sakai & Hirata, 2009). Approximately 300 MeSO-net stations are deployed around the metropolitan area, of which I chose 101 stations located around Tokyo (Fig. 5.2a). The vertical component of the seismic noise from April 1, 2017, to March 15, 2021, was used in this study.

To estimate the temporal change in ambient noise before and after the outbreak of COVID-19, I calculated the power spectral density (PSD) following the method of McNamara & Boaz (2019). The PSD as a function of time and frequency is an effective tool for visually distinguishing different types of seismic noise. I divided the daily data into 10-min segments and applied demean and detrend to each data segment. After applying a 50% cosine taper, I calculated the PSD for each 10-min data segment. The decrease in the amplitude value due to the taper was corrected using the coefficient $c = \sqrt{N/\sum_k^N w(k)^2}$, where N is the length of the window of the taper and $w(k)$ is the window of the taper for the kth sample. In this study, I

used the median values of the PSDs for the specific periods (e.g., all day, daytime, or night) as the daily PSDs because the mean value is easily affected by large outliers caused by earthquakes, and nearby construction, etc.

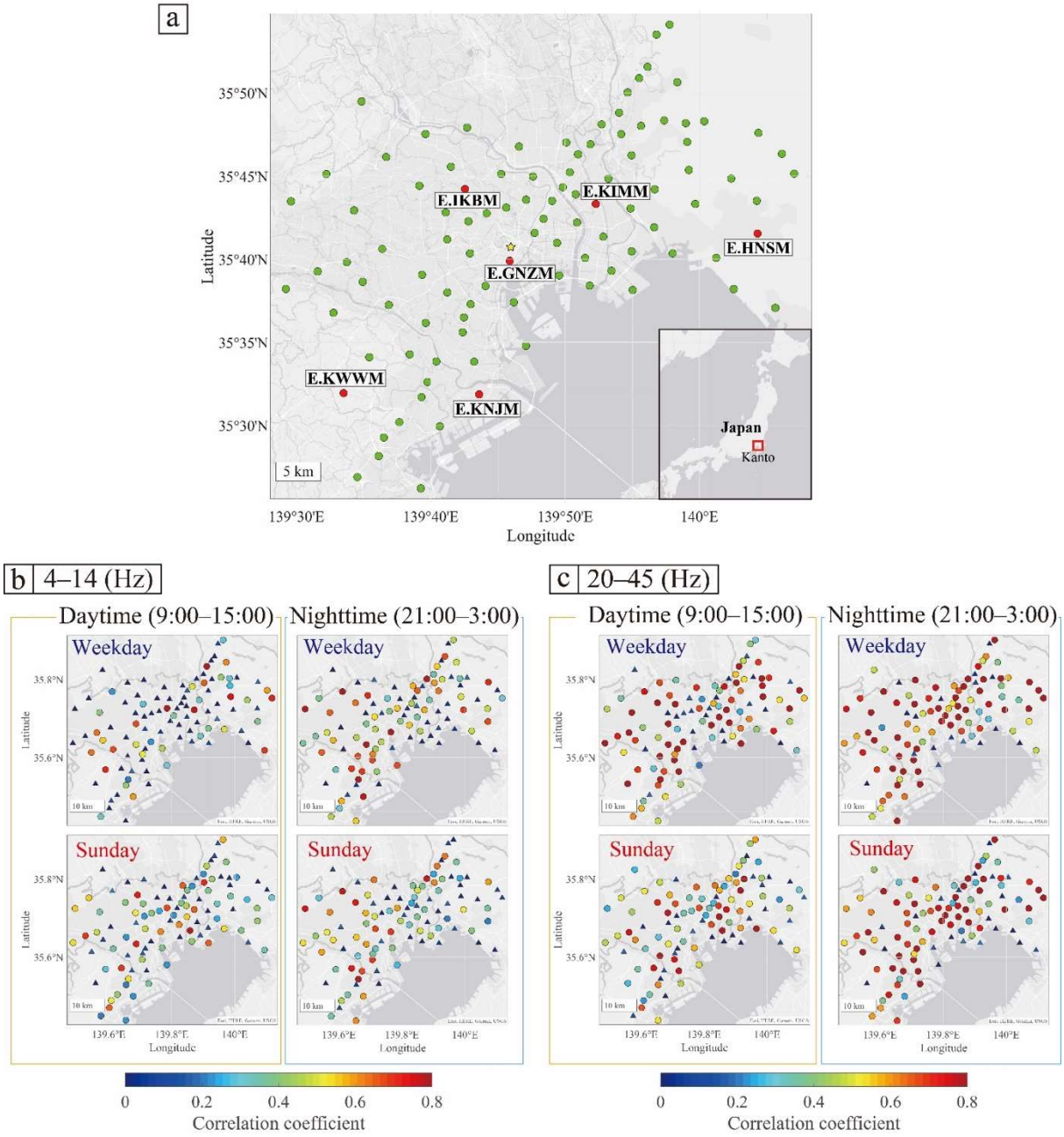

Figure 5.2. *(a) Arrangement of the MeSO-net. Red and green dots show the MeSO-net stations. The yellow star indicates the Tokyo station. (b–c) Map of correlation coefficients, which were calculated considering day and time in the frequency range of (b) 4–14 Hz and (c) 20–45 Hz. Triangles represent the stations with correlation coefficients <0.2, and circles represent the stations with correlation coefficients >0.2; the latter was used in Figures 5.6, 5.7, and 5.8.*

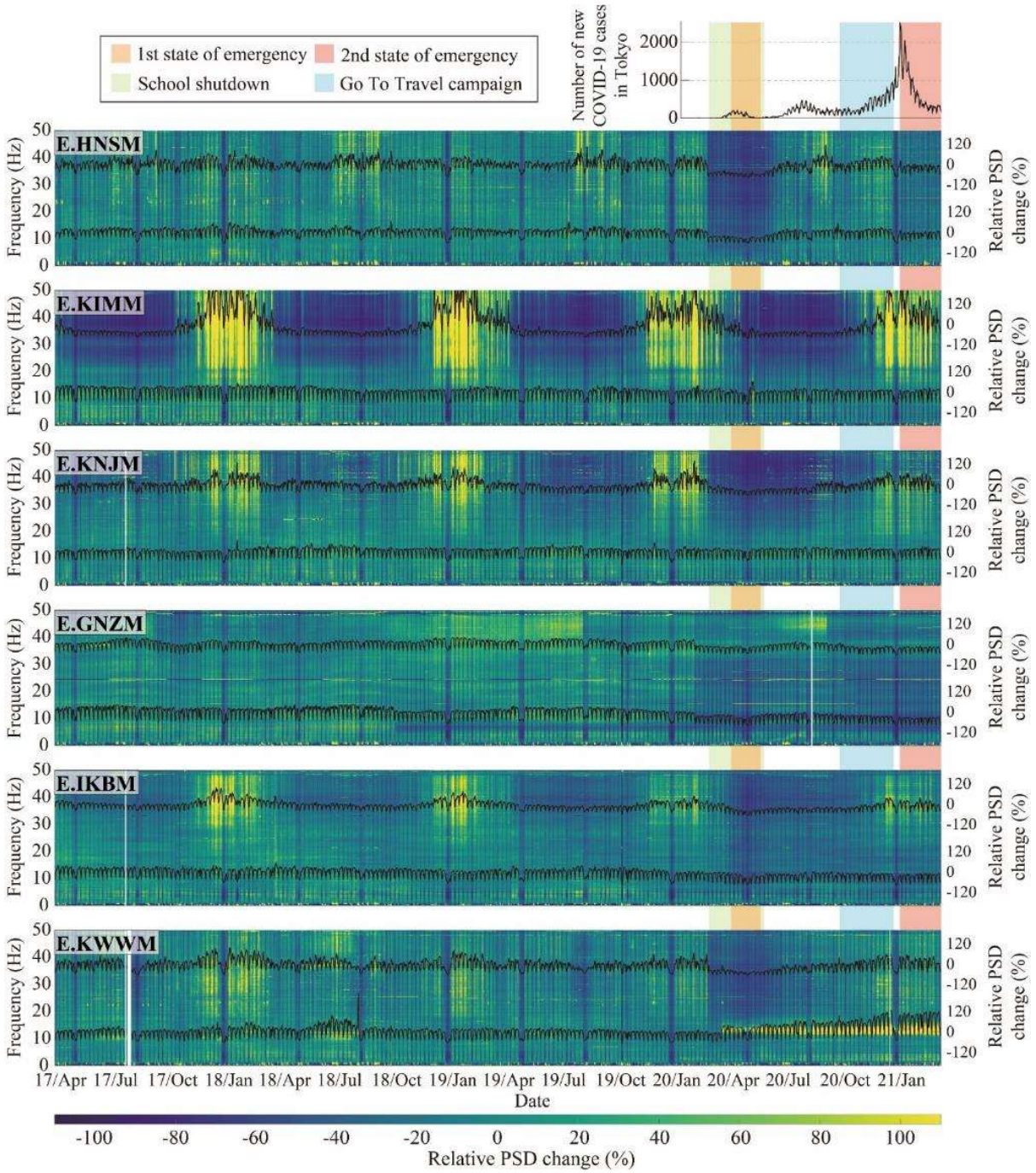

Figure 5.3. *Time-series of the relative noise level from April 2017 to March 2021 for six stations. The background color indicates the relative noise level at each frequency. The upper and lower black solid lines in each panel represent the relative noise level of the mean value in the frequency ranges of 4 to 14 Hz and 20 to 45 Hz, respectively. The upper right figure shows the number of new COVID-19 cases in Tokyo (same as Figure 5.1). The orange and pink shaded areas represent the periods of the first and second states of emergency in Tokyo, respectively; the green shaded area represents the period of school closures, and the light blue shaded area represents the period of the Go-To Travel campaign.*

5.3. Temporal changes in relative noise level

To monitor the PSD, I estimated the temporal changes in the relative noise level (R) at each station using the following equation:

$$R\ (\%) = \frac{PSD_{cur} - PSD_{ref}}{PSD_{ref}} \times 100, \quad (5.1)$$

where PSD_{cur} represents the daily PSD, which was estimated using the median value of all segments during specific time segments and PSD_{ref} represents the median value of 2 years of PSD_{cur} from April 2017 to March 2019. The PSDs were used without logarithmic transformation.

Figure 5.3 shows the temporal changes in the relative noise level (R) at several stations, calculated using the PSD_{cur} for all segments in a day. The largest decrease in PSD was observed during the first state of emergency at most stations (e.g., E.HNSM and E.KNJM). This variation was larger at higher frequencies, consistent with the results of a previous study (Yabe et al., 2020). To clarify the differences in variation with frequency, I focused on the two frequency bands of 4–14 Hz and 20–45 Hz. The high-frequency range of 20–45 Hz was previously found to show a two-step seismic noise reduction (Yabe et al., 2020), whereas the low-frequency range of 4–14 Hz was found to show a clear reduction during lockdowns worldwide (Lecocq et al., 2020). The mean PSD value was calculated for each frequency band, and the temporal change in the relative noise level was calculated using equation (5.1) (black solid lines in Fig. 5.3). The variations in the PSD were different in each frequency range. Some stations showed clear seasonal variations, especially in the higher frequency range (e.g., E.KIMM), whereas they were less pronounced at lower frequencies.

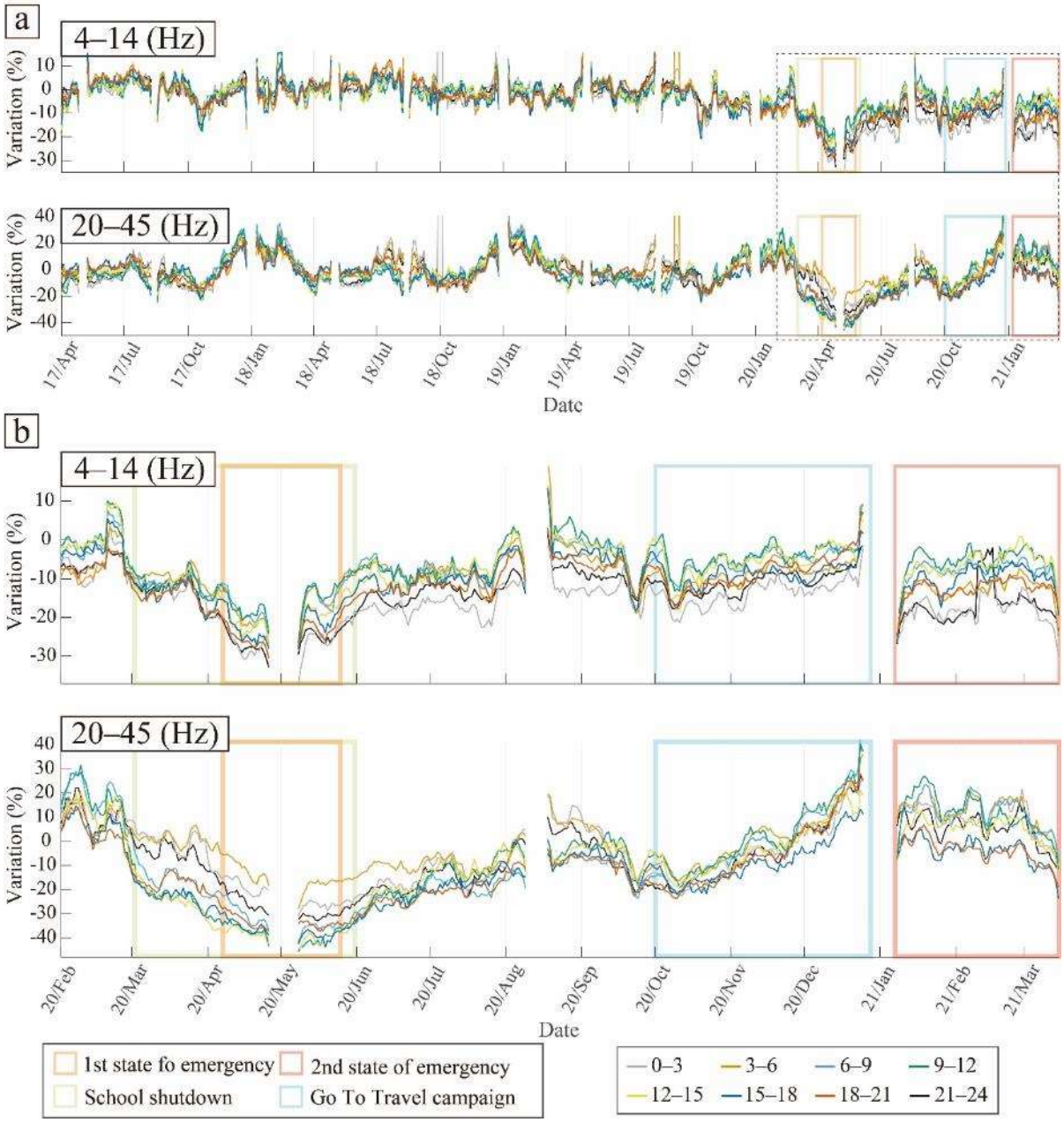

Figure 5.4. *Temporal variations of PSD depending on the time of day. (a) From April 2017 to March 2020. (b) Enlarged view of the black dashed square in panel (a). Each solid line indicates the PSD in each period shown in the right bottom box. The orange and pink squares represent the periods of the first and second states of emergency in Tokyo, respectively; the green square represents the period of school closures; the light blue square represents the period of the Go-To Travel campaign.*

5.4. Variation with time of day

The anthropogenic noise levels throughout the day are known to have distinct variations due to variations in human activities with the time of day (Green et al., 2017; Groos & Ritter, 2009; Lecocq et al., 2020; McNamara & Buland, 2004; Yabe et al., 2020). In this study, I estimated the temporal variations of the PSD for each time of day to determine which times of day are more sensitive to changes in human activities related to COVID-19. The temporal variations of PSD depending on the time of day were estimated by calculating PSD_{cur} for a specific period. The time range was set to 3 hrs. To eliminate the effect of the day of the week and calendar effects, I removed bank holidays and the periods around long holidays (New Year holidays: December 26–January 7, summer holidays: August 10–August 17, and consecutive holidays: April 27–May 7) and smoothed the data using a 7-day moving window. Although the temporal variations of PSD showed different trends depending on the station, the median values of the variations of all stations were used to determine the overall trend of the variation.

Figure 5.4 shows the temporal variation of PSD with a time of day, and, as can be seen, the overall trend of the PSD variations significantly differs between the two frequency bands. In the high-frequency range (20–45 Hz), the PSD rapidly decreased following the school closures, whereas this trend was not clear in the low-frequency range (4–14 Hz), as discussed in a previous study (Yabe et al., 2020). The long-period temporal variations of PSD showed strong seasonal variations in the high-frequency range (20–45 Hz), whereas they were not clearly visible in the low-frequency range (4–14 Hz) (Fig. 5.4a). After the outbreak of COVID-19, the difference in the temporal variations of PSD with a time of day became larger in both frequency bands (Fig. 5.4b).

In the low-frequency range (4–14 Hz), the PSD decreased in all periods during the first declared state of emergency and quickly recovered to near previous levels after the state of emergency was lifted (Fig. 5.4). The degree of PSD reduction depended on the time of the day. The largest reductions were observed from 21:00 to 3:00 in most periods. Interestingly, differences in the variations of PSD between daytime and nighttime were still observed after the first state of emergency was lifted.

In the high-frequency range (20–45 Hz), the daytime PSD was clearly reduced during the school closures before the state of emergency was declared (Fig. 5.4). That reflects a decrease in the noise level due to the absence of school-related activities. Because MeSO-net stations are mainly installed in schools, the PSDs observed at MeSO-net stations are more sensitive to noise related to school activities (Yabe et al., 2020). However, considering the large PSD reductions from 6:00 to 21:00, these reductions do not only reflect a decrease in school activities but also in other human activities (e.g., traffic). The PSD during the Go To Travel campaign gradually increased in all periods, and the differences in the time-dependent

PSD variations became smaller. During the second declared state of emergency, the PSD decreased significantly from 15:00 to 21:00. This was because the second state of emergency was targeted to restrict nonessential and non-urgent outings, especially at night.

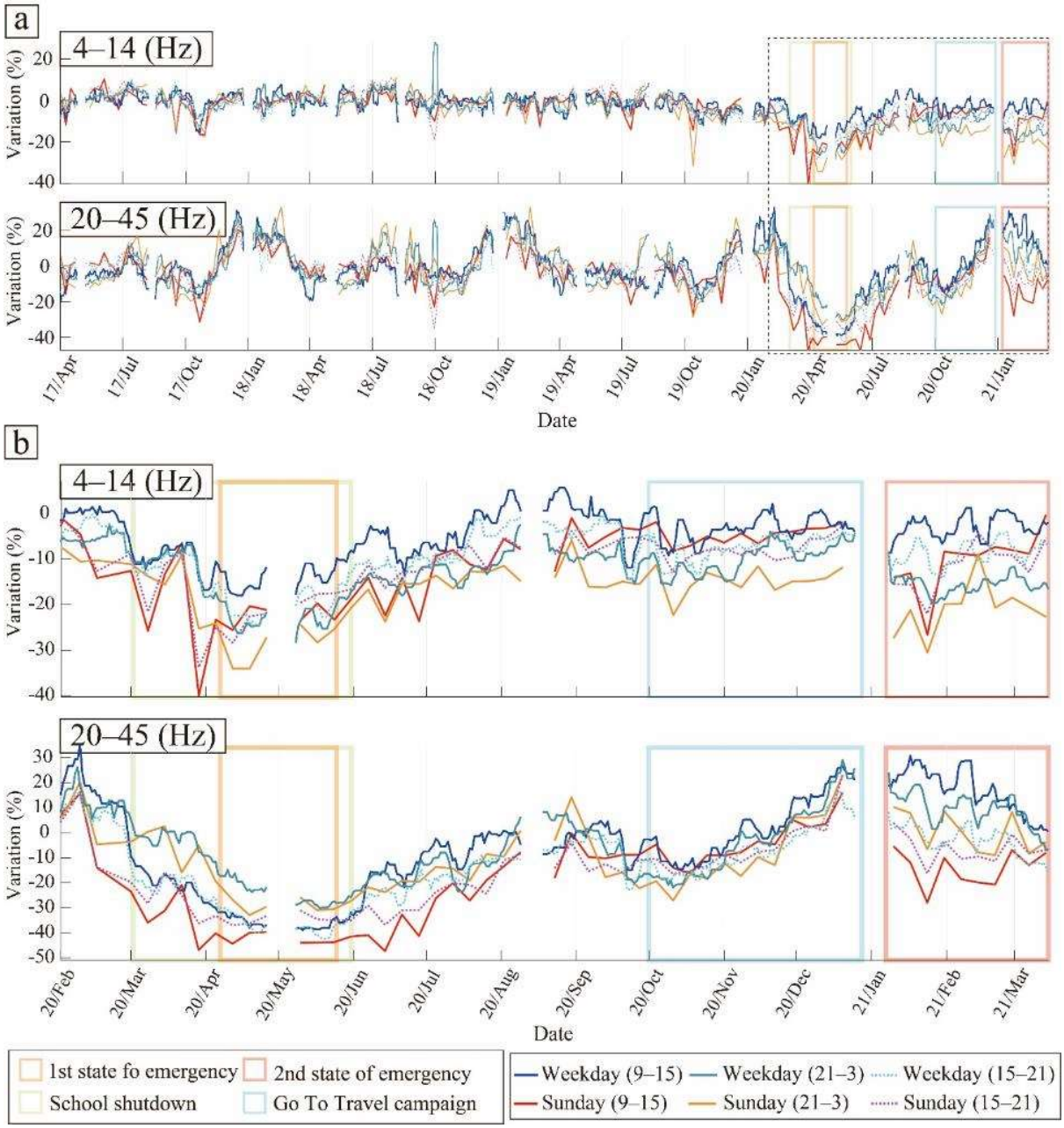

Figure 5.5. *Temporal variations of PSD depending on the day of the week. (a) From April 2017 to March 2020. (b) Enlarged view of the black dashed square in panel (a). Each solid line indicates the PSD under each condition shown in the right bottom box. The orange and pink squares represent the periods of first and second states of emergency in Tokyo, respectively; the green square represents the period of school closures; the light blue square represents the period of the Go-To Travel campaign.*

5.5. Variation with a day of the week

In the analysis of the variation of the PSD depending on the time of day, the effect of the day of the week was ignored by using a 7-day moving window (Fig. 5.4). Because the difference in the PSD between weekdays and Sundays was significant (Fig. 5.3), the differences in the temporal variations of PSD of the day of the week were also examined. In this study, the temporal variations of PSD were calculated separately for weekdays and Sundays. Bank holidays and the periods around long holidays were excluded. For weekdays, the data was smoothed using a 7-day moving window after weekday data extraction. Considering the differences in PSD based on the time of day (Fig. 5.4), I calculated the temporal variations of PSD during the daytime (9:00 to 15:00), the evening (15:00 to 21:00), and at night (21:00 to 3:00).

Figure 5.5 shows the results of the PSD considering both the day of the week and the time of day. The temporal variations of PSD with the day of the week showed strong seasonal variations in the high-frequency range (20–45 Hz), whereas they were not clear in the low-frequency range (4–14 Hz) (Fig. 5.5a). After the outbreak of COVID-19, the differences in the temporal variations of PSD by day of the week became more pronounced (Fig. 5.5b). The difference in the daytime PSD between weekdays and Sundays was significant after the outbreak of COVID-19 (blue and red solid lines in Fig. 5.5b).

In the low-frequency range (4–14 Hz), the nighttime PSD decreased the most after the outbreak of COVID-19 in most periods, regardless of the day of the week, similar to the results for each period (Fig. 5.4b and 5.5b).

In the high-frequency range (20–45 Hz), the PSDs decreased significantly during the period of school closures and the first declared state of emergency, whereas the variations differed for each day of the week in the following periods. The PSD recovered rapidly on weekdays after the state of emergency was lifted, while it recovered only gradually on Sundays. Although the PSD variations depending on the time of day also showed gradual recoveries after the first state of emergency (Fig. 5.4b), the trend was most influenced by the gradual recovery on Sundays. During the Go-To Travel campaign, the differences based on the day of the week became quite small in the high-frequency range. During the second state of emergency, the variations of PSD were different on different days of the week. The daytime PSD on Sundays showed a significant reduction, whereas that on weekdays did not change.

5.6. Seasonal effects

The PSDs varied significantly depending on the restrictions of human activities or economic measures during the COVID-19 pandemic but also showed clear seasonal variations (Figs. 5.3–5.5). In particular, in the frequency range of 20–45 Hz, the seasonal variations were as large as those related to COVID-19. To identify stations where the seasonal variations have a strong annual cycle, I calculated the correlation coefficient (CC) for annual temporal changes in relative noise levels between April 2017 to March 2018 and April 2018 to March 2019 using the following equation:

$$CC = \frac{cov(y_{2017}, y_{2018})}{\sigma_{y_{2017}} \sigma_{y_{2018}}}, \tag{5.2}$$

where y_{2017} and y_{2018} represent the smoothed annual changes in noise level with a 30-day moving average for April 2017 to March 2018 and April 2018 to March 2019, respectively; and $\sigma_{y_{2017}}$ and $\sigma_{y_{2018}}$ represent the variances of y_{2017} and y_{2018}, respectively.

Using maps of the correlation coefficients estimated at each station (Figs. 5.2b and c), I identified stations with strong and consistent seasonal effects. In the frequency range of 4–14 Hz, the number of stations with high correlation coefficients was limited. However, in the frequency range of 20–45 Hz, many stations yielded high correlation coefficients, while some areas had low correlation coefficients. For instance, around Tokyo station (yellow star in Fig. 5.2a), I observed a low correlation for weekdays in the daytime for the frequency range of 20–45 Hz. Low correlations can be attributed to weak seasonal effects and non-periodic changes in noise levels related to irregular local events and changes in the environment.

The annual seasonal change was defined as the mean value of changes from April 2017 to March 2018 and from April 2018 to March 2019. The annual seasonal changes showed significant variations depending on the station (gray dots in Fig. 5.6). To visualize the overall trend of the variations, the median value of the annual seasonal changes (solid lines in Fig. 5.6) at the stations, which showed correlation coefficients >0.2 (circles in Figs. 5.2b and c), was used. To stabilize the seasonal variation, I ignored stations that showed correlation coefficients <0.2. The median values showed a clear seasonal variation on each day of the week and at each time point.

In the low-frequency range (4–14 Hz), the nighttime seasonal changes showed a strong PSD from July to August and a weak PSD from October to November (Fig. 5.6a). The daytime seasonal changes did not show a clear trend, and the error bars were much larger than the seasonal changes (boxes and dashed lines in Fig. 5.6a).

In the high-frequency range (20–45 Hz), the daytime seasonal changes for the weekdays showed a clear trend (Fig. 5.6b) with a large peak (from late November to early March) and two small dips (around late March and August). The two small dips coincided with long school holidays (roughly from March 25 to April 5 and from July 20 to August 31 at elementary schools in Tokyo). Therefore, I concluded that this noise reduction was mainly related to school activities. The nighttime seasonal changes showed a strong seasonal variation on both weekdays and Sundays (right panels in Fig. 5.6b), increasing during the summer and winter. An increase in PSD in summer was observed at night in both frequency bands.

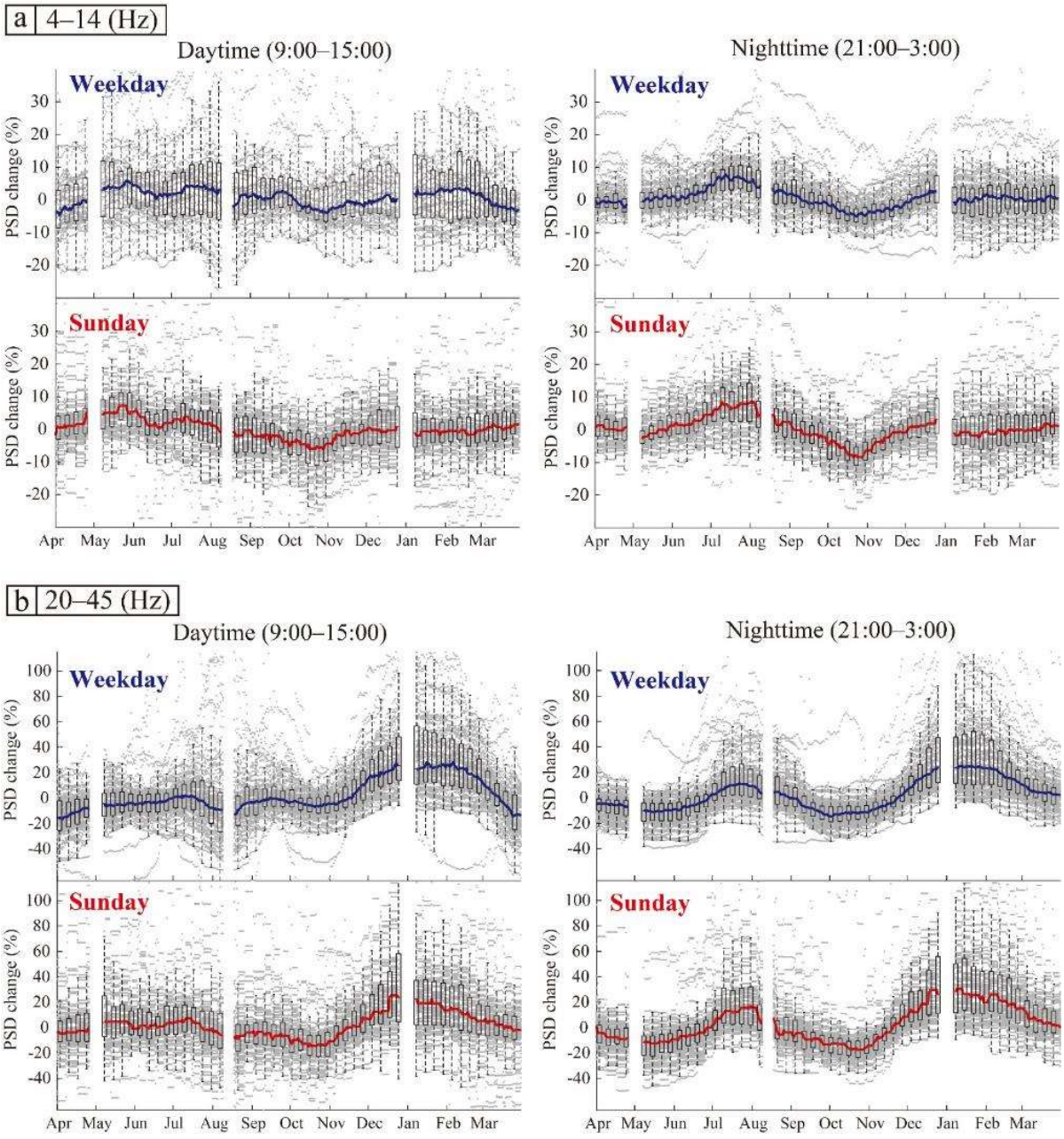

Figure 5.6. *Seasonal variations in the relative noise level in the frequency range (a) 4–14 Hz and (b) 20–45 Hz. The left and right panels show the daytime and nighttime results, respectively. Gray dots represent the seasonal variations at each station, showing correlation coefficients >0.2 (circles in Figs. 5.2b and c). The blue and solid red lines indicate the median values on weekdays and Sunday, respectively. The boxes represent the first and third quartiles, and the error bars represent the minimum and maximum values within the 1.5× the interquartile range from the first and third quartiles. The boxes and error bars were plotted every 7 days.*

5.7. Temporal changes in relative noise level during the COVID-19 pandemic

The temporal changes in the relative noise level were corrected for seasonal changes by deducting the annual seasonal changes. The corrected temporal changes in the relative noise level from January 2020 to March 2021 at each station and their median values are shown by gray dots and solid lines in Figure 5.7, respectively. The median values clearly decreased around the periods of school closures and declared states of emergency in most cases (Fig. 5.7).

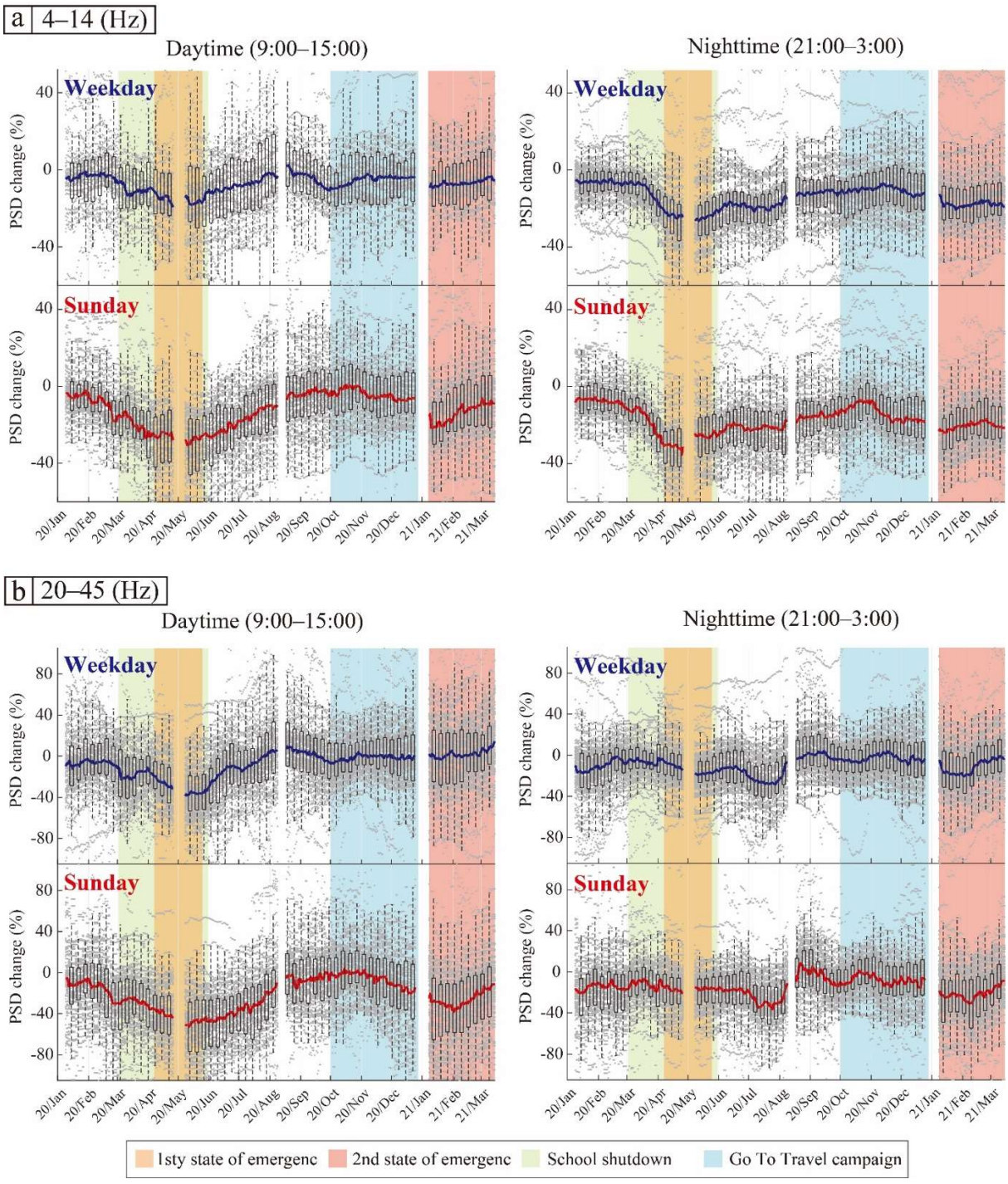

Figure 5.7. *Corrected temporal changes in the relative noise level in the frequency range (a) 4–14 Hz and (b) 20–45 Hz. The left and right panels show the daytime and nighttime results, respectively. The gray dots represent the corrected temporal changes at each station, showing correlation coefficients >0.2 (circles in Figs. 5.2b and c). The blue and solid red lines indicate the median values on weekdays and Sunday, respectively. The boxes represent the first and third quartiles, and the error bars represent the minimum and maximum values within the 1.5× the interquartile range from the first and third quartiles. The boxes and error bars were plotted every 7 days. The orange and pink shaded areas represent the periods of the first and second*

states of emergency in Tokyo, respectively; the green shaded area represents the period of school closures; the light blue shaded area represents the period of the Go-To Travel campaign.

In the low-frequency range (4–14 Hz), the PSDs decreased in all cases during the first state of emergency; after that, the PSDs gradually recovered, almost reaching pre-COVID-19 pandemic noise levels, until the beginning of the Go-To Travel campaign (Fig. 5.7a). During the Go-To Travel campaign, no further increase was apparent. On Sunday nights, the PSD decreased rapidly since November. In the daytime on Sundays, the PSD decreased significantly with the second declared state of emergency.

In the high-frequency range (20–45 Hz), the daytime PSD decreased significantly around the periods of school closures and declared states of emergency (Fig. 5.7b). The daytime PSD on weekdays recovered rapidly after the first state of emergency was lifted, while that on Sundays did not immediately recover, similar to the results for the day of the week (Fig. 5.5b).

During the Go-To Travel campaign, the PSD did not change clearly in all cases, although the results for the days of the week showed a significant increase in PSD during this period (Figs. 5.5b and 5.7b). Thus, correcting for the annual seasonal variations revealed that most stations recorded PSD variations similar to that pre-COVID-19 pandemic. After the declaration of the second state of emergency, the PSDs clearly decreased, except for the daytime on weekdays. These trends are similar to the results shown in Figure 5.5b. Around the end of the second state of emergency, the PSDs increased, although the results for the days of the week showed a decrease (Figs. 5.5b and 5.7b). At night, the PSDs clearly decreased from July to August (right panels in Fig. 5.7b). This period corresponds to a large seasonal variation of PSD in summer (Fig. 5.6b).

5.8. Discussion

Using continuous seismic data from MeSO-net stations, I monitored the changes in the seismic noise levels around Tokyo from April 2017 to March 2021. To constrain the effect of human activities on anthropogenic seismic noise, I studied the temporal variations of PSD depending on the time of day and day of the week (Figs. 5.4 and 5.5). The PSDs showed significant variations in restrictions and measures during the COVID-19 pandemic. Furthermore, the PSDs showed clear seasonal or periodic variations, especially in the frequency range of 20–45 Hz (Figs. 5.4a and 5.5a). To confirm this seasonal effect, I estimated seasonal changes and corrected for these changes in the noise level using stations where the correlation of the PSDs of the periods April 2017 to March 2018 and April 2018 to March 2019

yielded correlation coefficients >0.2. Although the number of stations with correlation coefficients >0.2 was limited, especially in the frequency range of 4–14 Hz (Figs. 5.2b and c), the median value of the seasonal variations showed significant features in both frequency ranges (Fig. 5.6). Most seasonal changes showed a strong PSD and a weak PSD season. Since the seasonal changes were as large as the changes related to COVID-19, I corrected for the temporal changes in the relative noise level by deducting the annual seasonal changes. Most of the corrected temporal variations of the PSDs showed the largest reduction during the first state of emergency for both time of day and day of the week (Figs. 5.4, 5.5, and 5.7). To compare the features of the corrected temporal variations of the PSDs, I plotted their median values on the same graph (Fig. 5.8).

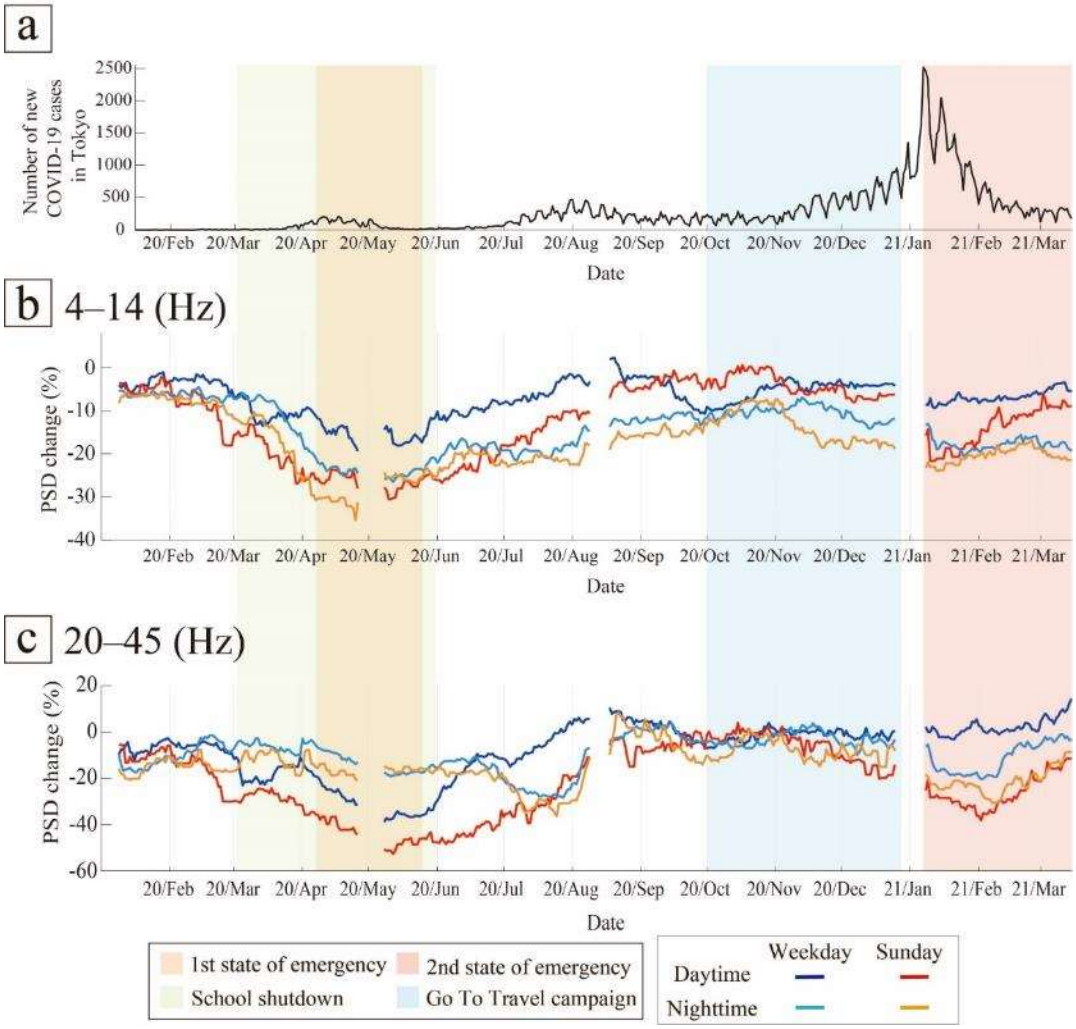

Figure 5.8. *(a) The number of new COVID-19 cases in Tokyo (same as Fig. 5.1). (b–c) Comparison between temporal changes in the noise level in the frequency ranges (b) 4–14 Hz and (c) 20–45 Hz. The orange and pink shaded areas represent the periods of the first and second states of emergency in Tokyo, respectively; the green shaded area represents the period*

of school closures; the light blue shaded area represents the period of the Go-To Travel campaign.

During the first state of emergency, the PSD decreased the most under all conditions except at night in the high-frequency range (orange shaded area in Fig. 5.8). That was because the first state of emergency had tighter restrictions than the second state of emergency. For instance, school closures and forgoing unnecessary outings were requested in the first state of emergency, whereas school activities and leisure events continued during the second state of emergency. In the latter period, the nighttime PSD in the high-frequency range did not show a reduction (light blue and orange lines in Fig. 5.8c). Moreover, the results for the time of day in this range also showed only a small reduction in the first state of emergency (gray and right orange lines in Fig. 5.3b). The first state of emergency was less sensitive to the noise level at night (21:00–3:00).

In addition, the daytime PSD on weekdays in the high-frequency range further decreased after the beginning of the school closures, but the decrease was smaller (blue line in Fig. 5.8c). During the first state of emergency, in addition to the school closures, the majority of educational and recreational facilities were ordered to close; therefore, noise decreased more significantly during this period than during the school closure period. The daytime results for weekdays during the first state of emergency were similar to the two-step PSD reduction reported by Yabe et al. (2020), and these trends were also confirmed in the wider Tokyo area that was covered by the stations used in this study.

After the first state of emergency was lifted, the daytime PSD immediately recovered on weekdays (blue lines in Figs. 5.8b and c). In contrast, the recovery on Sundays was gradual (red lines in Figs. 5.8b and c). The PSDs continued to recover until the period of the Go To Travel campaign. The weekday noise level strongly reflected the effects of the lifting of the state of emergency, whereas the Sunday noise level likely reflected the concern of people about COVID-19, as most people continued to avoid non-essential outings even after the state of emergency was lifted.

The nighttime PSD in the high-frequency range showed a significant reduction from late June to late August (light blue and orange lines in Fig. 5.8c). In this period, the seasonal variation of PSD at night increased (right panels in Fig. 5.6b). Therefore, this reduction could indicate a lack of summer night activities, as in previous years.

During the Go-To Travel campaign (light blue shaded area in Fig. 5.8), the PSDs showed no clear variation except for at night on Sundays in the low-frequency range, even though the results for time of day and day of the week in the high-frequency range showed significant increases during this period (Figs. 5.4b and 5.5b). Thus, the increases in PSD in the

high-frequency range during this period were not due to the Go-To Travel campaign but rather to seasonal changes. The rate of variation of PSD recovered was almost zero, and the difference between each condition became small during this period, especially in the high-frequency range (Fig. 5.8c). I assume that the level of social activities was close to the normal conditions before the COVID-19 pandemic. Before the COVID-19 pandemic, the differences in each condition were smaller than those after the outbreak of COVID-19 (Figs. 5.4a and 5.5a).

Following the declaration of the second state of emergency, all PSDs except for the daytime PSD on weekdays showed a significant reduction in both frequency ranges (pink shaded area in Fig. 5.8). The second state of emergency was focused on restricting activity at night. Accordingly, the nighttime PSD followed the effect of the second state of emergency. Furthermore, if the Sunday noise levels indeed strongly reflect the concern of the people about COVID-19, most people avoided non-essential outings voluntarily. The PSDs gradually increased from the middle of the second state of emergency, suggesting a gradual reduction in public concern about COVID-19 following a decrease in the number of infections.

5.9. Conclusions

In this study, I analyzed the differences in the temporal variations of PSD in two different frequency ranges for the time of day and day of the week during the COVID-19 pandemic. Our results will help identify specific sources of anthropogenic seismic noise. Furthermore, recently, because of the development of permanent high-quality seismic networks and seismic processing techniques, it has become possible to use specific anthropogenic noises to visualize near-surface structures. Anthropogenic seismic noises, such as traffic and trains, were used to extract shear, compressional, or surface waves propagating between pairs of stations by computing cross-correlations for visualization or monitoring (Brenguier et al., 2019; Nakata et al., 2011). Identifying dominant anthropogenic noise is thus useful in geophysical exploration using passive seismic noise. Studying anthropogenic seismic noise is an efficient way to characterize and monitor specific human activities and visualize underground structures.

References

Brenguier, F., Boué, P., Ben-Zion, Y., Vernon, F., Johnson, C. W., Mordret, A., Courant, O., Share, P. -E., Beaucé, E., Hollis, D. & Lecocq, T. Train Traffic as a Powerful Noise Source for Monitoring Active Faults With Seismic Interferometry. *Geophys. Res. Lett.* **46**, 9529-9536; doi:10.1029/2019GL083438 (2019).

Díaz, J., Ruiz, M., Sánchez-Pastor, P. S. & Romero, P. Urban Seismology: On the origin of earth vibrations within a city. *Sci. Rep.* **7**, 1-11 (2017).

Green, D. N. & Bowers, D. Seismic raves: Tremor observations from an electronic dance music festival. *Seismol. Res. Lett.* **79**, 546-553l; doi:10.1785/gssrl.79.4.546 (2008).

Green, D. N., Bastow, I. D., Dashwood, B. & Nippress, S. E. J. Characterizing broadband seismic noise in Central London. *Seismol. Res. Lett.* **88**, 113-124; doi:10.1785/0220160128 (2017).

Groos, J. C. & Ritter, J. R. R. Time domain classification and quantification of seismic noise in an urban environment. *Geophys. J. Int.* 179, 1213-1231; doi:10.1111/j.1365-246X.2009.04343.x (2009).

Gössling, S., Scott, D. & Hall, C. M. Pandemics, tourism and global change: a rapid assessment of COVID-19. *J. Sustain. Tour.* **29**, 1-20; doi:10.1080/09669582.2020.1758708 (2020).

Hong, T.-K., Lee, J., Lee, G., Lee, J. & Park, S. Correlation between ambient seismic noises and economic growth. *Seismol. Res. Lett.* **91**, 2343-2354; doi:10.1785/0220190369 (2020).

Kasahara, K., Sakai, S., Morita, Y., Hirata, N., Tsuruoka, H., Nakagawa, S., Nanjo, K. & Obara, K. Development of the Metropolitan Seismic Observation Network (MeSO-net) for detection of mega-thrust beneath Tokyo metropolitan area. *Bull. Earthq. Res. Institute, Univ. Tokyo* **84**, 71-88 (2009).

Kuzma, H. A., Fernández-Martínez, J. L., Zhao, Y., Dunson, C. & Zhai, M. Vehicle traffic as a source for near-surface passive seismic imaging. in *Symposium on the Application of Geophysics to Engineering and Environmental Problems 2009,* 609-615 (2009).

Larose, E., Carrière, S., Voisin, C., Bottelin, P., Baillet, L., Guéguen, P., Walter, F., Jongmans, D., Guillier, B., Garambois, S., Gimbert, F. & Massey, C. Environmental seismology: What can we learn on earth surface processes with ambient noise? *J. Appl Geophy.* **116**, 62-74; doi:10.1016/j.jappgeo.2015.02.001 (2015).

Lecocq, T., Hicks, S. P., Van Noten, K., van Wijk, K., Koelemeijer, P., De Plaen, R. S. M., Massin, F., Hillers, G., Anthony, R. E., Apoloner, M.-T., Arroyo-Solórzano, M., Assink, J. D., Büyükakpınar, P., Cannata, A., Cannavo, F., Carrasco, S., Caudron, C., Chaves, E. J., Cornwell, D. G., Craig, D., den Ouden, O. F. C., Diaz, J., Donner, S., Evangelidis, C. P., Evers, L., Fauville, B., Fernandez, G. A., Giannopoulos, D., Gibbons, S. J., Girona, T., Grecu, B., Grunberg, M., Hetényi, G., Horleston, A., Inza, A., Irving, J. C. E., Jamalreyhani, M., Kafka, A., Koymans, M. R., Labedz, C.

R., Larose, E., Lindsey, N. J., McKinnon, M., Megies, T., Miller, M. S., Minarik, W., Moresi, L., Márquez-Ramírez, V. H., Möllhoff, M., Nesbitt, I. M., Niyogi, S., Ojeda, J., Oth, A., Proud, S., Pulli, J., Retailleau, L., Rintamäki, A. E., Satriano, C., Savage, M. K., Shani-Kadmiel, S., Sleeman, R., Sokos, E., Stammler, K., Stott, A. E., Subedi, S., Sørensen, M. B., Taira, T., Tapia, M., Turhan, F., van der Pluijm, B., Vanstone, M., Vergne, J., Vuorinen, T. A. T., Warren, T., Wassermann, J. & Xiao, H. Global quieting of high-frequency seismic noise due to COVID-19 pandemic lockdown measures. *Science.* (2020). doi:10.1126/science.abd2438.

Lindsey, N. J., Yuan, S., Lellouch, A., Gualtieri, L., Lecocq, T. & Biondi, B. City-scale dark fiber DAS measurements of infrastructure use during the COVID-19 pandemic. *Geophys. Res. Lett.* 47, e2020GL089931; doi:10.1029/2020gl089931 (2020).

Longuet-Higgins, M. S. A theory of the origin of microseisms. *Philos. Trans. R. Soc. London* **243**, 1-35 (1950).

McNamara, D. E. & Boaz, R. I. Visualization of the seismic ambient noise spectrum in *Seismic Ambient Noise* (eds. Nakata, N, Gualtieri, L & Fichtner, A) 1-29 (Cambridge University Press, 2019).

McNamara, D. E. & Buland, R. P. Ambiente noise levels in the continental United States. *Bull. Seismol. Soc. Am.* **94**, 1517; doi:10.1785/012003001 (2004).

Nakata, N., Snieder, R., Tsuji, T., Larner, K. & Matsuoka, T. Shear wave imaging from traffic noise using seismic interferometry by cross-coherence. *Geophysics* 76, SA97; doi:10.1190/geo2010-0188.1 (2011).

Poli, P., Boaga, J., Molinari, I., Cascone, V. & Boschi, L. The 2020 coronavirus lockdown and seismic monitoring of anthropic activities in Northern Italy. *Sci. Rep.* 10, 9404; doi:10.1038/s41598-020-66368-0 (2020).

Riahi, N. & Gerstoft, P. The seismic traffic footprint: Tracking trains, aircraft, and cars seismically. *Geophys. Res. Lett.* **42**, 2674-2681; doi:10.1002/2015GL063558 (2015).

Sakai, S. & Hirata, N. Distribution of the metropolitan seismic observation network. *Bull. Earthq. Res. Institute, Univ. Tokyo* **84**, 57-69 (2009).

Sohrabi, C., Alsafi, Z., O'Neill, N., Khan, M., Kerwan, A., Al-Jabir, A., Iosifidis, C. & Agha, R. World Health Organization declares global emergency: A review of the 2019 novel coronavirus (COVID-19). *International Journal of Surgery* **76**, 71-76; doi:10.1016/j.ijsu.2020.02.034 (2020).

Xiao, H., Eilon, Z. C., Ji, C. & Tanimoto, T. COVID-19 societal response captured by seismic noise in China and Italy. *Seismol. Res. Lett.* **91**, 2757-2768; doi:10.1785/0220200147 (2020).

Yabe, S., Imanishi, K. & Nishida, K. Two-step seismic noise reduction caused by COVID-19 induced reduction in social activity in metropolitan Tokyo, Japan. *Earth, Planets Sp.* **72**, 167 (2020).

Chapter 6

Conclusion

6.1. Research summary

I developed technique for both imaging and monitoring underground structure by using ambient seismic noise to solve various social issues such as disaster mitigation and resource development. This work is summarized as follows:

(1) In Chapter 2, I applied surface wave tomography using ambient noise to construct a high-resolution 3D S-wave velocity model in central Japan. I applied the zero-crossing method to estimate surface-wave dispersion curves in the frequency domain, and I obtained high 3D resolution of shallow structures by using a direct inversion method. The resultant velocity model clearly indicates small-scale geological features such as faults, sedimentary basins, volcanic systems, and geological boundaries. I identified magma-related structures without active-source data in the volcanic regions, and I identified a magma chamber below Mt. Nikko-Shirane based on its low seismic velocity anomaly. Our results also revealed the spatial distribution of fault traces as low-velocity anomalies. In the Izu collision area, I observed several high-velocity blocks separated by low-velocity boundaries, which may represent microplates. Our high-resolution velocity model can be used to simulate seismic wave propagation to understand the characteristics of amplification in central Japan and thereby contribute to disaster management and assessment.

(2) In Chapter 3, I proposed a three-dimensional S-wave velocity model in the Kanto basin estimated by joint inversion using multimodal Rayleigh and Love waves. The multimodal dispersion curves of Rayleigh and Love waves were estimated using the F-J method. Including higher modes improved the accuracy and precision of the inverted solutions by at least 50% in the simulation test. The error of inversion using actual observed data decreased by more than 98% when I added the first and second overtone to the fundamental mode. The high-precision multimodal joint inversion constructed smooth three-dimensional S-wave velocity model, despite the inversions being independent. Our estimated model revealed a low-velocity anomaly of sediments towards the east and a curved velocity contour of the basement rock. Such structures better explain the observed surface-wave dispersion curves than the previous model. My estimated model could successfully estimate the three-dimensional S-wave velocity,

including that of the basement rock, using only surface-wave dispersion data from ambient noise, which has significant implications. The high-resolution three-dimensional S-wave velocity model is essential to understand the complex amplification of surface waves that cause strong motion, especially in a basin. Our velocity model can improve the earthquake simulation and hazard assessment.

(3) In Chapter 4, I developed an approach to monitor underground by cross-correlation of ambient seismic noise. Taking advantage of always present of ambient seismic noise, the time-series cross-correlations ware calculated, and the relative velocity change of surface wave was estimated. My mapping results showed the continuous temporal variation in seismic velocity across the fault and volcano during the Kumamoto earthquake. The higher spatial resolution of our estimated seismic velocity variation in a broad area allowed us to identify the spatial distribution of the damage zone or stress state. Seismic velocity near the rupture faults and Aso volcano decreased during the earthquake. The velocity reduction near the faults may have been due to formation damage, a change in stress state, and an increase in pore pressure. Furthermore, I mapped the post-earthquake fault-healing process. The largest seismic velocity reduction observed at Aso volcano during the earthquake was likely caused by pressurized volcanic fluids. The large increase in seismic velocity at the volcano's magma body was observed ~3 months after the earthquake, which may have responded to depressurization caused by the eruption. This study demonstrates the usefulness of continuous monitoring of faults and volcanoes.

(4) In Chapter 5, I focused on anthropogenic seismic noise which is dominant in higher frequency ambient noise. Understanding the characteristics of anthropogenic help identify specific sources of anthropogenic seismic noise, which may be utilized as the signal of geophysical explorations. Since anthropogenic seismic noise is strongly associated with social activities, the magnitude of the anthropogenic seismic noise varies with the time of day and day of the week. I analyzed the differences in the temporal variations of PSD in the Tokyo metropolitan area in two different frequency ranges for a time of day and day of the week during the COVID-19 pandemic. The results showed the largest reduction in noise levels during the first state of emergency under most conditions. After the first state of emergency was lifted, the daytime noise reverted to previous levels immediately on weekdays and gradually on Sundays. That was likely because economic activities instantly resumed, while non-essential outings were still mostly avoided on Sundays. Furthermore, the daytime noise level on Sundays was strongly reduced regardless of changes on weekdays after the second state of emergency, which restricted activities mainly at night. Sunday noise levels gradually increased from the middle of the second state of emergency, suggesting a gradual reduction in public

concern about COVID-19 following a decrease in the number of infections. Our findings demonstrate that seismic noise can be used to monitor social activities.

6.2. Future work

As described in section 6.1, I developed the applications to image and monitor underground structures using ambient seismic noise. This section mentioned how we utilize the developed applications and has room for improvement.

(1) In Chapter 2, I constructed the spatially high-resolution S-wave velocity model by applying surface-wave tomography. I improved the resolution by including dispersion curves in higher frequencies, which can reflect smaller structures. Since the high-frequency surface waves are easily attenuated, extraction of higher-frequency information in the far station pair was difficult. To overcome this problem, increasing the signal-to-noise ratio is necessary. Some studies were reported to increase the signal-to-noise ratio by additional preprocessing such as stacking. As described in Chapter 3, the inclusion of higher-order modes of dispersion curves can also improve the accuracy and precision of inversion. Combined with these methods, a more detailed S-wave velocity can be constructed.

(2) In Chapter 3, a multimodal surface wave joint inversion was developed. The inclusion of higher-order modes improved the accuracy and precision of the solution of inversion by more than 50% compared to previous methods. According to Chapter 3, the inversion using the fundamental mode to the second overtone of dispersion curves almost completely reconstructs the true model, even if the inversion includes either Rayleigh or Love wave. If we obtain Rayleigh and Love wave dispersion curves from fundamental mode to second overtones, the P-wave velocity structure could be inverted from dispersion curves of Rayleigh wave after the S-wave velocity structure was estimated from dispersion curves of Love wave. The Rayleigh wave incorporates the sensitivity of S-waves and P-wave velocity, but the Love wave has no sensitivity of P-wave velocity. The S- and P-wave velocity structures are essential for revealing resource distributions such as gas and magma reservoirs.

(3) In Chapter 4, I monitored seismic velocity change due to the Kumamoto earthquake. My result clearly reflected the damage zone the seismogenic fault zone as the area where velocity largely decreased. This approach can be applied anywhere permanent seismometers are deployed, such as Hi-net in the Japanese and arrays in the United States. Velocity changes due to slow slip or foreshocks identified through this crustal-scale monitoring could thus be used to estimate future earthquakes. The denser deployment of

seismometers around fault zones and volcanoes would allow local anomalies related to earthquake and volcanic activities to be accurately resolved. Furthermore, the three-dimensional velocity change model could also be estimated by inversion using the depth sensitivity kernel of surface wave phase velocity. Understanding three-dimensional changes in the underground structure is important not only for revealing the earthquake mechanisms but also for resource development.

(4) In Chapter 5, I studied anthropogenic seismic noise. Our results will help identify specific sources of anthropogenic seismic noise. Furthermore, recently, because of the development of permanent high-quality seismic networks and seismic processing techniques, it has become possible to use specific anthropogenic noises to visualize near-surface structures. Anthropogenic seismic noises, such as traffic and trains, were used to extract shear, compressional, or surface waves propagating between pairs of stations by computing cross-correlations for visualization or monitoring. Identifying dominant anthropogenic noise is thus useful in geophysical exploration using passive seismic noise.

Acknowledgments

I spent my bachelor's, master's, and doctoral courses at Kyushu University. During this time, I could get many experiences and learn many things. These experiences made my not only researcher skills but also the spirit and humanity of people grow. As the culmination of what I have learned at Kyushu University, I could organize my studies in my doctoral dissertation. I want to thank all the people who have influenced me during this long university life.

I cannot thank Prof. Takeshi Tsuji and Assis. Prof. Ikeda enough. The great opportunity to meet two such wonderful researchers has changed my life. When I was an undergraduate student, I procrastinated on my research and caused many inconveniences. I still feel sorry about it. However, because of your advice and support at that time, I could become a more honest person. After that, you taught me many things, including being a researcher and spirit and humanity. Without your many supports, I would not have been able to become a researcher. After becoming a working person, I have met many researchers and realized the greatness of the two of you. There are still many things I am not skilled at, both as a researcher and as a member of society, but I would like to continue to devote myself to becoming as great a researcher as both of you someday.

I want to thank Junichi Ito, director of the Research Institute of Earthquake and Volcano Geology of Geological Survey of Japan, Osamu Fujiwara, deputy director, Masayuki

Yoshimi, and all the members of the Earthquake Hazard Assessment Research Group. Thank you very much for your support for me in entering the doctoral program for working people.

I would also like to thank my parents. Thank you for your concern about my health and my career path. I am proud to be a researcher which is the same job as my father, even though my father was against it.

Finally, I want to thank my family member Yuka. Because she is a hardworking researcher, even I, a lazy person, tend to study with her. Thanks to her, I was able to concentrate on writing my doctoral dissertation.

For both Chapter 2 and Chapter 4, I am deeply grateful to the National Research Institute for Earth Science and Disaster Resilience (NIED) for developing and providing the seismic data recorded by Hi-net. And for both Chapter 3 and Chapter 5, I am deeply grateful to NIED and the Earthquake Research Institute, University of Tokyo, for developing and providing the seismic data recorded by MeSO-net.

May 2022

Hiro Nimiya